Check for updates

The magnetocaloric effect properties for potential applications of magnetic refrigerator technology: a review

Phahul Zhemas Zul Nehan, [a] Okvarahireka Vitayaya,[a] Dicky Rezky Munazat,[a] Maykel T. E. Manawan,[bc] Darminto Darminto[d] and Budhy Kurniawan *[a]

In the pursuit of a clean and environmentally friendly future, magnetic refrigerator technology based on the magnetocaloric effect has been proposed as a replacement for conventional refrigeration technologies characterized by inefficient energy use, greenhouse gas emissions, and ozone depletion. This paper presents an in-depth exploration of the current state of research on magnetocaloric effect (MCE) materials by, examining various types of MCE materials and their respective potentials. The focus is particularly directed towards perovskite manganite materials because of their numerous advantages over other materials. These advantages include a wide working temperature range, easily adjustable Curie temperature around room temperature, excellent chemical stability, cost-effective production processes, negligible magnetic and thermal hysteresis properties, as well as competitive values for $-\Delta S_M$ and ΔT_{ad} compared to other materials. Additionally, crucial parameters defining the MCE properties of perovskite manganite materials are comprehensively discussed, both at a fundamental level and in detail.

[a] Department of Physics, Faculty of Mathematics and Natural Science, Universitas Indonesia, Depok 16424, Indonesia. E-mail: budhy.kurniawan@sci.ui.ac.id

[b] Program Study of Propulsion Technology, Faculty of Defense Science and Technology, Universitas Pertahanan, Bogor 16810, Indonesia

[c] Advanced Materials Research Center, National Research and Innovation Agency, Serpong 15314, Indonesia

[d] Department of Physics, Faculty of Science and Data Analytics, Institut Teknologi Sepuluh Nopember, Surabaya 60111, Indonesia

1. Introduction

Modern technology and massive improvements in industrial technology have exposed several problems for society, such as issues related to global warming and excessive energy consumption. These issues are believed to arise in modern

Phahul Zhemas Zul Nehan obtained Bachelor's degree in Physics, from Institut Teknologi Sepuluh Nopember (2023). Currently, He continues to study Master's degree in the Study Program of Materials Science at the Department of Physics from Universitas Indonesia under the supervision of Dr Budhy Kurniawan, Dr Maykel T. E. Manawan, and Prof. Dr Darminto. In his study, he received a Pendidikan Magister menuju Doktor untuk Sarjana Unggul (PMDSU) scholarship program from the Indonesian Ministry of Education, Culture, Research and Technology. His research interests are the materials science mainly in the characterization of magnetic, composite, and energy storage materials.

Phahul Zhemas Zul Nehan

Okvarahireka Vitayaya is currently a joint materials science MS student at Universitas Indonesia under the supervision of Dr Budhy Kurniawan R. and Dr Maykel T. E. Manawan in 2023. She obtained a Bachelor's degree in Physics from Universitas Riau in 2022. In her study, he received a Pendidikan Magister menuju Doktor untuk Sarjana Unggul (PMDSU) scholarship program from the Indonesian Ministry of Education, Culture, Research and Technology. Her research interest is in magnetic material properties such as colossal magnetoresistance and magnetocaloric effect of magnetic material, mainly Lanthanum manganite-based materials.

Okvarahireka Vitayaya

technology, particularly conventional gas compression-based refrigeration technology (CRT), which is increasingly prevalent in wider communities and areas.[1] This is supported by the world energy consumption data for CRT, which reportedly reached 17% in 2015,[2] and increased to 20% in 2018.[3] This condition demonstrates the extensive use of CRTs worldwide. Furthermore, conventional refrigerators have disadvantages, including high and inefficient energy consumption, low cooling efficiency cycles ranging from 5–10%, requiring ample space, and the presence of harmful gases still in use.[1,4,5] Hazardous gases utilized such as chlorofluorocarbons (CFC), hydrochlorofluorocarbons (HCFC), and hydrofluorocarbons (HFC) contribute to ozone layer depletion and greenhouse gas emissions. Fortunately, according to the Montreal Protocol, CFC gas has been banned since 2010, but the use of others continues, with HCFC estimated to be phased out by 2040 and an 80% reduction in HFC usage by 2047.[3,6]

Looking towards the future, CRT is based on liquid and gas-phase cooling which is being considered for replacement by other technologies. Currently, researchers are developing solid-state based technologies with utilizing the electric and magnetic properties of materials to replace them as they are deemed more efficient in terms of energy usage and size. The most used application based on electric properties is the thermoelectric system, which exploits the Seebeck effect.[7] Thermoelectric technology has several advantages such as not having a moving parts, different operating temperature ranges, and flexibility which allows it to be used as a cooling

Dicky Rezky Munazat

Dicky Rezky Munazat obtained his Bachelor's in Physics (2018) and Master's degrees in Materials Science from Universitas Indonesia (2020). He is a research assistant and support staff at Department of Physics, Universitas Indonesia. He is currently pursuing a Doctoral degree in Materials Science at the Department of Physics, Universitas Indonesia, under the guidance of Dr Budhy Kurniawan and Dr Maykel T. E. Manawan. His research interests are synthesized and characterized ceramic magnetic materials by X-ray/Neutron diffraction crystallography analysis, and the properties of magnetic materials, including colossal magnetoresistance and the magnetocaloric effect.

Maykel T. E. Manawan

Maykel T. E. Manawan obtained his Bachelor's, Master's, and PhD degrees in Physics (2005, 2009, 2014) from Universitas Indonesia. Currently, he is a lecturer at Universitas Pertahanan Indonesia (since 2018) and a researcher at the National Research and Innovation Agency (since 2022). In other experiences, he joins and works in the International Center for Diffraction Data (ICDD since 2020) and Bruker-AXS Indonesia (since 2017). His research interests are the application of crystallography, quantum crystallography, X-ray/Neutron diffraction analysis, batteries, magnetic materials, and materials science.

Darminto Darminto

Darminto Darminto graduated from PhD program in Physics, at Institut Teknologi Bandung, Indonesia (2000) and continued the post-doctoral research program at Twente University, The Netherlands (2001–2003). Returned then as a lecturer at the Physics Department, Institut Teknologi Sepuluh Nopember, Surabaya, Indonesia, he was appointed as a professor of condensed matter physics in 2011. Apart from collaborating with RIKEN Nishina Center since 2009, Federal Institute for Materials Research and Testing (BAM), Germany (since 2013) and Synchrotron Light Research Institute, Thailand (since 2016). His current research interest focuses on superconductivity, magneto-electronics, nano- and 2D-materials.

Budhy Kurniawan

Budhy Kurniawan obtained his Bachelor's and Master's degrees in Physics (1992 & 1995) from Universitas Indonesia and he received his PhD in the Field of Condensed Matter Physics from Tokyo Institute of Technology, Japan (2000). Currently, he is an Associate Professor at the Department of Physics, Universitas Indonesia. His research interests are the characterization and properties of quantum spin systems and magnetic materials such as static and dynamic magnetic properties of NH_4CuCl_3, magnetoresistance, magnetocaloric effect, microwave absorber materials, multiferroics materials and also thermoelectric phenomena.

This journal is © the Owner Societies 2024

Phys. Chem. Chem. Phys., 2024, **26**, 14476–14504 | **14477**

alternative. However, after more than 20 years of development, it still suffers from low energy conversion efficiency.[7] This has led researchers to seek alternative options by leveraging the properties of the magnetocaloric effect, namely magnetic refrigeration technology (MRT).[4,8,9] MRT possesses superior properties compared to CRT, including energy efficiency, compact and portable size, cooling efficiency cycles of 30–60%, and the absence of harmful gases due to its environmentally friendly solid-based composition.[4,10] However, the assembly cost of MRT is estimated to be nearly two-thirds of the total cost, posing a significant obstacle to its widespread adoption. Despite that looking at other benefits this assembly cost can be offset by its higher thermodynamic cycles, which are 1 to 2 times greater than CRT, thereby impacting economic competition.[11]

Research on MRT materials is often associated with their magnetism. Their presence has a significant appeal to researchers and technicians, prompting them to do depth studies. Some intriguing phenomena can be explored, such as microwave absorber properties, magnetostriction, magnetoresistance,[12–15] magnetocaloric effect,[1,4,16,17] multiferroic properties,[7] and others. One of the phenomena that has been intensively developed for the application of MRT is the magnetocaloric effect (MCE). The MCE is an intrinsic property of magnetic materials that, when subjected to a magnetic field, induces changes in magnetic entropy ($-\Delta S_M$) and adiabatic temperature changes (ΔT_{ad}), which can assist in controlling environmental temperature by increasing or decreasing it.[18,19]

The phenomenon of MCE was discovered by Weiss and Piccard, who studied nickel samples reported in 1917 and 1918 regarding the discovery of heat around the Curie temperature (T_C). This temperature marks the transition from ferromagnetic to paramagnetic material when subjected to a magnetic field.[7] Furthermore, they also distinguished between reversible effects and heating caused by hysteresis. In 1926, Debye and Giauque discovered the MCE phenomenon in paramagnetic salt materials. After a long time of undeveloped research related to an MCE, brown investigated pure gadolinium (Gd), in 1976 year, as a potential material for magnetic refrigeration applications. Gadolinium stood out due to its favorable properties, such as a Curie temperature (T_C) of 294 K around room temperature, magnetic entropy change of 10.2 J kg^{-1} K^{-1}, and relative cooling power of 410 J kg^{-1} under a magnetic field of 5 T.[20,21] This remarkable discovery of MCE materials has potential applications in magnetic refrigeration and cancer treatment using hyperthermia methods.[22] Therefore, Gd has become the standard reference for ideal MCE materials.[16,23–27] However, satisfactory results have not been yet achieved in practical applications. The main challenge in the expensive development of MRT is the use of Gd as a material, which has a high ($4000 per kg), and limited availability.[17] Therefore, there is a need for alternative materials that are more affordable and abundantly available in nature.

Several alternative MCE materials have been developed by researchers to address these challenges. Fig. 1(A) illustrates the progress of MCE material research from 2010 to 2023. Research

on MCE materials has progressed rapidly, resulting in various potential MCE materials, as shown in Fig. 1(B). To date, innovative types of materials include Heusler alloys,[28,29] LaFe$_{13-x}$Si$_x$ alloys,[30–33] Fe-based alloys,[34] MnAs,[35] spinel ferrites,[36–38] perovskite magnanites,[9,15–17,27,39–41] double perovskites,[19] and composite.[42–44] This was aimed at obtaining MCE materials with ideal criteria for magnetic refrigeration applications. Based on the criteria proposed by Phan *et al.*, perovskite manganites have the potential as a permanent magnetic refrigeration applications.[4] Therefore, in this study, we will discuss the MCE phenomenon in general, the development of various types of materials, and a detailed discussion on perovskite manganites.

2. Fundamental aspects

2.1 Theory of magnetocaloric effect

The MCE properties represented by the two expressions consist of a change in the magnetic entropy ($-\Delta S_M$) and the adiabatic temperature change (ΔT_{ad}). In the concept of entropy (S), a measure of the degree of disorder in thermodynamics, a system can be adjusted by changing its magnetic field, temperature, or other thermodynamic parameters.[1] Thus, in an adiabatic state, the total entropy in the system has three entropy component values, as shown in eqn (1):[45]

$$S_T(H, T) = S_M(H, T) + S_l(T) + S_e(T) \tag{1}$$

where S_T is the total entropy of the system, S_M is the magnetic entropy, S_l is the lattice entropy, and S_e is the electronic entropy. It is known that S_M depends on the temperature and magnetic field, while S_l and S_e only depend on temperature.[1] That makes the value of MCE associated with S_M and $-\Delta S_M$, with the latter being one of the crucial parameters influencing environmental temperature changes.

Fig. 2 depicts a simple mechanism of the magnetocaloric effect phenomenon. When the magnetic material is without a magnetic field ($H_1 = 0$ T), the magnetic spin moments appear randomly resulting in a significant value of S_M. If the magnetic field is applied ($H_2 > 0$ T), an adiabatic magnetization process occurs that causes rotating magnetic spin moments of atoms reducing the value of S_M.[4] This has adiabatically occurred with a constant S value, so the decrease in S_M increases the values in S_l value, influencing the rise in material temperature due to lattice vibrations or phonons and the value of $-\Delta S_M \ll 0$.[46] the excess heat in the system quickly dissipates into the environment through a medium such as air, water, water–alcohol, *etc.* when a magnetic field is applied to materials. This condition increases the ΔT_{ad} value. After the magnetic field is removed ($H_3 = 0$ T), an adiabatic demagnetization process and the direction of the random magnetic spin moments occur. This causes an increase in S_M and a decrease in S_l, resulting in a decrease in the temperature of the system with the value of $-\Delta S_M \gg 0$. Therefore, the system absorbed heat from the environment to return to equilibrium, causing a decrease in
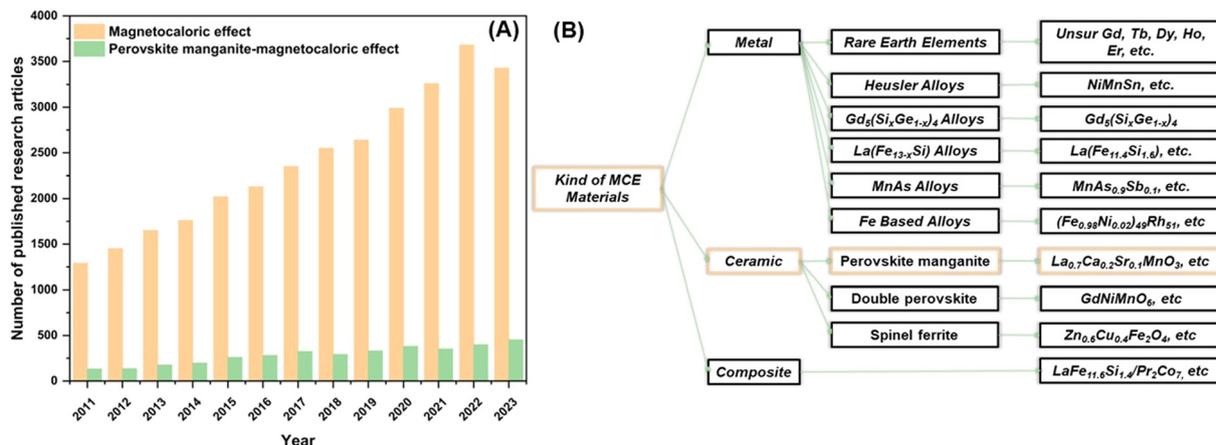
14478 | *Phys. Chem. Chem. Phys.*, 2024, **26**, 14476–14504

This journal is © the Owner Societies 2024

Fig. 1 (A) The number of published research articles on magnetocaloric effect based on magnetic materials using search keywords "magnetocaloric effect" and "perovskite manganite magnetocaloric effect" from Google Scholar accessed on January 4, 2024, and (B) a classification diagram of various magnetocaloric effect materials.
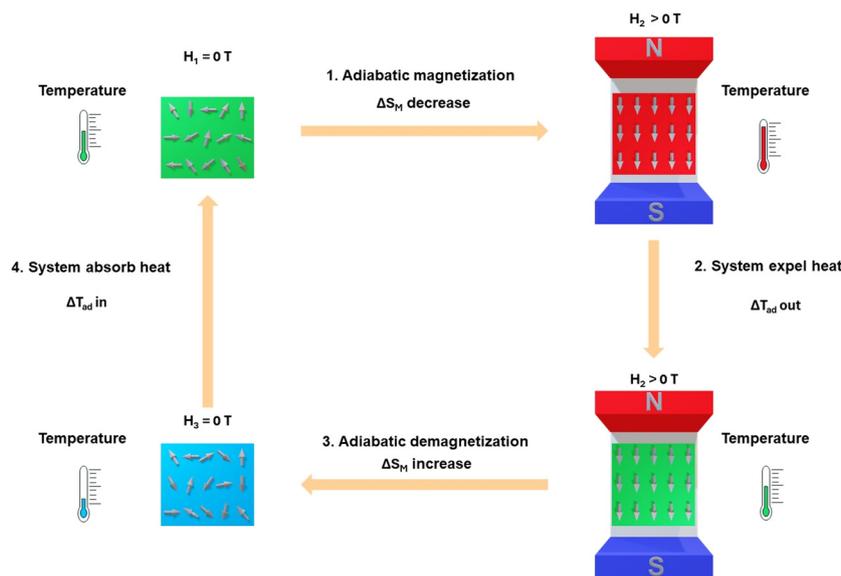

Fig. 2 Schematic diagram of the mechanism of magnetocaloric effect properties.

the environmental temperature accompanied by a decrease in ΔT_{ad} value.[46] If this process is repeated, then a reversible cycle is created.

2.2 Relation between magnetic entropy and adiabatic temperature change

Based on the mentioned definition, the MCE properties can be expressed using parameters $-\Delta S_{\text{M}}$ and ΔT_{ad} with thermodynamic aspects. In general, the value of $-\Delta S_{\text{M}}$ isothermal under a magnetic field change, $\Delta H = H_2 - H_1$, can be defined as follows:

$$\Delta S_{\text{M}}(T, \Delta H) = S_{\text{M}}(T, H_2) - S_{\text{M}}(T, H_1) \qquad (2)$$

$$\Delta S_{\text{M}}(T, \Delta H) = dS_{\text{M}}(T, \Delta H) \qquad (3)$$

$$\Delta S_{\text{M}} = \int_{H_1}^{H_2} \left(\frac{\partial S}{\partial H}\right)_{\text{H,p}} dH \qquad (4)$$

By utilizing the Maxwell relationship equation expressed in eqn (5) as a function of magnetization (M), magnetic field (H), and temperature (T) under constant pressure (p).

$$-\left(\frac{\partial S}{\partial H}\right)_{\text{T,p}} = \left(\frac{\partial M}{\partial T}\right)_{\text{H,p}} \qquad (5)$$

Therefore, if eqn (5) is substituted into eqn (4), the formula for $-\Delta S_{\text{M}}$ can be obtained by utilizing indirect measurements as follows eqn (6):

$$-\Delta S_{\text{M}} = \int_{H_1}^{H_2} \left(\frac{\partial M}{\partial T}\right)_{\text{H,p}} dH \qquad (6)$$

This journal is © the Owner Societies 2024

Phys. Chem. Chem. Phys., 2024, **26**, 14476–14504 | **14479**

Indirect measurements such as measuring magnetization at discrete magnetic fields and temperature intervals, where $-\Delta S_M$ can be expressed by the following equation:

$$(-\Delta S_M)_i = \sum_j \frac{M(T_{i+1} - H_j) - M(T_i - H_j)}{T_{i+1} - T_i}(H_{j+1} - H_j) \quad (7)$$

where $(-\Delta S_M)_i$ is the magnetic entropy change at temperature T_i, M_i and M_{i+1} are the magnetizations at T_i and T_{i+1}, H_j is the magnetic field.

On the other hand, there is another parameter, ΔT_{ad}, to know the performance of the MCE properties from direct measurements such as measuring the capacity against the magnetic field. Using the second law of thermodynamics equation regarding entropy and specific heat capacity (C_P), eqn (8) is obtained:

$$C_P = T\left(\frac{dS}{dT}\right) \quad (8)$$

To obtain the equation for ΔT_{ad}, eqn (8) is substituted into eqn (3), resulting in

$$\Delta S_M(T, \Delta H) = \frac{C_P(T, \Delta H)}{T}dT \quad (9)$$

Based on eqn (9), it can be evaluated to obtain the equation for ΔT_{ad}, given as follows:

$$\Delta T_{ad} = -\int_{H_1}^{H_2} \frac{T}{C_P(T, \Delta H)}\left(\frac{\partial M}{\partial T}\right)_{H,p} dH \quad (10)$$

From eqn (6), (8) and (10), it can be concluded that every magnetic material exhibiting MCE will perform well if it has high values of $-\Delta S_M$ and ΔT_{ad}. Both of these values will be high when the value of $\left(\frac{\partial M}{\partial T}\right)_{H,p}$, the magnetic entropy change with temperature at a constant magnetic field and pressure, is large and C_p, the heat required to increase the temperature by 1 °C for 1 kg of mass, is small at the same temperature.[1,4,39] The value of $\left(\frac{\partial M}{\partial T}\right)_{H,p}$ increases the maximum at around T_C, which may be associated with enhancing the maximum MCE value.

2.3 Determination of magnetic cooling capability

In addition to measuring ΔT_{ad}, $-\Delta S_M$ and C_p, other important parameters characterizing the MCE properties are related to the magnetic cooling capability of the MCE material.[1] These parameters divided into two definitions are relative cooling power (RCP) and refrigerant capacity (RC). Both represent the amount of heat available for transfer between the hot and cold sides in one ideal Carnot cycle.[39,47,48]

The calculation of RCP is related to the value of $-\Delta S_M$ and can be defined as follows:[9,41,44]

$$RCP = |-\Delta S_M^{max}| \times \delta T_{FWHM} \quad (11)$$

where, $-\Delta S_M^{max}$ is the maximum magnetic entropy change from $-\Delta S_M$ and δT_{FWHM} is the full width at half maximum (FWHM)

of $-\Delta S_M$ curve. This approach presents some problems, such as certain samples having wide $-\Delta S_M(T)$ curves with very small $-\Delta S_M$ values or narrow $-\Delta S_M(T)$ curves with very high $-\Delta S_M$ values. It may yield acceptable RCP values. However, in such cases, it may not be suitable for practical applications.[1] Furthermore, many researchers have assumed that $\delta T_{FWHM} = T_2 - T_1$, where T_2 and T_1 are the normalizations of the value $\frac{\Delta S_M}{\Delta S_M^{max}} = \frac{1}{2}$.[47,49]

The calculation of RC has a relationship with the value of $-\Delta S_M$ and can be defined as follows:[41,50,51]

$$RC = \int_{T_1}^{T_2} \Delta S_M(T, H)dT \quad (12)$$

where, T_2 is the temperature of the hot reservoir state, and T_1 is the temperature of the cold reservoir state. It is worth noting that if the measured material exhibits hysteresis, steps are required to eliminate losses due to hysteresis to obtain a clean RC value.[1,35]

2.4 Relation between magnetic behavior and types of magnetic phase transition

It is known that determining the order of the magnetic phase transition between the ferromagnetic and paramagnetic states is usually carried out through a thermodynamic sense, such as utilizing the first derivatives of Gibbs free-energy with parameters such as temperature, pressure, magnetic field, *etc.*, which can be observed from the resulting curves. Many researchers have reported two types of magnetic phase transition orders based on the results of these curves.[1,4,7,16,17,41,47,48,52–57] If the first derivative results in a discontinuous curve marked by a magnetic phase transition at critical points within a very narrow temperature range, such as changes in entropy, volume, and magnetization values, it is known as the behavior of a first-order magnetic phase transition (FOMT).[54,55,57] This phenomenon often occurs when the magnetic transition (dis)order–order occurs parallel to changes in the underlying crystal lattice, which is associated with magnetostructural transformations accompanied by the emergence of hysteresis.[1,34,54] The advantage of FOMT is its significant value of $-\Delta S_M$ for applications in magnetic refrigeration technology (MRT). However, FOMT exhibits significant magnetic and thermal hysteresis, leading to losses in the performance of the MCE properties and a very narrow operating temperature range.[52,54] Examples of materials that exhibit FOMT include $La(Fe,Si)_{13}$,[58] $Gd_5Si_2Ge_2$,[59] $MnAs_{1-x}Sb_x$,[35] $Ni_{65}Mn_{20}Ga_{15}$,[28] and $(Fe_{0.98}Ni_{0.02})_{51}Rh_{49}$ alloys.[34] On the other hand, if the first derivative presents a continuous curve marked by a magnetic phase transition at critical points with a broad temperature range, this behavior is known as a second-order magnetic phase transition.[53,56] The advantage of materials exhibiting SOMT behavior is that SOMT materials have a broad operating temperature range and small magnetic and thermal hysteresis, although the value of $-\Delta S_M$ is slightly lower than FOMT.[1] Small magnetic and thermal hysteresis can disregard the presence of losses in the performance and cycle reversibility of the MCE properties in MRT. Examples of materials exhibiting SOMT behavior include

14480 | *Phys. Chem. Chem. Phys.*, 2024, **26**, 14476–14504

This journal is © the Owner Societies 2024

$La_{0.55}Ca_{0.05}Sr_{0.40}MnO_3$,[60] $La_{0.05}Pr_{0.1}Sr_{0.35}MnO_3$,[61] $Zn_{0.6}Cu_{0.4}Fe_2O_4$,[62] $CoGa_{1.2}Fe_{0.8}O_4$,[36] and others.

2.5 Ideal criterion of MCE materials

The remarkable discovery of MCE properties in pure Gd by Brown has been used as the standard reference for ideal MCE materials until now.[16,23,26,27,63,64] According to a summary by Phan and Yu, the ideal criteria for MCE materials for magnetic refrigerator applications include several aspects listed as follows:[4]

a. Large values of $-\Delta S_M$ and ΔT_{ad}.

b. Small lattice entropy (high Debye temperature).

c. Curie temperature around room temperature, *i.e.*, 300 K.

d. The MCE properties have a broad working temperature range, such as 10–80 or >250 K.

e. Magnetic hysteresis approaching zero, associated with the reversibility of MCE in magnetic refrigerators.

f. Small thermal hysteresis linked to the reversibility of MCE in magnetic refrigerators.

g. Small specific heat capacity and high thermal conductivity, ensuring remarkable temperature changes and heat exchange rates.

h. Large electrical resistance associated with low eddy current heating or minimal losses.

i. High chemical stability, easy sample synthesis, and cost-effective materials for magnetic refrigerator applications.

2.6. Types of MCE measurements

2.6.1 Direct measurement method. The direct method involves placing a thermometer on the experimental material, and the value of ΔT_{ad} can be directly determined additionally, direct measurement methods can be employed to obtain C_p data. Direct measurement methods show an accuracy in the range of 5–10% and depend on errors in thermometry, errors in field settings, the quality of thermal insulation on the sample, and the quality of the compensation scheme to eliminate the effects of changes in magnetic fields in temperature sensor readings.[1,4,52] However, it should be noted that the tools used for direct measurement methods are sensitive and require careful to collect data.

2.6.2 Indirect measurement method. Indirect measurements were carried out to obtain magnetization data for calculating the change in magnetic entropy. The accuracy of magnetization data measurements has a relatively high error (20–30%), whereas calculating MCE from heat capacity data shows better accuracy than other techniques at low temperatures.[4] Indirect methods can be performed using two approach calculations. The first method involves utilizing data measuring the temperature dependence on magnetization under varying magnetic fields or data measuring the dependence of magnetic fields on isothermal magnetization.[1,4,52]

3. Challenges and various types of MCE materials for future application

A brief explanation of the characterization and main properties of the MCE material based on its classification is provided in

Table 1 Comparison of ideal MCE parameters for types of MCE materials in the classification of metals and ceramics

No.	Materials	Ideal MCE parameters							
		A*	B*	C*	D*	E*	F*	G*	H*
Metals									
1	Pure of rare earth elements		✓	✓	✓	✓	✓	✓	✓
2	Heusler alloys	✓	✓	✓					✓
3	$Gd_5(Si_{4-x}Ge_x)$ alloys		✓	✓					✓
4	$La(Fe_{13-x}Si_x)$ alloys	✓	✓						✓
5	Fe-based alloys	✓	✓						✓
6	MnAs alloys	✓	✓	✓	✓	✓	✓		
Ceramics									
1	Perovskite manganite	✓	✓		✓	✓	✓	✓	✓
2	Double perovskite	✓	✓		✓	✓			✓
3	Spinel ferrite	✓			✓	✓	✓	✓	✓

Note: * (A) inexpensive and easily obtainable material, (B) large and easily controllable $-\Delta S_M$ and RCP values, (C) Curie temperature close to or easily adjustable to room temperature (300 K), (D) wide MCE working temperature range such as 10–80 K, (E) low thermal and magnetic hysteresis, (F) easy production or synthesis processes, (G) good chemical stability, (H) non-toxic and environmentally friendly.

this section. The aim was to categorize MCE materials based on the compositions from previous studies. However, this concise discussion focuses on MCE materials for MRT applications near room temperature. According to previous studies, MCE materials can be classified into three categories consist of metals, ceramics, and composites.[1,4,5,19,22,31,35,59,64] For more details, the classifications of metals and ceramics are summarized in Table 1. However, in this section, we will also explain the development of challenges and efforts to achieve MRT applications in the future in general for all existing alternative materials.

3.1 Challenges and strategies for future MRT application

Based on the background mentioned, homework still needs to be completed to achieve future MRT applications. In addition to the challenges in the economic aspect, prototype development, and sustainability optimization are expected to be the next challenges. These challenges include reducing the heat exchange time between the materials and heat exchangers,[65] integrating thermal change controls,[65,66] minimizing losses due to magnetic hysteresis,[58] enhancing mechanical stability and thermodynamic cycle sustainability,[11] and achieving good MCE performance at low magnetic field strengths and over a wide temperature range.[4,52] Efforts to solve these challenges have been undertaken by researchers, primarily using strategies such as (i) selecting alternative materials, (ii) adjusting chemical stoichiometry, (iii) modifying external parameters (pressure, magnetic field, and temperature), (iv) utilizing fluid mediums, and (v) reducing the size.[4,65] Further discussions on strategies (i), (ii), and (iii) will be addressed in the following sections.

Principally, the magnetocaloric effect can induce local heating and cooling associated with the transfer of heat from the system to the environment. This gap has been exploited by researchers to explore fluid mediums to enhance their

magnetocaloric effect properties. The development of fluid mediums in heat transfer extends beyond air alone but also includes water, alcohol, water–alcohol mixtures, liquid mercury, liquid sodium–potassium, and GaInSn liquid alloys.[4,11] The use of GaInSn alloy-based heat transfer fluids has attracted attention for further study because of their non-toxic nature at room temperature,[11] thermal conductivity 27 times greater than that of water enabling faster heat transfer,[67] and a specific heat value of 1/14 that of water allowing for higher temperatures to be achieved in MRT.[68] Moreover, it is estimated that using this medium can reduce the size of system components and costs for MRT production, promising for the future. Furthermore, at high frequencies, the GaInSn liquid alloy is estimated to be more than 2.5 times cheaper than water–alcohol mixtures.[11] For example, Rajamani et al. investigated the use of GaInSn as a heat transfer medium with La(Fe,Mn,Si)$_{13}$H$_z$, presenting the stability of the magnetocaloric material for 1.5 years and the compatibility of the GaInSn liquid alloy heat transfer medium as a cheaper, more effective, and sustainable medium in MRT systems.[11]

In addition, size reduction strategies are expected that will play a significant role in their magnetic properties.[69–74] Furthermore, the interest in reducing the size from micro to nanoscale can provide opportunities for other developments such as hyperthermia or drug delivery,[75] thermal switchers,[65,66] energy harvesting devices,[76] etc. However, this review will focus on MRT applications. Generally, size reduction strategies from micro to nanoscale in MCE materials can affect the broadening of the magnetic phase transition, resulting in a broader working temperature range, a decrease in saturation magnetization, and $-\Delta S_M$ value.[51,65,77–80] These changes are associated with disturbances such as strain fields, atomic disorder, uncompensated surface spins, chemical inhomogeneity, grain size distribution, etc.[65] For example, Zeng et al. reduced the size of Gd material to as small as 15 nm, resulting in a reported decrease in the $-\Delta S_M$ value by up to 50% compared with micro-sized samples.[81] However, this size reduction can alter the characteristics of the magnetic phase transition from the first order to the second order, characterized by a broadening of the working temperature range.[65] Similar results were also obtained with other materials such as Gd$_{5.09}$Ge$_{2.03}$Si$_{1.88}$,[82] La–Fe–Si,[83] and La$_{0.7}$Ca$_{0.3}$MnO$_3$,[84] where larger particle sizes could maintain significant MCE values.[81–84] Therefore, future strategies need to be developed not only for the base material but also for fluid media and grain size considerations to obtain more effective MCE materials ready to replace CRT.

3.2 Metal materials

3.2.1 Pure of rare earth elements. The discovery of remarkable MCE properties in the Gd element makes it one of the best MCE materials in this group. The Gd material has a $-\Delta S_M$ value of 10.2 J kg^{-1} K^{-1} with a T_C value of 294 K and an RCP value of 410 J kg^{-1} under a magnetic field of 5 T.[4] The emergence of MCE properties in Gd is due to its placement in the 4f group and having the largest magnetic spin moment. Additionally, rare earth metals exhibit different magnetic structures due to

indirect oscillations in the localized 4f magnetic moment through electron conduction.[85] Furthermore, Ayas et al. reported that rare earth metals have larger crystal field interactions than exchange interactions in light rare earth pure elements. On the other hand, the opposite condition occurs in heavy rare earth pure elements.[1] In addition to Gd, other materials have also been investigated, such as terbium (Tb), dysprosium (Dy), holmium (Ho), erbium (Er), and thulium (Tm), as listed in Table 2.[45] Unfortunately, the high cost and limited availability restrict the use of pure rare earth metals for MRT applications.

3.2.2 Heusler alloys. Heusler alloys, also commonly known as shape memory alloys, were discovered in the late 19th century and have been extensively researched to this day. Since their initial discovery, Heusler alloys have grown to include more than 1500 members. The structural characteristic of these materials include face-centered cubic (FCC) and body-centered cubic (BCC) unit cells. Heusler alloys have two general formulas both A$_2$BC (full Heusler) and ABC (half Heusler), where A and B are filled with transition metal elements, and C is filled with elements from groups III–IV A.[86,87] Fig. 3(A) illustrates the structure of full Heusler (a) and half Heusler (b).

Heusler alloys, such as Ni–Mn–Ga, have been extensively developed due to their exceptional MCE properties resulting from the FOMT behavior and the transformation from ferromagnetic austenite to weakly magnetic martensite.[29,88–94] Zheng et al. reported Ni$_{44}$Co$_6$Mn$_{37}$In$_{13}$ alloy, and described the martensitic phase transition under a magnetic field. The results showed values of $-\Delta S_M$ = 9.8 J kg^{-1} K^{-1} and RCP = 221.7 J kg^{-1} occurring around T_C = 419.5 K under a magnetic field 6 T. However, the Ni$_{44}$Co$_6$Mn$_{37}$In$_{13}$ alloy exhibited thermal and magnetic hysteresis, resulting in losses in MCE properties.[29] Furthermore, Datta et al. conducted research on Ni–Mn–Ga-based materials with varying compositions, including Ni$_{50}$Mn$_{27}$Ga$_{23}$ (NMG-1), Ni$_{54}$Mn$_{21}$Ga$_{25}$ (NMG-2), and Ni$_{54}$Mn$_{25}$Ga$_{21}$ (NMG-3). Different types of magnetic phase transitions were observed, with SOMT behavior for NMG-1, NMG-2, and FOMT behavior for NMG-3. Although the $-\Delta S_M$ values were lower than those reported by Zheng et al., it is crucial to note that differences in the composition can influence the type of magnetic phase transition.[95] Additionally, Ni–Mn–X alloys with X = In, Sn, and Sb have been found to exhibit $-\Delta S_M$ values in the range of 11.85 to 20.00 J kg^{-1} K^{-1}.[94] Kutynia and Gebara reported on Mn$_{1-x}$Zr$_x$CoGe materials with x = 0.03, 0.05, 0.07, and 0.1, showing $-\Delta S_M^{max}$ values with a range 2.94 to 13.42 J kg^{-1} K^{-1}.[87] In summary, the investigations mentioned above indicate that composition, structure, and doping determination play crucial roles in determining the magnetocaloric properties of Heusler alloys. The comprehensive performance summary of MCE in Heusler alloys is provided in Table 2.

3.2.3 Gd$_5$(Si$_x$Ge$_{1-x}$)$_4$ alloys. The development of Gd-based materials, such as Gd$_5$(Si$_x$Ge$_{1-x}$)$_4$, has attracted attention due to their excellent magnetic properties.[59] Fig. 3(B) illustrates the crystal structure transformation at specific temperatures, categorized into three regions. For the range $0.5 < x \leq 1$, an orthorhombic crystal structure of the Gd$_5$Si$_4$ type is presented

14482 | *Phys. Chem. Chem. Phys.*, 2024, **26**, 14476–14504

This journal is © the Owner Societies 2024

Table 2 List MCE performance from previous researches

Material	Sample form, heat treatment ($T(K)/t$)	Grain size (nm)	T_C (K)	$\lvert-\Delta S_M\rvert$ (J kg^{-1} K^{-1})	ΔH (T)	RCP (J kg^{-1})	Transition order	Ref.
Metals								
Pure rare-earth elements5								
Gd	—	—	294	11.2		—	—	45
Tb	—	—	230	15.7	6	—	—	45
Dy	—	—	180	13.5	6	—	—	45
Ho	—	—	134	1.8	6	—	—	45
Er	—	—	85	1.2	6	—	—	45
Tm	—	—	56	—	—	—	—	45
Heusler alloys								
$Ni_{50}Mn_{27}Ga_{23}$	Arc-M, (1173/24 h)	—	350	1.98	3	235.8	2	95
$Ni_{54}Mn_{21}Ga_{25}$	Arc-M, (1173/24 h)	—	322	1.90	3	161.5	2	95
$Ni_{54}Mn_{25}Ga_{21}$	Arc-M, (1173/24 h)	—	345	3.53	3	144.7	1	95
$Ni_{2.16}Mn_{0.84}Ga$	Arc-M, (1073/48 h)	—	339	7.3	14	—	1	93
$Ni_{42}Mn_{43}Cr_4Sn_{11}$	Arc-M, (1173/24 h)	—	168.2	8.7	6	284.2	1	88
$Ni_{42}Mn_{43}Cr_4Sn_{11}$	Arc-M, (1173/24 h)	—	291.1	5.04	6	234.1	2	88
$Ni_{50}Mn_{25}Sn_{25}$	MW, (−)	—	—	1.4	2	—	2	89
$Ni_{65}Mn_{20}Ga_{15}$	Nanowire (−)	—	~350	2.5	2	—	1	28
Ni_2MnGa	Arc-M, (−)	—	375	0.35	0.27	—	—	195
$Ni_{44}Mn_{45}Sn_{11}$	Arc-M, (1173/24 h)	—	237	7.2	5	122	1	196
$Ni_{44}Mn_{44}Fe_1Sn_{11}$	Arc-M, (1173/24 h)	—	262.5	21.3	5	172	1	196
$Ni_{44}Mn_{43}Fe_2Sn_{11}$	Arc-M, (1173/24 h)	—	288.5	21.2	5	90	1	196
$Ni^{44}Co_6Mn_{37}In_{13}$	Arc-M, (1173/48 h)	—	419.5	9.8	5	221.7	—	29
$Mn_{49}Ni_{42}Sn_9$	Arc-M, (1173/72 h)	—	315.1	—	5	—	1	197
$Mn_{49}Ni_{41}Co_1Sn_9$	Arc-M, (1173/72 h)	—	304.8	34.5	5	—	1	197
$Mn_{49}Ni_{39}Co_3Sn_9$	Arc-M, (1173/72 h)	—	266.3	36.5	5	—	1	197
$Mn_{49}Ni_{37}Co_5Sn_9$	Arc-M, (1173/72 h)	—	217.5	39.9	5	—	1	197
$Mn_{0.97}Zr_{0.03}CoGe$	Arc-M, (−)	—	290	6.93	5	195	—	87
$Mn_{0.95}Zr_{0.05}CoGe$	Arc-M, (−)	—	285	13.42	5	425	—	87
$Mn_{0.93}Zr_{0.07}CoGe$	Arc-M, (−)	—	283	3.96	5	246	—	87
$Mn_{0.90}Zr_{0.10}CoGe$	Arc-M, (−)	—	278	2.94	5	219	—	87
$Gd5(Si_xGe_{1-x})_4$ alloys								
$Gd_5Si_2Ge_2$	—, (−)	—	276	18.4	5	535	—	59
$Gd_5Si_2Ge_2$ (0 kbar)	Arc-M, (1300/1 h)	—	~275	~28.5	5	—	1	99
$Gd_5Si_2Ge_2$ (0.7 kbar)	Arc-M, (1300/1 h)	—	~273	~21.5	5	—	1	99
$Gd_5Si_2Ge_2$ (1.5 kbar)	Arc-M, (1300/1 h)	—	~278	~19.6	5	—	1	99
$Gd_5Si_2Ge_2$ (2.7 kbar)	Arc-M, (1300/1 h)	—	~284	~15.8	5	—	1	99
$Gd_5Si_2Ge_2$ (3.4 kbar)	Arc-M, (1300/1 h)	—	~292	~13.4	5	—	1	99
$Gd_5Si_2Ge_2$ (4.2 kbar)	Arc-M, (1300/1 h)	—	~294	~12.1	5	—	1	99
$Gd_5Si_2Ge_2$ (5.9 kbar)	Arc-M, (1300/1 h)	—	~303	~7.3	5	—	1	99
$Gd_5Si_2Ge_2$ (9.2 kbar)	Arc-M, (1300/1 h)	—	~307	~7.1	5	—	1	99
$Gd_5Si_2Ge_2$	Arc-M, (1573/1 h)	—	294	7.0	2	—	1	198
$Gd_5Si_2Ge_{1.98}Ga_{0.02}$	Arc-M, (1573/1 h)	—	295	~4.0	2	—	2	198
$Gd_5Si_2Ge_{1.96}Ga_{0.04}$	Arc-M, (1573/1 h)	—	298	~4.0	2	—	2	198
$Gd_5Si_2Ge_{1.984}Ga_{0.06}$	Arc-M, (1573/1 h)	—	298	~3.2	2	—	2	198
$Gd_5Si_{1.72}Ge_{2.28}$	Arc-M, (−)	—	247	13.73	2	—	1	199
$(Gd_{0.98}Tb_{0.02})_5Si_{1.72}Ge_{2.28}$	Arc-M, (−)	—	241	12.73	2	—	1	199
$(Gd_{0.96}Tb_{0.02})_5Si_{1.72}Ge_{2.28}$	Arc-M, (−)	—	237	18.85	2	—	1	199
$(Gd_{0.94}Tb_{0.02})_5Si_{1.72}Ge_{2.28}$	Arc-M, (−)	—	231	25.13	2	—	1	199
$(Gd_{0.92}Tb_{0.02})_5Si_{1.72}Ge_{2.28}$	Arc-M, (−)	—	230	16.90	2	—	1	199
$(Gd_{0.90}Tb_{0.10})_5Si_{1.72}Ge_{2.28}$	Arc-M, (−)	—	230	14.50	2	—	1	199
$Gd_5Ge_{2.04}Si_{1.94}Mn_{0.02}$	Arc-M, (1173/7 d)	—	293	19.8	5	357	1	98
$Gd_5Ge_{2.035}Si_{1.935}Mn_{0.06}$	Arc-M, (1173/7 d)	—	295	14.7	5	378	1	98
$Gd_5Si_{2.035}Ge_{1.935}Mn_{0.03}$	Arc-M, (1173/7 d)	—	295	11.6	5	220.1	1	200
$Gd_5Si_{2.01}Ge_{1.91}Mn_{0.08}$	Arc-M, (1173/7 d)	—	299	7.0	5	175.3	1	200
$Gd_5Si_2Ge_2$	—	—	262	8.1	1	—	—	100
$Gd_{4.5}Dy_{0.5}Si_2Ge_2$	—	—	252	7.7	1	—	—	100
$Gd_4Dy_1Si_2Ge_2$	—	—	243	7.5	1	—	—	100
$Gd_{3.5}Dy_{1.5}Si_2Ge_2$	—	—	231	7.6	1	—	—	100
$Gd_3Dy_2Si_2Ge_2$	—	—	220	7.5	1	—	—	100
$DyAl_2Ge_2$	SF, (1323/10 h)	—	8	12.0	7	275	—	201
$Dy_{0.5}Gd_{4.5}Si_2Ge_2$	Arc-M, (−)	—	—	~8.8	5.5	—	1	202
$Dy_3Gd_2Si_2Ge_2$	Arc-M, (−)	—	—	~13.9	5.5	—	1	202
$Dy_5Si_2Ge_2$	Arc-M, (−)	—	—	~6.9	5.5	—	1	202
$La(Fe_{13-x}Si_x)$ alloys								
$LaFe_{11.2}Si_{1.8}$	SC, (1373/10 h)	—	~182	16.8	2	—	1	30

This journal is © the Owner Societies 2024

Phys. Chem. Chem. Phys., 2024, **26**, 14476–14504 | **14483**

Table 2   (*continued*)

Material	Sample form, heat treatment (T(K)/t)	Grain size (nm)	T_C (K)	$\|-\Delta S_M\|$ (J kg^{-1} K^{-1})	ΔH (T)	RCP (J kg^{-1})	Transition order	Ref.
LaFe$_{11.2}$Si$_{1.8}$	SC-powder <100 μm, (1373/10 h)	—	∼182	10.6	2	—	1	30
LaFe$_{11.2}$Si$_{1.8}$	SC-powder <100–200 μm, (1373/10 h)	—	∼182	12.5	2	—	1	30
LaFe$_{11.2}$Si$_{1.8}$	SC-powder <200–300 μm, (1373/10 h)	—	∼182	12.8	2	—	1	30
LaFe$_{11.2}$Si$_{1.8}$	HPS-powder <100 μm, (753/25 m)	—	191	10.3	2	—	1	30
LaFe$_{11.2}$Si$_{1.8}$	HPS-powder <100–200 μm, (753/25 m)	—	187	11.1	2	—	1	30
LaFe$_{11.2}$Si$_{1.8}$	HPS-powder <200–300 μm, (753/25 m)	—	186	12.1	2	—	1	30
LaFe$_{11.2}$Si$_{1.8}$	SPS-powder <100 μm, (1223/5 m)	—	193	7.2	2	—	1	30
LaFe$_{11.2}$Si$_{1.8}$	SPS-powder <100–200 μm, (1223/5 m)	—	185	12.8	2	—	1	30
LaFe$_{11.2}$Si$_{1.8}$	SPS-powder <200–300 μm, (1223/5 m)	—	185	12.5	2	—	1	30
La$_{1.2}$Fe$_{11.6}$Si$_{1.4}$	Arc-M, (1273/30 m)	—	190	6.1	2	—	2	58
La$_{1.2}$Fe$_{11.6}$Si$_{1.4}$B$_{0.75}$	MS-R 5 m s^{-1}, (1273/30 m)	—	191	20.2	2	—	1	58
La$_{1.2}$Fe$_{11.6}$Si$_{1.4}$B$_{0.75}$	MS-R 10 m s^{-1}, (1273/30 m)	—	188	13.5	2	—	1	58
La(Fe$_{0.94}$Co$_{0.6}$)Si$_{1.6}$B$_{0.25}$	Arc-M, (1325/48 h)	—	285	6.70	3	174.2	2	203
La(Fe$_{0.92}$Ni$_{0.02}$Co$_{0.6}$)Si$_{1.6}$B$_{0.25}$	Arc-M, (1325/48 h)	—	293	4.63	3	166.7	2	203
La(Fe$_{0.90}$Ni$_{0.04}$Co$_{0.6}$)Si$_{1.6}$B$_{0.25}$	Arc-M, (1325/48 h)	—	303	3.77	3	154.1	2	203
La(Fe$_{0.88}$Ni$_{0.06}$Co$_{0.6}$)Si$_{1.6}$B$_{0.25}$	Arc-M, (1325/48 h)	—	311	3.12	3	136.8	2	203
La(Fe$_{0.86}$Ni$_{0.08}$Co$_{0.6}$)Si$_{1.6}$B$_{0.25}$	Arc-M, (1325/48 h)	—	319	2.97	3	—	2	203
La(Fe$_{0.84}$Ni$_{0.10}$Co$_{0.6}$)Si$_{1.6}$B$_{0.25}$	Arc-M, (1325/48 h)	—	329	1.99	3	—	2	203
LaFe$_{11.6}$Si$_{1.4}$(<100 μm)	Arc-M-SPS, (for SPS 1273/5 m forwad to 1323/24 h)	—	230	3.08	5	84	2	31
La(Fe$_{12.4}$Si$_{1.6}$)	Arc-M, (1273/30 d)	—	208	10.5	1	—	—	102
La(Fe$_{12.4}$Si$_{1.6}$)	Arc-M, (1273/30 d)	—	208	14.3	2	—	—	102
La(Fe$_{12.4}$Si$_{1.6}$)	Arc-M, (1273/30 d)	—	208	19.4	5	—	—	102
La$_{0.7}$Ce$_{0.3}$(Fe$_{0.92}$Co$_{0.08}$)$_{11.4}$Si$_{1.6}$	Arc-M, (1273/3 h)	—	—	4.1	2	—	2	204
La$_{0.7}$Ce$_{0.3}$(Fe$_{0.92}$Co$_{0.08}$)$_{11.4}$Si$_{1.6}$	Arc-M, (1273/3 h)	—	—	8.3	5	—	2	204
La$_{0.7}$Ce$_{0.3}$(Fe$_{0.92}$Co$_{0.08}$)$_{11.4}$Si$_{1.6}$	MS-R, (1273/3 h)	—	—	5.4	2	—	2	204
La$_{0.7}$Ce$_{0.3}$(Fe$_{0.92}$Co$_{0.08}$)$_{11.4}$Si$_{1.6}$	MS-R, (1273/3 h)	—	—	10.4	5	—	2	204
La$_{1.4}$Fe$_{10.92}$Co$_{0.88}$Si$_{1.2}$	HEBM, (1323/12 d)	—	292	3.74	2	129.4	2	205
La$_{1.4}$Fe$_{10.86}$Co$_{0.94}$Si$_{1.2}$	HEBM, (1323/12 d)	—	298	3.63	2	130.7	2	205
La$_{1.4}$Fe$_{10.82}$Co$_{0.98}$Si$_{1.2}$	HEBM, (1323/12 d)	—	301	4.00	2	138.0	2	205
La$_{1.4}$Fe$_{10.78}$Co$_{1.02}$Si$_{1.2}$	HEBM, (1323/12 d)	—	307	3.69	2	132.1	2	205
La$_{1.4}$Fe$_{10.72}$Co$_{1.06}$Si$_{1.2}$	HEBM, (1323/12 d)	—	310	3.65	2	136.1	2	205
La$_{1.4}$Fe$_{10.82}$Co$_{0.98}$Si$_{1.2}$	Arc-M, (1323/12 d)	—	296	5.35	2	130.5	2	205
La$_{0.9}$Ce$_{0.1}$Fe$_{11.5}$Si$_{1.5}$	Arc-M, (1373/15 d)	—	191	21.2	3	—	1	206
La$_{0.8}$Ce$_{0.2}$Fe$_{11.5}$Si$_{1.5}$	Arc-M, (1373/15 d)	—	∼186	27.4	3	—	1	206
La$_{0.7}$Ce$_{0.3}$Fe$_{11.5}$Si$_{1.5}$	Arc-M, (1373/15 d)	—	181	51.6	3	—	1	206
LaFe$_{11.5}$Si$_{1.5}$	Arc-M, (1373/9 d)	—	195	16.5	2	154.3	1	207
La$_{0.95}$Gd$_{0.05}$Fe$_{11.5}$Si$_{1.5}$	Arc-M, (1373/9 d)	—	196	15.3	2	140.2	1	207
La$_{0.9}$Gd$_{0.1}$Fe$_{11.5}$Si$_{1.5}$	Arc-M, (1373/9 d)	—	196	12.6	2	117.6	1	207
La$_{0.85}$Gd$_{0.15}$Fe$_{11.5}$Si$_{1.5}$	Arc-M, (1373/9 d)	—	198	9.5	2	110.2	2	207
La$_{0.8}$Gd$_{0.2}$Fe$_{11.5}$Si$_{1.5}$	Arc-M, (1373/9 d)	—	200	7.9	2	86.1	2	207
La$_{0.75}$Gd$_{0.25}$Fe$_{11.5}$Si$_{1.5}$	Arc-M, (1373/9 d)	—	204	6.8	2	90.9	2	207
La$_{1.0}$Fe$_{10.2}$Co$_{1.0}$Si$_{1.8}$	Arc-M, (1423/100 h)	—	312	2.0	1	68	2	32
La$_{1.0}$Fe$_{10.2}$Co$_{1.0}$Si$_{1.8}$	Arc-M, (1423/100 h)	—	312	3.6	2	162	2	32
La$_{1.0}$Fe$_{10.2}$Co$_{1.0}$Si$_{1.8}$	Arc-M, (1423/100 h)	—	312	4.9	3	255	2	32
MnAs alloys								
MnAs	HPRF, (1647/8 h)	—	311	47	5	—	1	109
MnAs	HPRF, (1647/8 h)	—	318	44	2	—	1	109
MnAs$_{0.9}$Sb$_{0.1}$	SVR, (1073/7 d)	—	280	30	5	—	1	110
MnAs$_{0.95}$Sb$_{0.05}$	SSR, (1073/7 h)	—	300	∼23.00	5	∼240	1	35
MnAs$_{0.90}$Sb$_{0.10}$	SSR, (1073/7 h)	—	288	∼22.50	5	∼260	1	35
MnAs$_{0.85}$Sb$_{0.15}$	SSR, (1073/7 h)	—	282	∼22.45	5	∼220	1	35
MnAs$_{0.80}$Sb$_{0.20}$	SSR, (1073/7 h)	—	276	∼22.43	5	∼240	1	35
MnAs$_{0.75}$Sb$_{0.25}$	SSR, (1073/7 h)	—	262	∼21.40	5	∼225	1	35
MnAs$_{0.70}$Sb$_{0.30}$	SSR, (1073/7 h)	—	242	∼20.30	5	∼245	1	35
Fe-based alloys								
(Fe$_{0.98}$Ni$_{0.02}$)$_{49}$Rh$_{51}$	Arc-M, (1273/10 d)	—	266	10.3	2	—	1	34
(Fe$_{70}$Ni$_{30}$)$_{89}$B$_{11}$	Arc-M, (973, 2 h)	—	381	0.31	1	100	2	208

14484 | *Phys. Chem. Chem. Phys.*, 2024, **26**, 14476–14504

This journal is © the Owner Societies 2024

Table 2 (*continued*)

Material	Sample form, heat treatment (T(K)/t)	Grain size (nm)	T_C (K)	$\lvert-\Delta S_M\rvert$ (J kg^{-1} K^{-1})	ΔH (T)	RCP (J kg^{-1})	Transition order	Ref.
$(Fe_{70}Ni_{30})_{89}B_{11}$	Arc-M, (973, 2 h)	—	381	1.46	5	641	2	208
$(Fe_{70}Ni_{30})_{99}Cr_1$	HEBM, (973, 2 h)	—	398	1.58	5	548	2	209
$(Fe_{70}Ni_{30})_{96}Cr_3$	HEBM, (973, 2 h)	—	323	1.49	5	436	2	209
$(Fe_{70}Ni_{30})_{95}Cr_5$	HEBM, (973, 2 h)	—	258	1.45	5	406	2	209
$(Fe_{70}Ni_{30})_{94}Cr_6$	HEBM, (973, 2 h)	—	245	1.22	5	366	2	209
$(Fe_{70}Ni_{30})_{92}Cr_7$	HEBM, (973, 2 h)	—	215	1.11	5	306	2	209
$Fe_{17}Pr_2$	HEBM, (—)	—	292	2.1	1.5	107	—	210
$Fe_{17}Pr_2$	HEBM, (—)	—	292	4.5	5	573	—	210
Ceramics								
Spinel ferrites								
$Zn_{0.6}Cu_{0.4}Fe_2O_4$	SG, (1373/24 h)	460	305	1.16	5	289	2	62
$Zn_{0.4}Ni_{0.2}Cu_{0.4}Fe_2O_4$	SG, (1373/24 h)	—	565	1.41	5	141	2	62
$Zn_{0.2}Ni_{0.4}Cu_{0.4}Fe_2O_4$	SG, (1373/24 h)	810	705	1.61	5	233	2	62
$Zn_{0.7}Ni_{0.3}Fe_2O_4$	SG, (1273/24 h)	—	327	0.67	2	112	2	38
$Zn_{0.7}Ni_{0.2}Cu_{0.1}Fe_2O_4$	SG, (1273/24 h)	—	296	0.64	2	117	2	38
$Zn_{0.7}Ni_{0.1}Cu_{0.2}Fe_2O_4$	SG, (1273/24 h)	—	282	0.62	2	124	2	38
$CoGa_{1.2}Fe_{0.8}O_4$	SSR, (1273/10 h)	—	210	1.51	5	27	2	36
$CoGa_{1.2}Fe_{0.8}O_4$	SSR, (1273/10 h)	—	210	1.23	4	18	2	36
$CoGa_{1.2}Fe_{0.8}O_4$	SSR, (1273/10 h)	—	210	1.00	3	12	2	36
$CoGa_{1.2}Fe_{0.8}O_4$	SSR, (1273/10 h)	—	210	0.7	2	7	2	36
$CoGa_{1.2}Fe_{0.8}O_4$	SSR, (1273/10 h)	—	210	0.4	1	3	2	36
$CoFe_2O_4$	SSR, (1473/6 h)	—	675	0.66	5	335.7	2	211
$Co_{8.875}Cr_{0.125}Fe_2O_4$	SSR, (1473/6 h)	—	740	1.98	5	128	2	211
$Co_{8.705}Cr_{0.250}Fe_2O_4$	SSR, (1473/6 h)	—	735	1.8	5	137	2	211
$Co_{8.675}Cr_{0.325}Fe_2O_4$	SSR, (1473/6 h)	—	731	1.76	5	145	2	211
$Co_{8.500}Cr_{0.500}Fe_2O_4$	SSR, (1473/6 h)	—	687	1.02	5	52	2	211
$Ni_{0.4}Cd_{0.3}Zn_{0.3}Fe_3O_4$	SG, (1173/24 h)	—	510	0.68	3	81.07	2	212
$Ni_{0.4}Cd_{0.3}Zn_{0.3}Fe_3O_4$	SG, (1373/24 h)	—	545	0.98	3	145.18	2	212
$Ni_{0.4}Cd_{0.3}Zn_{0.3}Fe_3O_4$	SG, (1173/24 h)	—	510	1.11	5	152.09	2	212
$Ni_{0.4}Cd_{0.3}Zn_{0.3}Fe_3O_4$	SG, (1373/24 h)	—	545	1.62	5	253.65	2	212
$Mg_{0.35}Zn_{0.65}Fe_2O_4$	SSR, (1573/12 h)	—	295	1.026	3	114.5	2	37
$Mg_{0.35}Zn_{0.65}Fe_2O_4$	SSR, (1573/12 h)	—	295	1.337	4	150.17	2	37
$Mg_{0.35}Zn_{0.65}Fe_2O_4$	SSR, (1573/12 h)	—	295	1.642	5	185.2	2	37
Double perovskites								
Gd_2NiMnO_6	SSR, (1623/—)	—	130	35	7	—	—	213
Gd_2NiMnO_6	SG, (1573/48 h)	—	130	3.7	5	—	2	127
Pr_2NiMnO_6	SSR, (1423/24 h)	—	215	4.9	5	—	—	214
Nd_2NiMnO_6	SSR, (1423/24 h)	—	191	2.3	5	—	—	214
Tb_2NiMnO_6	SSR, (1423/24 h)	—	110	5.2	5	—	—	214
Tb_2NiMnO_6	SG, (1573/48 h)	—	112	3.5	5	—	2	127
Ho_2NiMnO_6	SG, (1273/100 h)	—	86	6.4	5	—	—	214
Ho_2NiMnO_6	SG, (1473/48 h)	—	81.2	1.7	5	—	2	128
Ho_2NiMnO_6	SG, (1473/48 h)	—	101	3.4	5	175	2	215
Dy_2NiMnO_6	SSR, (1473/24 h)	—	97	5.2	7	—	—	216
Dy_2NiMnO_6	SG, (1473/48 h)	—	93	3.7	5	194	2	215
Er_2NiMnO_6	SG, (1473/48 h)	—	84	3.4	5	169	2	215
Eu_2NiMnO_6	SSR, (1473/24 h)	—	145	4.0	7	—	—	216
Eu_2NiMnO_6	SG, (1573/48 h)	—	143	3.2	5	—	—	127
Gd_2CoMnO_6	SSR, (1623/—)	—	112	24	7	—	—	213
Dy_2CoMnO_6	SG, (1373/48 h)	—	96	4.2	7	216	2	217
Ho_2CoMnO_6	SG, (1373/48 h)	—	85	4.6	7	275	2	217
Ho_2CoMnO_6	SG, (1473/48 h)	—	73.5	2.2	5	—	2	127
Er_2CoMnO_6	SG, (1373/48 h)	—	71	4.5	7	253	2	217
$Er_2Fe_{Cr}O_6$	SG, (1500/32 h)	—	11.7	11.95	5	215.8	2	218
$Tm_2Fe_{Cr}O_6$	SG, (1500/32 h)	—	10.5	4.76	5	123.5	2	218
Perovskite manganites								
$Pr_{0.7}Sr_{0.3}MnO_3$	SG, (973/5 h)	44	275	2.92	5	350	2	47
$Pr_{0.5}La_{0.2}Sr_{0.3}MnO_3$	SSR, (1623/24 h)	—	229	6.65	5	302.17	2	219
$Pr_{0.4}La_{0.3}Sr_{0.3}MnO_3$	SSR, (1623/24 h)	—	319	5.21	5	216.13	2	219
$Pr_{0.7}Sr_{0.3}MnO_3$	SSR, (1623/24 h)	—	263	3.38	1.8	50.00	—	169
$Pr_{0.7}Sr_{0.2}Ba_{0.1}MnO_3$	SSR, (1523/24 h)	—	231	~3.15	1.8	~62.00	—	169
$Pr_{0.7}Sr_{0.1}Ba_{0.2}MnO_3$	SSR, (1523/24 h)	—	200	~2.55	1.8	~70.00	—	169
$Pr_{0.7}Ba_{0.3}MnO_3$	SSR, (1523/24 h)	—	184	1.58	1.8	74.02	—	169
$Pr_{0.5}Eu_{0.1}Sr_{0.4}Mn$	SSR, (1623/60 h)	42.38	279.9	4.47	5	264.88	2	48
$Pr_{0.5}Er_{0.1}Sr_{0.4}Mn$	SSR, (1623/60 h)	51.68	188.5	4.86	5	270.00	2	48

This journal is © the Owner Societies 2024

Phys. Chem. Chem. Phys., 2024, **26**, 14476–14504 | **14485**

Table 2   (continued)

Material	Sample form, heat treatment (T(K)/t)	Grain size (nm)	T_C (K)	$\lvert -\Delta S_M \rvert$ (J kg^{-1} K^{-1})	ΔH (T)	RCP (J kg^{-1})	Transition order	Ref.
EuTi$_{0.8625}$Nb$_{0.0625}$Mn$_{0.075}$O$_3$	SSR, (1473/18 h)	—	5.5	34.7	5	364.9	2	49
EuTi$_{0.8375}$Nb$_{0.0625}$Mn$_{0.100}$O$_3$	SSR, (1473/18 h)	—	5.5	27.8	5	367.6	2	49
EuTi$_{0.8125}$Nb$_{0.0625}$Mn$_{0.125}$O$_3$	SSR, (1473/18 h)	—	6.5	23.2	5	369.2	2	49
EuTi$_{0.7875}$Nb$_{0.0625}$Mn$_{0.150}$O$_3$	SSR, (1473/18 h)	—	9.0	17.1	5	357.6	2	49
(Nd$_{0.5}$Sm$_{0.5}$)$_{0.5}$Sr$_{0.5}$MnO$_3$	SSR (1573/36 h)	—	188	∼2.85	5	∼183	2	171
LaMnO$_3$ bulk	SG, (1673/36 h)	—	124	2.69	5	250	2	142
LaMnO$_3$	SG, (1673/36 h)	200	135	2.67	5	355	2	142
LaMnO$_3$	SG, (1673/36 h)	40	150	2.4	5	369	2	142
La$_{0.7}$Sr$_{0.3}$MnO$_3$	SG, (973/5 h)	21	358	2.81	5	232	2	47
La$_{0.56}$Pr$_{0.14}$Sr$_{0.3}$MnO$_3$	SG, (973/5 h)	30	343	2.96	5	271	2	47
La$_{0.42}$Pr$_{0.28}$Sr$_{0.3}$MnO$_3$	SG, (973/5 h)	34	329	2.70	5	267	2	47
La$_{0.28}$Pr$_{0.42}$Sr$_{0.3}$MnO$_3$	SG, (973/5 h)	24	311	2.17	5	283	2	47
La$_{0.14}$Pr$_{0.56}$Sr$_{0.3}$MnO$_3$	SG, (973/5 h)	27	290	2.44	5	289	2	47
La$_{0.05}$Pr$_{0.1}$Sr$_{0.35}$MnO$_3$	SGP, (1373/24 h)	—	310	3.58	3	161.11	2	61
La$_{0.05}$Pr$_{0.1}$Sr$_{0.35}$Mn$_{0.95}$Ti$_{0.05}$O$_3$	SGP, (1373/24 h)	—	288	2.78	3	118.85	2	61
La$_{0.6}$Ca$_{0.4}$MnO$_3$	SG, (973/10 h)	45	258	2.3	5	228	2	23
La$_{0.7}$Ca$_{0.3}$MnO$_3$	P, (1273/48 h)	190	254	5.98	5	252	1	119
La$_{0.7}$Ca$_{0.3}$MnO$_3$	SG, (1273/48 h)	265	251	6.88	5	259	1	119
La$_{0.7}$Ca$_{0.3}$MnO$_3$	SSR, (1573/48 h)	11 000	253	7.06	5	263	1	119
La$_{0.7}$Ca$_{0.3}$MnO$_3$	P-SPS, (1073/10 m)	95	243	2.60	5	288	2	119
La$_{0.7}$Ca$_{0.3}$MnO$_3$	SG-SPS, (1073/10 m)	75	235	2.81	5	272	2	119
La$_{0.7}$Ca$_{0.3}$MnO$_3$	R-SPS, (1073/10 m)	40	160	1.65	5	249	2	119
La$_{0.66}$Ca$_{0.33}$MnO$_3$	ST, (1023/6 h)	22.60	258	3.76	5	226.61	2	24
La$_{0.61}$Ca$_{0.33}$Mn$_{1.05}$O$_3$	ST, (1023/6 h)	21.20	272	3.61	5	210.51	2	24
La$_{0.56}$Ca$_{0.33}$Mn$_{1.10}$O$_3$	ST, (1023/6 h)	21.90	262	3.08	5	183.57	2	24
La$_{0.66}$Ca$_{0.28}$Mn$_{1.05}$O$_3$	ST, (1023/6 h)	24.00	266	3.67	5	233.45	2	24
La$_{0.66}$Ca$_{0.23}$Mn$_{1.10}$O$_3$	ST, (1023/6 h)	20.30	278	2.99	5	195.71	2	24
La$_{0.7}$Ca$_{0.3}$MnO$_3$	MM, (—)	15	139	0.89	1.5	—	2	172
La$_{0.7}$Ca$_{0.3}$Mn$_{0.98}$Ni$_{0.02}$O$_3$	MM, (—)	15	134	0.77	1.5	—	2	172
La$_{0.7}$Ca$_{0.3}$Mn$_{0.93}$Ni$_{0.07}$O$_3$	MM, (—)	15	139	0.70	1.5	—	2	172
La$_{0.7}$Ca$_{0.3}$Mn$_{0.90}$Ni$_{0.10}$O$_3$	MM, (—)	15	154	0.95	1.5	—	2	172
La$_{0.7}$Ca$_{0.24}$Sr$_{0.06}$MnO$_3$	SGP, (1473/6 h)	40	292	5.3×10^{-4}	5	∼276	2	220
La$_{0.7}$Ca$_{0.24}$Sr$_{0.06}$MnO$_3$	SGP-SPS, (1473/6 h)	400	292	5.16×10^{-4}	5	—	2	220
La$_{0.7}$Ca$_{0.26}$Sr$_{0.04}$MnO$_3$	MSGP, (1473/3 h)	1440	280	1.9×10^{-4}	5	—	2	220
La$_{0.7}$Ca$_{0.23}$Sr$_{0.07}$MnO$_3$	SSRPR, (1573/24 h)	1680	292	5.5×10^{-4}	5	∼210	2	220
La$_{0.7}$Ca$_{0.23}$Sr$_{0.07}$MnO$_3$	SSRAM, (1573/24 h)	1120	301	4.2×10^{-4}	5	∼160	2	220
La$_{0.7}$Ca$_{0.3}$MnO$_3$	HEBM, (1373/2 h)	568.86	243	7.43	1.8	93.29	1	117
La$_{0.7}$Sr$_{0.05}$Ca$_{0.25}$MnO$_3$	HEBM, (1373/2 h)	586.33	271	6.29	1.8	65.51	2	117
La$_{0.7}$Sr$_{0.10}$Ca$_{0.20}$MnO$_3$	HEBM, (1373/2 h)	599.18	312	4.05	1.8	60.80	2	117
La$_{0.7}$Sr$_{0.15}$Ca$_{0.15}$MnO$_3$	HEBM, (1373/2 h)	608.49	325	3.78	1.8	70.39	2	117
La$_{0.7}$Sr$_{0.20}$Ca$_{0.10}$MnO$_3$	HEBM, (1373/2 h)	416.99	342	3.47	1.8	74.63	2	117
La$_{0.55}$Sr$_{0.45}$MnO$_3$	SSR, (1373/12 h)	480	354	3.088	5	213	2	60
La$_{0.55}$Ca$_{0.05}$Sr$_{0.40}$MnO$_3$	SSR, (1373/12 h)	410	342	2.830	5	196	2	60
La$_{0.55}$Ca$_{0.10}$Sr$_{0.35}$MnO$_3$	SSR, (1373/12 h)	420	336	2.710	5	177	2	60
La$_{0.55}$Ca$_{0.25}$Sr$_{0.20}$MnO$_3$	SSR, (1373/12 h)	430	311	2.550	5	165	2	60
La$_{0.67}$Ca$_{0.23}$Sr$_{0.1}$Mn$_{0.98}$Ni$_{0.02}$O$_3$	SG, (1273/24 h)	860	296	4.92	5	193	2	26
La$_{0.63}$Ca$_{0.20}$Sr$_{0.13}$MnO$_3$	SG, (—)	40	267	0.83	3	48	2	33
La$_{0.63}$Ca$_{0.20}$Sr$_{0.13}$MnO$_3$	SG-SPS, (1073/15 m)	—	272	1.1	3	65	2	33
La$_{0.63}$Ca$_{0.20}$Sr$_{0.13}$MnO$_3$	SG-SPS, (1173/15 m)	—	285	1.8	3	88	2	33
La$_{0.63}$Ca$_{0.18}$Sr$_{0.15}$Mn$_{0.98}$Fe$_{0.02}$O$_3$	SG, (1273/24 h)	410	329	4.889	5	181	2	27
La$_{0.63}$Ca$_{0.13}$Sr$_{0.20}$Mn$_{0.98}$Fe$_{0.02}$O$_3$	SG, (1273/24 h)	680	330	4.712	5	204	2	27
La$_{0.63}$Ca$_{0.03}$Sr$_{0.30}$Mn$_{0.98}$Fe$_{0.02}$O$_3$	SG, (1273/24 h)	790	350	3.355	5	179	2	27
La$_{0.63}$Ca$_{0.29}$Sr$_{0.04}$MnO$_3$	SGP, (1373/1 h)	—	264.43	0.56	0.5	16	2	167
La$_{0.63}$Ca$_{0.29}$Sr$_{0.04}$MnO$_3$	SGP, (1373/1 h)	—	266.87	1.02	1	34.8	2	167
La$_{0.63}$Ca$_{0.29}$Sr$_{0.04}$MnO$_3$	SGP, (1373/1 h)	—	269.29	1.43	2	54.1	2	167
La$_{0.63}$Ca$_{0.29}$Sr$_{0.04}$MnO$_3$	SGP, (1373/1 h)	—	276.31	2.44	3	114.9	2	167
La$_{0.70}$Ca$_{0.20}$Sr$_{0.10}$MnO$_3$	SSR, (1473/24 h)	—	308	1.97	2	—	2	123
La$_{0.7}$Ca$_{0.15}$Sr$_{0.15}$MnO$_3$	SSR, (1473/24 h)	—	338	0.344	1	12.272	2	124
La$_{0.7}$Ca$_{0.15}$Sr$_{0.15}$Mn$_{0.98}$Gd$_{0.02}$O$_3$	SSR, (1473/24 h)	—	211	0.629	1	48.951	2	124
La$_{0.7}$Ca$_{0.15}$Sr$_{0.15}$Mn$_{0.94}$Gd$_{0.06}$O$_3$	SSR, (1473/24 h)	—	203	0.509	1	51.964	2	124
La$_{0.7}$Ca$_{0.15}$Sr$_{0.15}$MnO$_3$	SSR, (1473/24 h)	—	338	0.925	2	37.568	2	124
La$_{0.7}$Ca$_{0.15}$Sr$_{0.15}$Mn$_{0.98}$Gd$_{0.02}$O$_3$	SSR, (1473/24 h)	—	211	1.198	2	108.698	2	124
La$_{0.7}$Ca$_{0.15}$Sr$_{0.15}$Mn$_{0.94}$Gd$_{0.06}$O$_3$	SSR, (1473/24 h)	—	203	1.004	2	111.63	2	124
La$_{0.75}$Eu$_{0.05}$Ca$_{0.1}$Sr$_{0.1}$MnO$_3$	SG, (1173/10 h)	171	264	5.39	2	110.38	2	144
La$_{0.70}$Eu$_{0.10}$Ca$_{0.1}$Sr$_{0.1}$MnO$_3$	SG, (1173/10 h)	98.34	226	4.52	2	119.81	2	144
La$_{0.65}$Eu$_{0.15}$Ca$_{0.1}$Sr$_{0.1}$MnO$_3$	SG, (1173/10 h)	84.34	194	4.35	2	124.38	2	144
La$_{0.75}$Eu$_{0.05}$Ca$_{0.1}$Sr$_{0.1}$MnO$_3$	SG, (1173/10 h)	171	264	5.39	5	282.20	2	144
La$_{0.70}$Eu$_{0.10}$Ca$_{0.1}$Sr$_{0.1}$MnO$_3$	SG, (1173/10 h)	98.34	226	4.52	5	305.20	2	144

14486 | *Phys. Chem. Chem. Phys.*, 2024, **26**, 14476–14504

This journal is © the Owner Societies 2024

Table 2 (continued)

Material	Sample form, heat treatment (T(K)/t)	Grain size (nm)	T_C (K)	$\lvert-\Delta S_M\rvert$ (J kg^{-1} K^{-1})	ΔH (T)	RCP (J kg^{-1})	Transition order	Ref.
$La_{0.65}Eu_{0.15}Ca_{0.1}Sr_{0.1}MnO_3$	SG, (1173/10 h)	84.34	194	4.35	5	323.15	2	144
$La_{0.7}Sr_{0.15}Ca_{0.15}MnO_3$	SG, (1223/10 h)	114.37	341	3.74	5	—	2	115
$La_{0.65}Bi_{0.05}Sr_{0.15}Ca_{0.15}MnO_3$	SG, (1223/10 h)	275.55	321	4.13	5	—	2	115
$La_{0.60}Bi_{0.10}Sr_{0.15}Ca_{0.15}MnO_3$	SG, (1223/10 h)	325.5	291	4.28	5	257	2	115
$La_{0.55}Bi_{0.15}Sr_{0.15}Ca_{0.15}MnO_3$	SG, (1223/10 h)	433.83	251	4.18	5	248	2	115
$La_{0.7}Sr_{0.3}Mn_{0.9}Cu_{0.1}O_3$	SG, (1273/24 h)	27	320	3.07	5	198	2	20
$La_{0.6}Bi_{0.1}Sr_{0.2}Ca_{0.1}Mn_{0.9}Cu_{0.1}O_3$	SG, (1273/24 h)	29	275	3.66	5	162	2	20
$La_{0.6}Bi_{0.1}Sr_{0.15}Ca_{0.15}Mn_{0.9}Cu_{0.1}O_3$	SG, (1273/24 h)	32	235	3.74	5	159	2	20
$La_{0.7}Sr_{0.3}Mn_{0.9}Cu_{0.1}O_3$	SG, (1273/24 h)	27	320	3.07	5	198	2	20
$La_{0.6}Bi_{0.1}Sr_{0.3}Mn_{0.9}Cu_{0.1}O_3$	SG, (1273/24 h)	23	300	3.4	5	161	2	20
$La_{0.6}Bi_{0.1}Sr_{0.25}Ca_{0.05}Mn_{0.9}Cu_{0.1}O_3$	SG, (1273/24 h)	24	290	3.65	5	184	2	20
$La_{0.7}Ba_{0.1}Ca_{0.1}Sr_{0.1}MnO_3$	WM, (1473/6 h)	40	316.17	3.16	5	284.53	2	16
$La_{0.7}Ba_{0.1}Ca_{0.1}Sr_{0.1}MnO_3$	WM, (1473/6 h)	40	316.17	2.6	4	221.16	2	16
$La_{0.7}Ba_{0.1}Ca_{0.1}Sr_{0.1}MnO_3$	WM, (1473/6 h)	40	316.17	2	3	162.66	2	16
$La_{0.7}Ba_{0.1}Ca_{0.1}Sr_{0.1}MnO_3$	WM, (1473/6 h)	40	316.17	1.34	2	102.51	2	16
$La_{0.7}Ba_{0.1}Ca_{0.1}Sr_{0.1}MnO_3$	WM, (1473/6 h)	40	316.17	0.61	1	48.59	2	16
$La_{0.7}Ba_{0.1}Ca_{0.1}Sr_{0.1}MnO_3$	SG, (1473/6 h)	62	337.81	4.89	5	229.29	2	16
$La_{0.7}Ba_{0.1}Ca_{0.1}Sr_{0.1}MnO_3$	SG, (1473/6 h)	62	337.81	4.27	4	173.66	2	16
$La_{0.7}Ba_{0.1}Ca_{0.1}Sr_{0.1}MnO_3$	SG, (1473/6 h)	62	337.81	3.51	3	123.80	2	16
$La_{0.7}Ba_{0.1}Ca_{0.1}Sr_{0.1}MnO_3$	SG, (1473/6 h)	62	337.81	2.58	2	74.923	2	16
$La_{0.7}Ba_{0.1}Ca_{0.1}Sr_{0.1}MnO_3$	SG, (1473/6 h)	62	337.81	1.31	1	32.619	2	16
$La_{0.7}Ba_{0.15}Ca_{0.15}MnO_3$	SSR, (1623/30 h)	91.18	308	4.37	4	140.43	2	77
$La_{0.7}Ba_{0.10}Ca_{0.20}MnO_3$	SSR, (1623/30 h)	89.99	279	5.43	4	184.69	2	77
$La_{0.7}Ba_{0.05}Ca_{025}MnO_3$	SSR, (1623/30 h)	132.45	261	7.01	4	182.37	2	77
$La_{0.7}Ba_{0.15}Ca_{0.15}MnO_3$	SG, (1273/10 h)	16.41	210	1.31	4	144.1	2	77
$La_{0.7}Ba_{0.10}Ca_{0.20}MnO_3$	SG, (1273/10 h)	17.65	185	1.28	4	153.6	2	77
$La_{0.7}Ba_{0.05}Ca_{0.25}MnO_3$	SG, (1273/10 h)	54.6	130	0.27	4	40.5	2	77
$La_{0.6}Ca_{0.2}Ba_{0.2}MnO_3$	SSR, (1473/48 h)	120	300	2.4	2	190	2	40
$La_{0.6}Ca_{0.2}Ba_{0.2}MnO_3$	P-SPS, (973/12 m)	60	245	4.7	2	244	2	40
$La_{0.7}Ca_{0.3}MnO_3$	SG-SPS, (973/10 m)	63	205	2.62	5	267.2	—	118
$La_{0.7}Ca_{0.2}Ba_{0.1}MnO_3$	SG-SPS, (973/10 m)	52	225	2.51	5	268.5	—	118
$La_{0.7}Ca_{0.1}Ba_{0.2}MnO_3$	SG-SPS, (973/10 m)	44	245	2.33	5	270.3	—	118
$La_{0.7}Ca_{0.3}MnO_3$	SSR, (1573/48 h)	11 000	243	7.1	5	263	1	120
$La_{0.7}Ca_{0.2}Ba_{0.1}MnO_3$	SSR, (1573/48 h)	5000	260	4.3	5	258	1	120
$La_{0.7}Ca_{0.1}Ba_{0.2}MnO_3$	SSR, (1573/48 h)	4000	302	3.5	5	207	1	120
$La_{0.7}Ca_{0.3}MnO_3$	P-SPS, (1073/10 m)	95	253	2.6	5	288	2	120
$La_{0.7}Ca_{0.2}Ba_{0.1}MnO_3$	P-SPS, (1073/10 m)	140	280	2.3	5	301	2	120
$La_{0.7}Ca_{0.1}Ba_{0.2}MnO_3$	P-SPS, (1073/10 m)	125	311	1.7	5	306	2	120
$La_{0.8}Ba_{0.05}Sr_{0.15}MnO_3$	SG, (1373/10 h)	38.57	320	4.21	5	254	2	17
$La_{0.75}K_{0.05}Ba_{0.05}Sr_{0.15}MnO_3$	SG, (1373/10 h)	61.75	335	4.99	5	219	2	17
$La_{0.70}K_{0.10}Ba_{0.05}Sr_{0.15}MnO_3$	SG, (1373/10 h)	58.66	345	5.19	5	249	2	17
$La_{0.65}K_{0.15}Ba_{0.05}Sr_{0.15}MnO_3$	SG, (1373/10 h)	58.37	355	4.83	5	301	2	17
$La_{0.50}K_{0.20}Ba_{0.05}Sr_{0.15}MnO_3$	SG, (1373/10 h)	58.86	360	3.90	5	173	2	17
$La_{0.67}Sr_{0.33}MnO_3$	SG, (873/12 h)	48	275	1092	5	133.13	2	221
$La_{0.67}Sr_{0.33}MnO_3$	SG, (1073/12 h)	65	315	1.615	5	138.82	2	221
$La_{0.67}Sr_{0.33}MnO_3$	SG, (1273/12 h)	85	350	1.791	5	229.16	2	221
$La_{0.67}Sr_{0.33}MnO_3$	SG, (1473/12 h)	96	370	2.394	5	248.05	2	221
$La_{0.67}Sr_{0.33}MnO_3$	SG, (1273/24 h)	163.8	368.2	1.5	1	—	2	25
$La_{0.67}Sr_{0.33}CoO_3$	SG, (1273/24 h)	71.8	244.1	0.145	1	—	2	25
$La_{0.67}Sr_{0.33}CrO_3$	SG, (1273/24 h)	205.7	276.1	0.023	1	—	2	25
$La_{0.67}Sr_{0.33}FeO_3$	SG, (1273/24 h)	144.7	369.9	0.002	1	—	2	25
$La_{0.7}Sr_{0.3}MnO_3$	SG, (1073/5 h)	70	370	1.83	2	101	2	137
$La_{0.7}Sr_{0.3}Mn_{0.96}Fe_{0.04}O_3$	SG, (1073/5 h)	48	335	1.26	2	101	2	137
$La_{0.7}Sr_{0.3}Mn_{0.92}Fe_{0.08}O_3$	SG, (1073/5 h)	43	297	1.09	2	108	2	137
$La_{0.7}Sr_{0.3}Mn_{0.88}Fe_{0.12}O_3$	SG, (1073/5 h)	51	258	0.82	2	87	2	137
$La_{0.7}Sr_{0.3}Mn_{0.84}Fe_{0.16}O_3$	SG, (1073/5 h)	61	197	0.60	2	74	2	137
$La_{0.7}Sr_{0.3}Mn_{0.80}Fe_{0.20}O_3$	SG, (1073/5 h)	58	150	0.42	2	46	2	137
$La_{0.7}Sr_{0.3}Mn_{0.76}Fe_{0.24}O_3$	SG, (1073/5 h)	60	116	0.25	2	27	2	137
$La_{0.7}Sr_{0.3}Mn_{0.70}Fe_{0.30}O_3$	SG, (1073/5 h)	67	98	0.13	2	13	2	137
$La_{0.9}Sr_{0.1}MnO_3$	SSR, (1173/96 h)	—	172.8	2.64	5	306	2	222
$La_{0.9}Sr_{0.1}Mn_{0.85}Fe_{0.15}O_3$	SSR, (1173/96 h)	—	168	2.79	5	213	2	222
$La_{0.9}Sr_{0.1}Mn_{0.90}Fe_{0.10}O_3$	SSR, (1173/96 h)	—	155	2.44	5	197	2	222
$La_{0.8}Sr_{0.2}MnO_3$	SG, (1173/10 h)	41.88	332	1.94	2	120.59	2	164
$La_{0.775}Gd_{0.050}Sr_{0.2}MnO_3$	SG, (1173/10 h)	41.28	315	2.13	2	108.84	2	164
$La_{0.725}Gd_{0.075}Sr_{0.2}MnO_3$	SG, (1173/10 h)	53.30	295	2.03	2	116.40	2	164
$La_{0.700}Gd_{0.010}Sr_{0.2}MnO_3$	SG, (1173/10 h)	58.96	292	1.71	2	102.91	2	164
$La_{0.8}Sr_{0.2}MnO_3$	SG, (1173/10 h)	41.88	332	4.06	5	—	2	164
$La_{0.7}Sr_{0.3}Si_{0.05}Mn_{0.95}O_3$	SSR, (1523/6 h)	—	365.2	0.83	1.5	71.3	2	179

This journal is © the Owner Societies 2024

Phys. Chem. Chem. Phys., 2024, 26, 14476–14504 | 14487

Table 2 (continued)

Material	Sample form, heat treatment (T(K)/t)	Grain size (nm)	T_C (K)	$\lvert-\Delta S_M\rvert$ (J kg^{-1} K^{-1})	ΔH (T)	RCP (J kg^{-1})	Transition order	Ref.
La$_{0.7}$Sr$_{0.3}$Ti$_{0.05}$Mn$_{0.95}$O$_3$	SSR, (1523/6 h)	—	314.7	1.08	1.5	53.4	2	179
La$_{0.7}$Sr$_{0.3}$MnO$_3$	MM, (1373/2 h)	—	376	2.7	1.8	156	2	116
La$_{0.65}$Gd$_{0.05}$Sr$_{0.3}$MnO$_3$	MM, (1373/2 h)	—	356	2.6	1.8	155	2	116
La$_{0.60}$Gd$_{0.10}$Sr$_{0.3}$MnO$_3$	MM, (1373/2 h)	—	335	2.4	1.8	166	2	116
La$_{0.55}$Gd$_{0.15}$Sr$_{0.3}$MnO$_3$	MM, (1373/2 h)	—	311	3.7	1.8	183	2	116
La$_{0.50}$Gd$_{0.20}$Sr$_{0.3}$MnO$_3$	MM, (1373/2 h)	—	238	3.2	1.8	131	2	116
La$_{0.775}$Gd$_{0.050}$Sr$_{0.2}$MnO$_3$	SG, (1173/10 h)	41.28	315	4.26	5	—	2	164
La$_{0.725}$Gd$_{0.075}$Sr$_{0.2}$MnO$_3$	SG, (1173/10 h)	53.30	295	4.23	5	304.12	2	164
La$_{0.700}$Gd$_{0.010}$Sr$_{0.2}$MnO$_3$	SG, (1173/10 h)	58.96	292	3.59	5	281.80	2	164
La$_{0.4}$Gd$_{0.2}$Sr$_{0.4}$MnO$_3$	SG, (1173/10 h)	~25	331	0.067	6	12.196	2	78
La$_{0.4}$Gd$_{0.2}$Sr$_{0.4}$MnO$_3$	SG, (1173/10 h)	~25	318	2.486	6	404.085	2	78
La$_{0.7}$Sr$_{0.3}$MnO$_3$	SG, (1173/24 h)	20.09	319	1.63	5	178	2	122
La$_{0.69}$Dy$_{0.01}$Sr$_{0.3}$MnO$_3$	SG, (1173/24 h)	23.88	315	1.21	5	114	2	122
La$_{0.67}$Dy$_{0.03}$Sr$_{0.3}$MnO$_3$	SG, (1173/24 h)	23.88	264	1.05	5	204	2	122
La$_{0.7}$Sr$_{0.3}$MnO$_3$	SSR, (1753/12 h)	—	357	3.43	5	170	2	126
La$_{0.6}$Eu$_{0.1}$Sr$_{0.3}$MnO$_3$	SSR, (1753/12 h)	—	342	4.35	5	201	2	126
La$_{0.5}$Eu$_{0.2}$Sr$_{0.3}$MnO$_3$	SSR, (1753/12 h)	—	292	4.46	5	203	2	126
La$_{0.4}$Eu$_{0.3}$Sr$_{0.3}$MnO$_3$	SSR, (1753/12 h)	—	228	4.55	5	203	2	126
La$_{0.75}$Eu$_{0.05}$Sr$_{0.2}$MnO$_3$	SG, (1073/20 h)	56	298	0.70	2	90.11	2	223
La$_{0.75}$Eu$_{0.05}$Sr$_{0.2}$MnO$_3$	SG, (1273/20 h)	97	305	1.33	2	85.14	2	223
La$_{0.75}$Eu$_{0.05}$Sr$_{0.2}$MnO$_3$	SG, (1473/20 h)	484	305	1.76	2	78.24	2	223
La$_{0.67}$Ca$_{0.33}$MnO$_3$	SG, (1273/24 h)	257.76	270.5	1.8	1	—	—	64
La$_{0.67}$Sr$_{0.33}$MnO$_3$	SG, (1273/24 h)	223.19	301.2	1.0	1	—	—	64
La$_{0.8}$□$_{0.2}$MnO$_{2.8}$	SG, (1173/24 h)	1059	232	2.39	2	126.83	2	224
La$_{0.8}$□$_{0.2}$MnO$_{2.9}$	SG, (1173/24 h)	143	302	3.04	2	89.95	2	224
La$_{0.8}$□$_{0.2}$MnO$_3$	SG, (1173/24 h)	141	300	2.88	2	87.53	2	224
La$_{0.5}$□$_{0.1}$Ca$_{0.4}$MnO$_3$	SSR, (1623/12 h)	—	251	0.78	1	24.33	2	39
La$_{0.5}$□$_{0.1}$Ca$_{0.4}$MnO$_3$	SSR, (1623/12 h)	—	251	2.18	2	71.64	2	39
La$_{0.5}$□$_{0.1}$Ca$_{0.4}$MnO$_3$	SSR, (1623/12 h)	—	251	3.24	3	124.42	2	39
La$_{0.5}$□$_{0.1}$Ca$_{0.4}$MnO$_3$	SSR, (1623/12 h)	—	251	4.08	4	180.69	2	39
La$_{0.5}$□$_{0.1}$Ca$_{0.4}$MnO$_3$	SSR, (1623/12 h)	—	251	4.80	5	232.20	2	39
La$_{0.8}$Ca$_{0.2}$MnO$_3$	SSR, (1473/24 h)	—	187	~4.110	5	~269	—	114
La$_{0.8}$Ca$_{0.15}$□$_{0.05}$MnO$_3$	SSR, (1473/24 h)	—	183	~4.050	5	~267	—	114
La$_{0.8}$Ca$_{0.10}$□$_{0.10}$MnO$_3$	SSR, (1473/24 h)	—	183	~4.014	5	~284	—	114
La$_{0.8}$Ca$_{0.05}$□$_{0.15}$MnO$_3$	SSR, (1473/24 h)	—	182	~3.681	5	~293	—	114
La$_{0.8}$□$_{0.2}$MnO$_3$	SSR, (1473/24 h)	—	182	~3.497	5	~260	—	114
La$_{0.8}$Ca$_{0.2}$MnO$_3$	SSR, (1473/24 h)	—	241	~7.70	5	~255	—	121
La$_{0.8}$Ca$_{0.10}$□$_{0.10}$MnO$_3$	SSR, (1473/24 h)	—	264	~7.25	5	~275	—	121
La$_{0.8}$□$_{0.20}$MnO$_3$	SSR, (1473/24 h)	—	259	~7.60	5	~230	—	121
La$_{0.8}$Ca$_{0.2}$MnO$_3$	SSR, (1473/24 h)	—	241	~5.50	2	~95	—	121
La$_{0.8}$Ca$_{0.10}$□$_{0.10}$MnO$_3$	SSR, (1473/24 h)	—	264	~4.30	2	~105	—	121
La$_{0.8}$□$_{0.20}$MnO$_3$	SSR, (1473/24 h)	—	259	~5.00	2	~92	—	121
La$_{0.8}$Ca$_{0.2}$MnO$_3$	SSR, (1473/24 h)	—	241	~2.00	0.5	~25	—	121
La$_{0.8}$Ca$_{0.10}$□$_{0.10}$MnO$_3$	SSR, (1473/24 h)	—	264	~1.10	0.5	~40	—	121
La$_{0.8}$□$_{0.20}$MnO$_3$	SSR, (1473/24 h)	—	259	~1.15	0.5	~26	—	121
La$_{0.55}$□$_{0.1}$Ca$_{0.35}$MnO$_3$	SG, (1173/24 h)	—	274.7	1.97	2	71.88	2	43
La$_{0.65}$Ba$_{0.35}$MnO$_3$	SSR, (1473/24 h)	—	325	1.83	5	186	2	168
La$_{0.65}$Ba$_{0.30}$□$_{0.05}$MnO$_3$	SSR, (1473/24 h)	—	345	3.75	5	180	2	168
La$_{0.65}$Ba$_{0.25}$□$_{0.10}$MnO$_3$	SSR, (1473/24 h)	—	332	3.91	5	213	2	168
La$_{0.65}$Ba$_{0.15}$□$_{0.20}$MnO$_3$	SSR, (1473/24 h)	—	288	4.12	5	231	2	168
La$_{0.67}$Sr$_{0.33}$MnO$_3$	SSR, (1623/12 h)	—	365	1,62	1	—	2	146
La$_{0.58}$Sr$_{0.33}$□$_{0.09}$MnO$_{3-\delta}$	SSR, (1623/12 h)	—	367	1.41	1	—	2	146
La$_{0.63}$Sr$_{0.24}$□$_{0.09}$MnO$_{3-\delta}$	SSR, (1623/24 h)	—	355	1.78	1	—	2	146
La$_{0.67}$Sr$_{0.33}$MnO$_3$	SSR, (1623/12 h)	—	365	4.78	5	120	2	146
La$_{0.58}$Sr$_{0.33}$□$_{0.09}$MnO$_{3-\delta}$	SSR, (1623/12 h)	—	367	4.12	5	103	2	146
La$_{0.67}$Sr$_{0.24}$□$_{0.09}$MnO$_{3-\delta}$	SSR, (1623/12 h)	—	355	5.08	5	142	2	146
La$_{0.67}$Sr$_{0.15}$□$_{0.18}$MnO$_{3-\delta}$	SSR, (1623/12 h)	—	310	4.61	5	—	2	135
La$_{0.67}$Sr$_{0.06}$□$_{0.27}$MnO$_{3-\delta}$	SSR, (1623/12 h)	—	276	4.11	5	—	2	135
Composite								
0.75La$_{0.67}$Ca$_{0.33}$MnO$_3$/ 0.25La$_{0.67}$Sr$_{0.33}$MnO$_3$	SG, (1273/24 h)	342.09	370	>1.0	1	—	—	64
0.50La$_{0.67}$Ca$_{0.33}$MnO$_3$/ 0.50La$_{0.67}$Sr$_{0.33}$MnO$_3$	SG, (1273/24 h)	326.7	335	1.1	1	—	—	64
0.25La$_{0.67}$Ca$_{0.33}$MnO$_3$/ 0.75La$_{0.67}$Sr$_{0.33}$MnO$_3$	SG, (1273/24 h)	237.88	340	0.8	1	—	—	64
0.75La$_{0.62}$Nd$_{0.05}$Ba$_{0.33}$MnO$_3$/ 0.25Ni$_{0.5}$Zn$_{0.5}$Fe$_2$O$_4$	CP, (1273/10 h)	—	290	3.03	5	242	2	44

14488 | *Phys. Chem. Chem. Phys.*, 2024, **26**, 14476–14504

This journal is © the Owner Societies 2024

Table 2 (continued)

Material	Sample form, heat treatment (T(K)/t)	Grain size (nm)	T_C (K)	$|-\Delta S_M|$ (J kg^{-1} K^{-1})	ΔH (T)	RCP (J kg^{-1})	Transition order	Ref.
0.75La$_{0.62}$Nd$_{0.05}$Ba$_{0.33}$MnO$_3$/ 0.25Ni$_{0.4}$Zn$_{0.6}$Fe$_2$O$_4$	CP, (1273/10 h)	—	281	2.40	5	252.72	2	44
0.75La$_{0.62}$Nd$_{0.05}$Ba$_{0.33}$MnO$_3$/ 0.25Ni$_{0.4}$Zn$_{0.7}$Fe$_2$O$_4$	CP, (1273/10 h)	—	255	2.30	5	300.60	2	44
LaFe$_{11.6}$Si$_{1.4}$ (<100 μm)/ 5 wt% Pr$_2$Co$_7$	Arc-M-SPS, (for SPS 1273/5 m forwad to (1323/24 h))	—	270	2.29	5	115	2	31
LaFe$_{11.6}$Si$_{1.4}$ (<100 μm)/ 10 wt% Pr$_2$Co$_7$	Arc-M-SPS, (for SPS 1273/5 m forwad to (1323/24 h))	—	297	2.22	5	133	2	31
LaFe$_{11.6}$Si$_{1.4}$ (100–200 μm)/ 10 wt% Pr$_2$Co$_7$	Arc-M-SPS, (for SPS 1273/5 m forwad to (1323/24 h))	—	280	3.64	5	149	2	31
LaFe$_{11.6}$Si$_{1.4}$ (200–300 μm)/ 10 wt% Pr$_2$Co$_7$	Arc-M-SPS, (for SPS 1273/5 m forwad to (1323/24 h))	—	275	1.92	5	138	2	31

Note: SG (sol–gel), SSR (solid-state reaction), wet-mixing (WM), PW (pore wetting), ST (solvothermal), MM (mechanical milling), SGP (sol–gel pechini), MSGP (microwave sol–gel Pechini), SSRPR (solid-state reaction planetary Mill), SSRAM (solid-state reaction attrition mill), Arc-M (arc melting), MS-R (melt spinning-ribbons), polyol-spark plasma sintering (P-SPS), sol–gel-spark plasma sintering (SG-SPS), polyol (P), high energy ball milling (HEBM), high pressure resistive furnace (HPRF), microwave assisted solid state (MW), solid-vapor reaction (SVR), CP (coprecipitation process).

in both the paramagnetic and ferromagnetic phases. This condition arises from the covalent bonding of Si(Ge)–Si(Ge) between layers. The transition occurring in this range was SOMT without a change in the crystal structure. In the concentration range $0.24 \leq x \leq 0.5$, a FOMT is observed along with a change in the orthorhombic crystal structure (ferromagnetic state) of Gd$_5$Si$_4$ below T_C to the monoclinic structure of Gd$_5$Si$_2$Ge$_2$ (paramagnetic state) above T_C. This is caused by the disruption of half of the Si(Ge)–Si(Ge) bonding between layers. Finally, in the range $0 \leq x \leq 0.24$, FOMT and a change in the crystal structure from orthorhombic Gd$_5$Ge$_4$ above T_C to orthorhombic Gd$_5$Si$_4$ below T_C were observed, accompanied by the absence of Si(Ge)–Si(Ge) bonding between layers.[96,97]

Based on the report by Pecharsky and Gschneider a Gd$_5$(Si$_2$Ge$_2$) material indicates $-\Delta S_M$ = 18.4 J kg^{-1} K^{-1} and RCP = 535 J kg^{-1} with T_C = 276 K under a magnetic field of 5 T, suggesting the occurrence of a FOMT. Additionally, researchers have explored doping at Gd sites or (Si$_{1-x}$Ge$_x$)$_4$ and have applied hydrostatic pressure treatments to achieve excellent MCE properties with T_C around room temperature.[1,98–100] Despite the high MCE performance and potential for application in magnetic refrigerators, there are still factors to consider, such as hysteresis losses due to FOMT properties, a narrow working temperature range, difficulty in fabricating methods, limited and expensive materials.

3.2.4   La(Fe$_{13-x}$Si$_x$) alloys. La(Fe$_{13-x}$Si$_x$) alloys are one the most promising for magnetic refrigeration applications at room temperature. In the concentration $x \leq 2.5$, the crystal structure of the LaFe$_{13-x}$Si$_x$ alloys is NaZn$_{13}$ type cubic with the $Fm\bar{3}c$ space group, as illustrated in Fig. 3(C). The addition of Si to LaFe$_{13}$ shows a negative lattice expansion at T_C and a transition known as the itinerant electron metamagnetic (IEM) transition above T_C.[101] The IEM transition occurs due to changes in the density of states at the Fermi level when a magnetic field is applied, which occurs with a slight increase in Si concentration.[1] This led to a sharp decrease in the magnetization

change, enhancing the MCE properties of the alloy, accompanied by FOMT. Hu et al. reported an investigation of La(Fe$_{11.4}$Si$_{1.6}$), which showed sharper magnetization change and larger $-\Delta S_M$ than La(Fe$_{10.4}$Si$_{2.6}$). They calculated $-\Delta S_M$ of 19.4 J kg^{-1} K^{-1} under a magnetic field of 5 T.[102] Therefore, this research shows the importance of negative lattice expansion as a key parameter influencing the MCE properties of La(Fe$_{13-x}$Si$_x$) alloys.

The La(Fe$_{13-x}$Si$_x$) alloys are not limited to investigate in the IEM transition. Other developments have been carried out, such as modifying synthesis methods, heat treatments, and compound compositions, to achieve ideal MCE properties. Zhang et al. reported La$_{1.2}$Fe$_{11.2}$Si$_{1.4}$B$_{0.75}$ which is produced using different synthesis methods both Arc-melting (solid) and melt-spinning at 10 m s^{-1} and 50 m s^{-1}. All three samples indicated the presence of the IEM transition, marked by a very sharp magnetization change. This led to presenting FOMT state and high $-\Delta S_M$ values of 6.1, 20.2, and 13.5 J kg^{-1} K^{-1} under a magnetic field of 2 T. Additionally, the T_C value increased with the addition of B concentration (188–191 K), associated with the presence of Fe–Fe exchange interactions with a broadening of the Fe–Fe distance and cell volume.[58] Another study compared the heating behavior of La(Fe$_{13-x}$Si$_x$) alloy-based materials using hot pressing sintering (HPS) and spark plasma sintering (SPS).[30] As observed from the porosity, density, and compressive strength analysis, the SPS method provided better mechanical properties than the HPS method. The value of $-\Delta S_M$ from the SPS and HPS methods reached 12.8 and 12.1 J kg^{-1} K^{-1}, respectively. Thus, it was concluded that the use of the SPS method presents high MCE properties along with good mechanical properties, making it potentially suitable for application as a magnetic refrigerator.[30] More detailed information on La(Fe$_{13-x}$Si$_x$) alloys MCE properties from previous studies is tabulated in Table 2.

3.2.5   MnAs alloys. MnAs alloys are promising candidates for magnetic refrigeration applications, because of their
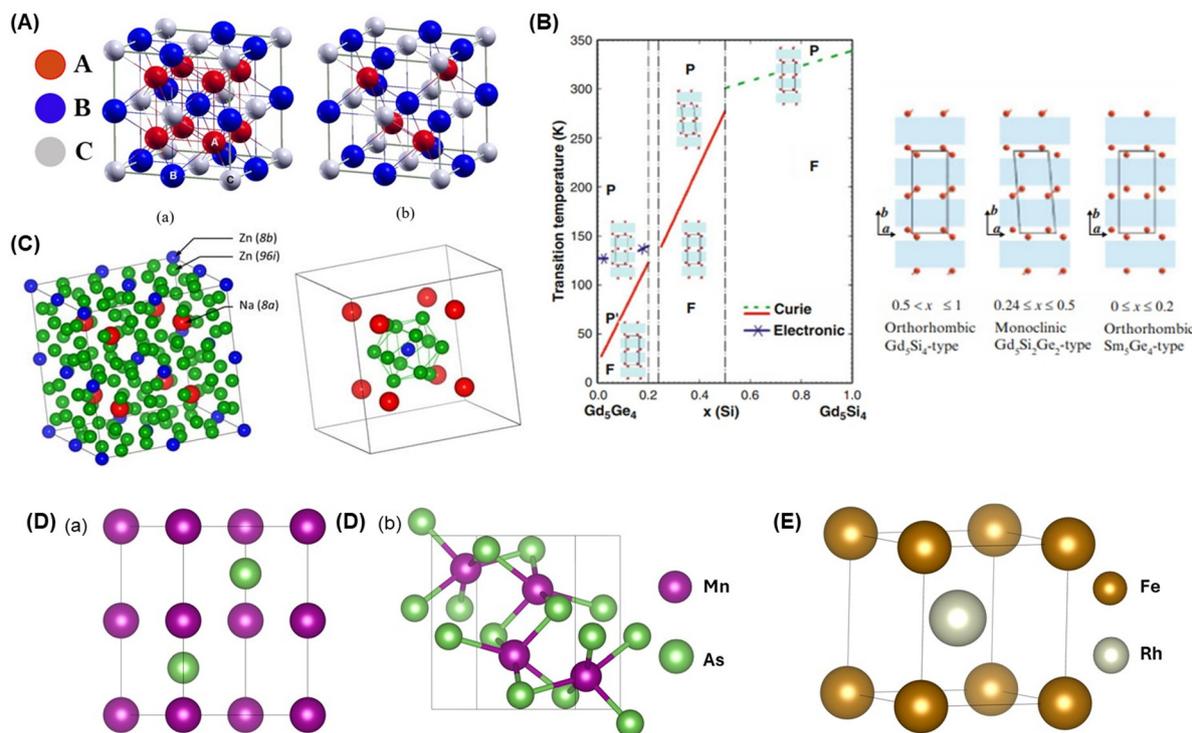
This journal is © the Owner Societies 2024

Phys. Chem. Chem. Phys., 2024, **26**, 14476–14504 | **14489**

Fig. 3 (A) Illustration of crystal structure for (a) full Heusler and (b) half Heusler reprinted from ref. 87 with open acess from MDPI,[87] (B) phase diagram of magnetic and crystal structure of $Gd_5(Si_xGe_{1-x})_4$ reprinted from ref. 96 with permission, copyright 2001, Wiley,[96] (C) crystal structure of $NaZn_{13}$-type in $La(Fe_xSi_{1-x})_{13}$ reprinted from ref. 101 with open access from MDPI,[101] (D) crystal structure of MnAs (a) NiAs-hexagonal type and (b) MnP-orthorhombic type obtained by MaterialProjects,[108] (E) crystal structure of FeRh obtained by crystallography open database,[192] where (D) and (E) are illustrated by VESTA.[193]

significantly high MCE properties. This is attributed to the magneto-structural transition of MnAs from the hexagonal NiAs structure to the orthorhombic MnP structure as it approaches T_C = 313 K.[103,104] Fig. 3(D) illustrates the hexagonal NiAs structure with space group $P6_3/mmc$ (a) below T_C and the orthorhombic MnP structure with space group $Pnma$ (b) above T_C.[105–108] The MnAs alloy is known for its high $-\Delta S_M$ value, reaching 47 J kg^{-1} K^{-1} under a magnetic field of 5 T at T_C = 318 K.[109] Additionally, Wada *et al.* experimented by doping MnAs with Sb, and one of the results, $Mn(As_{0.9}Sb_{0.1})$, is reported $-\Delta S_M$ of 32 J kg^{-1} K^{-1} and T_C of 283 K under a magnetic field of 5 T. Furthermore, this sample exhibited the loss of hysteresis behavior at high temperatures.[110] Sathyanarayana and Mani investigated the MCE properties of $Mn(As_{1-x}Sb_x)$ with x = 0.05–0.30. The results revealed a range of $-\Delta S_M$ values ranging from 20.30 to 23.00 J kg^{-1} K^{-1} and RCP values from 220 to 260 J kg^{-1} under a magnetic field of 5 T, accompanied by the FOMT state. All samples exhibited a ferromagnetic to paramagnetic phase transition with a decrease in T_C from 300.5 to 242 K as the concentration x increased.[35]

The high MCE properties of MnAs are also manifested under hydrostatic pressure. The presence of hydrostatic pressure effects on MnAs leads to the conclusion that there is a decrease in T_C with an increase in pressure and an exponential increase in MCE properties proportional to the pressure increment.[111]

The anticipated increase $-\Delta S_M$ value was estimated to reach 267 J kg^{-1} K^{-1} under a pressure of 2.23 kbar in a 5 T magnetic field. However, this effect diminishes and becomes detrimental when pressed beyond 2.64 kbar.[105] However, behind this promising potential, there are critical issues such as the challenging process of obtaining arsenic (As), which is environmentally toxic and limits its practical applications.[112]

3.2.6 Fe-Based alloys. Iron-based alloys have been extensively investigated due to their high $-\Delta S_M$ values and comparable with other materials. These materials typically exhibit FOMT behavior and magneto-structural transformations which are associated with good MCE properties and high $-\Delta S_M$ values.[34] Various types of materials have been developed from Fe-based alloys, such as Fe17R2 (R = rare earth element), Fe–Ni–M (M = B, Mn, Cr, Mo), Fe–M (M = Rh, Ni, Zr), $Fe_x(M_{1-x})_3Al$ (M = Cr and Mn), Fe–B–Cr–R (R = La, Ce, Gd, Nd), Fe–Zr–B–M (M = Mn, Cr, Ni, Al, Ti, Mo, Co, Er, Sm), Fe–B–X (X = Mn, Nb, Cr, Cu), and Fe–Zr–M (M = Mn, Dy).[1,34,85]

Two of the Fe-based alloys mentioned above are particularly interesting because of differences in their MCE properties such as FeNi and FeRh. Research on FeNi alloys has focused on reducing the T_C values, which are still above room temperature. The addition of Mn to FeNi alloys resulted in a decrease in T_C to 338 and 317 K for $(Fe_{70}Ni_{30})_{95}Mn_5$ and $(Fe_{70}Ni_{30})_{92}Mn_8$, respectively.[85] On the other hand, FeRh alloys, with a cubic crystal structure as shown in Fig. 3(E), have been extensively

studied due to their spectacular giant MCE properties, such as $Fe_{50}Rh_{50}$ and $Fe_{49}Rh_{51}$.[22] $Fe_{50}Rh_{50}$ has a T_C of 400 K, above room temperature, and requires an applied magnetic field of up to 40 T to obtain T_C at around room temperature. Meanwhile, $Fe_{49}Rh_{51}$ had a T_C of 315.6 K. It is noteworthy that FeRh alloys are highly sensitive to thermal treatment and composition.[34] Chirkova et al. investigated $Fe_{49}Rh_{51}$ with slight Ni doping, revealing a significant decrease in T_C to 266 K and obtaining a $-\Delta S_M$ value of 10.3 J kg^{-1} K^{-1} under a magnetic field of 2 T. The emergence of high $-\Delta S_M$ values is associated with FOMT behavior.[34] The FOMT behavior shows hysteresis losses due to thermal and magnetic hysteresis. Therefore, although these materials exhibit excellent MCE values, other factors must be considered before their application in magnetic refrigerators.

3.3 Ceramic materials

3.3.1 Perovskite manganite materials. Perovskite manganites (PM) are ceramic materials with the general formula $R_{1-x}A_xMnO_3$, where R represents rare earth metals, trivalent elements such as La, Pr, Nd, Sm, Eu, Gd, Ho, Tb, Y and A represents elements such as monovalent elements (Li, Na, K, Ag, etc.)[4,15] and divalent elements (Mg, Ca, Sr, Ba, etc.)[41,44,113] which have been extensively combined. The mixed element combinations of PM will create a mixed valence at site A or B. For example, if monovalent and divalent elements are substituted in PM, it will provide a new chemistry stability state as $R_{1-x}^{3+}A_x^{1+}Mn_{1-2x}^{3+}Mn_{2x}^{4+}O^{2-}$ and $R_{1-x}^{3+}A_x^{2+}Mn_{1-x}^{3+}Mn_x^{4+}O^{2-}$ respectively.[15,114] The existence of Mn^{3+} and Mn^{4+} ions in PM can be attracted by exchange interactions, which can influence the magnetic properties of PM. This fact has led researchers to investigate it as an alternative material for MRT. PM has several advantages, including cost-effectiveness, shorter production processes, relative ease of production, chemical stability, good structure, environmental friendliness, resistance to corrosive environments, SOMT behavior, excellent MCE properties, and easily adjustable T_C within the room-temperature range.[40,42,43,114-124]

The basic crystal structure of perovskite ABO_3 is cubic, where cation A occupies the A sites with twelve coordination sites (AO_{12}), and a small portion of cations occupy the B sites with six octahedral coordination (BO_6).[19] However, PM are substituted with specific atoms and experience structural distortions due to changes in the cation size and the Jahn–Teller effect. In a cubic crystal, Jahn–Teller distortion is observed with a reduction in the symmetry and the splitting of e_g levels. This event is influenced by the doping and energetic positions, which strongly affect the hybridization between the Mn^{3+} and O states in the 2p orbital. According to previous studies, the crystal field is determined by ligand states based on the 3d shell structure of ions: three electrons in the low t_{2g} state (t_{2g}^3) and one electron in the high e_g state (e_g^1) for Mn^{3+} ions and a configuration of (t_{2g}^3) for Mn^{4+} ions.[45,52] As a result, the cubic structure transforms into a rhombohedral or orthorhombic structure, as illustrated in Fig. 4(A).

The MCE properties of PM materials have been studied by several researchers. Banik et al. reported that $Pr_{0.8}Sr_{0.2}MnO_3$ exhibits a decrease in magnetization around T_C = 150 K with $-\Delta S_M$ = 3.54 J kg^{-1} K^{-1} and RCP = 289 J kg^{-1} under a magnetic field of 5 T.[125] Meanwhile, Khlifi et al. investigated $La_{0.8}Ca_{0.2-x}\square_xMnO_3$ ($0 \le x \le 0.2$) with annealing treatment at 1073 K, showing a transition from ferromagnetic to paramagnetic phase around T_C, with values of 269, 273, and 276 K, and a decrease in magnetization due to Ca^{2+} ion substitution. The presence of Ca^{2+} ions can convert Mn^{3+} ions to Mn^{4+}, which is linked to double-exchange and super-exchange interactions in the system. Both, the $-\Delta S_M$ values and RCP values for the samples appear in the ranges of 7.25–7.70 J kg^{-1} K^{-1} and 230–275 J kg^{-1}, respectively in under a magnetic field of 5 T, respectively.[121] Furthermore, Vadnala et al. studied $La_{0.7-x}Eu_xSr_{0.3}MnO_3$ compounds with x = 0.0, 0.1, 0.2, 0.3 to adjust the T_C value around room temperature, accompanied by an enhancement in the MCE properties. The T_C values for all the samples were 357, 342, 292, and 228 K, respectively. The decrease in T_C is due to the substitution of Eu^{2+} ions, which have a smaller ionic radius. The $-\Delta S_M$ values increased from 3.43 to 4.55 J kg^{-1} K^{-1}, accompanied by an increase in the RCP values from 170 to 203 J kg^{-1}. The analysis of the magnetic phase transition in $La_{0.7-x}Eu_xSr_{0.3}MnO_3$ compounds exhibits a SOMT behavior, which is associated with the absence of hysteresis losses due to thermal and magnetic hysteresis.[126] A summary of these examples is presented in Table 2.

3.3.2 Double perovskite materials. Double perovskites (DP) based on rare-earth and transition metals have been extensively studied due to their fascinating physical properties, such as MCE properties under cryogenic conditions. Additionally, this material has been well-researched for its easy synthesis, chemical stability, and high physical stability. The structure of DP materials is essentially similar to that of perovskite structure, but in a double version. Therefore, the general formula for DP is $(ABO_3)_2$, which can have crystal structures as depicted in Fig. 4(B) when connected with rare-earth and transition metals, forming $R_2MM'O_6$ (R represents a rare-earth metal, M and M' are transition metals).[19] Several examples of MCE materials based on DP structures ($R_2MM'O_6$) are listed in Table 2.[19,127-129] An example is R_2NiMnO_6, which has a monoclinic crystal structure and is known as a B-sites rock-salt type ordered structure where magnetic ions Ni^{2+} and Mn^{4+} alternate along the c-axis. Furthermore, the SE interaction between Ni^{2+}–O–Mn^{4+} associated with the distribution of Mn^{4+} and Ni^{2+} ions gives rise a high-temperature ferromagnetic ordering. If the rare-earth metal elements (R) of $R_2MM'O_6$ changed from La to Lu, it would decrease in T_C, ranging from 40 to 275 K, which is attributed to decreased ionic radius. Meanwhile, the $-\Delta S_M$ value is 35.5 under magnetic field 7 T, and 4.9, 2.3, 5.2, 6.4 under magnetic field 5 T for R = Gd, Dy, Eu, Pr, Nd, Tb, and Ho.[19]

3.3.3 Spinel ferrite materials. Spinel ferrites have the general formula AFe_2O_4, where A is a transition metal from the 3d group (Mn, Fe, Co, Ni, Cu, Zn, etc.).[5] The AFe_2O_4 type has a cubic spinel crystal structure with the $Fd\bar{3}m$ space group, as
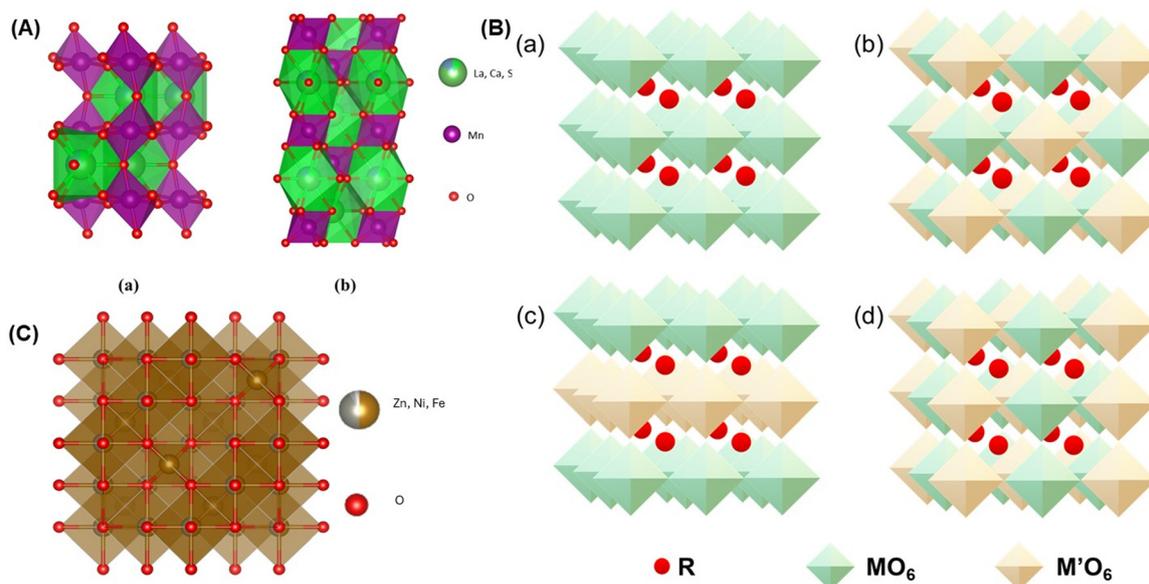
This journal is © the Owner Societies 2024

Phys. Chem. Chem. Phys., 2024, **26**, 14476–14504 | **14491**

Fig. 4 Illustration of crystal structure (A) perovskite manganites (a) orthorhombic-$La_{0.6}Ca_{0.3}Sr_{0.1}MnO_3$ and (b) rhombohedral-$La_{0.6}Ca_{0.2}Sr_{0.2}MnO_3$ obtained by crystallography open database,[194] (B) crystal structure of double perovskite-$R_2MM'O_6$ for (a) similar M and M', (b) rock-salt, (c) layered and (d) columnar order redrawn from ref. 19, (C) crystal structure of spinel ferrite cubic-$Zn_{0.9}Ni_{0.1}Fe_2O_4$ obtained by crystallography open database,[130] where (A) and (C) are illustrated by VESTA.[193]

depicted in Fig. 4(C).[130] The potential applications of spinel ferrites are broad, such as high-density information storage, electromagnetic wave absorption, biomedical applications, and MRT. However, based on the literature review, there are not many reports on the MCE properties of spinel ferrite. One reason why this material has not been extensively investigated for MCE properties is its relatively small $-\Delta S_M$ values, even when applied to high magnetic fields. Additionally, the highly sensitive T_C values pose a consideration, as MCE applications, especially for magnetic refrigeration, require a working temperature range around room temperature.

Oumezzine *et al.* reported on $Zn_{0.6-x}Ni_xCu_{0.4}Fe_2O_4$ ($0 \leq x \leq 0.6$) compounds which were synthesized using the Pechini sol–gel method. They observed a transition from ferromagnetic to paramagnetic phases around T_C values of 305, 565, 705, and > 750 K for x from 0 to 0.6. The significant increase in T_C was associated with the enhanced interactions between A and B in the AB_2O_4 structure. Analysis of the transition type using Arrot plots confirmed the occurrence of SOMT behavior. Furthermore, they calculated $-\Delta S_M$ values of 1.16, 1.41, 1.61 J kg^{-1} K^{-1}, and RCP values of 289, 141, 233 J kg^{-1} for $x = 0.0, 0.2, 0.4$ under a magnetic field of 5 T.[62] Jiyu Hu *et al.* also conducted research on spinel ferrite materials with the chemical formula $CoGa_{1.2}Fe_{0.8}O_4$, which exhibited $T_C = 210$ K and $-\Delta S_M = 1.5$ J kg^{-1} K^{-1} under a magnetic field of 5 T.[36] A summary of the MCE performance from various previous studies is provided in Table 2.

3.4 Composite materials

In the case of composite material research, there are studies on their magnetic properties including the MCE. Zhong *et al.*

reported a composite material $LaFe_{11.6}Si_{1.4}/Pr_2Co_7$, which showed variations in particle size and Pr_2Co_7 content. The $-\Delta S_M$ values for the different samples ranged from 1.92 to 3.64 J kg^{-1} K^{-1}, with RCP values in the range of 84 to 149 J kg^{-1} under a magnetic field of 2 T. Meanwhile, the T_C values of the samples increased from 230 to 297 K with variations in particle size.[31] Additionally, Ezaami *et al.* also reported $(1 - x)La_{0.7}Ca_{0.2}Sr_{0.1}MnO_3/xLa_{0.7}Ca_{0.15}MnO_3$ based on the rule of mixture estimation. In the investigation of the material $(1 - x)La_{0.7}Ca_{0.2}Sr_{0.1}MnO_3/xLa_{0.7}Ca_{0.15}MnO_3$, the optimum MCE properties were found at $x = 0.45$, and more details can be found in their report.[42] In addition, Tillaoui *et al.* reported the magnetocaloric effect properties in $(0.75)La_{0.62}Nd_{0.05}$-$Ba_{0.33}MnO_3/(0.25)Ni_{1-x}Zn_xFe_2O_4$ composites ($x = 0.5, 0.6, 0.7$) where it revealed T_C around room temperature ~ 290 K and provided $-\Delta S_M$ with ranges of 3.03, 2.40, 2.30 J kg^{-1} K^{-1} for $x = 0.5, 0.6, 0.7$ respectively. They also reported the value of the RCP which had a good value with ranges of 242, 252.72, 300.60 for $x = x = 0.5, 0.6, 0.7$.[44]

4. Phenomena and parameters influencing the behavior of MCE in perovskite manganites

As mentioned, a lot of PM exhibit SOMT behavior. Materials with SOMT behavior show reversible magnetic cooling cycles due to their small magnetic and thermal hysteresis.[1] Despite the high values of $-\Delta S_M$ in Table 1, but the $-\Delta S_M$ values of PM are relatively lower than those of the alloys. On the positive side, the valuable aspects of the PM are that $-\Delta S_M$ and T_C can

14492 | *Phys. Chem. Chem. Phys.*, 2024, **26**, 14476–14504

This journal is © the Owner Societies 2024

be easily tuned at room temperature, making researchers extensively explore materials for obtaining better MCE properties with ideal criteria. Several important parameters in PM will be discussed in the following section.

4.1 Types of substitution in perovskite manganites

The effect of substitution in PM materials is on the exchange interactions that occur. There are two possible interactions, namely the double-exchange (DE) interaction between Mn^{3+}–O^{2-}–Mn^{4+} and the super-exchange (SE) interaction between Mn^{3+}–O^{2-}–Mn^{3+}.[18] Fig. 5 shows the principles of exchange interactions. It is believed that if part of the trivalent ion, A-sites, in the perovskite material is replaced by a lower valence material and part of Mn^{3+} is replaced by Mn^{4+}. As a result, the spin in the e_g orbit becomes vacant, and O^{2-} acts as a bridge between two manganese states in the DE interaction.[131] For example, if A-sites are substituted with divalent ions, the equation becomes $R_{1-x}^{3+}A_x^{2+}Mn_{1-x}^{3+}Mn_x^{4+}O_3^{2-}$. Substitution in PM materials is categorized into three groups: substitution at site-A, site-B, and vacancy.[18,132–141] The determination of these three substitution methods in PM materials is based on considerations of ion valence, ion size, and crystal structure.

4.1.1 Substitution in A-sites of perovskite manganite systems. Substitution at the A-site has numerous variations that result in different magnetic moments, valence states, and ionic radii to generate a mixed valence of Mn^{3+} and Mn^{4+}. This mixed valence allows the generation of DE at low temperatures, leading to ferromagnetic materials, accompanied by changes in the average ion radii on the A-site, crystal structure, and magnetic moments. The effects of DE and MCE on the material will result in various magnetic order phenomena such as charge order, orbit order, and coupling together. These conditions will influence the values of T_C and $-\Delta S_M$.[18] The substitution at the A-site can consist of two types: single-ion substitution (Na, K, Ag, Li, *etc.*) and double-ion substitution (Sr, Ca, Mg, Ba, *etc.*). It is known that different valence conditions and ionic radius due to substitution have different effects on the structure, T_C, and MCE in $LaMnO_3$.[142] For instance,

SCHEME OF EXCHANGE INTERACTION Mn-O-Mn

● **Mn**   ● **O**

SUPER EXCHANGE INTERACTION

Mn^{3+} e^- O^{2-} e^- Mn^{3+}

DOUBLE EXCHANGE INTERACTION

Mn^{3+} e^- O^{2-} e^- Mn^{4+}

Fig. 5   Schematic of exchange interactions in PM systems.

substitution at the A-site includes $La_{0.7}Ca_{0.3}MnO_3$,[117] and $La_{0.7}Ba_{0.05}Ca_{0.25}MnO_3$.[77] which exhibit higher $-\Delta S_M$ values than $LaMnO_3$. Based on several studies, it can be concluded that A-site substitution with low-valence ions significantly influences changes in magnetic entropy and T_C, often exhibiting extreme values that need to be considered for the effects of substitution in Mn^{3+}/Mn^{4+} in the material system.[18,77,117,119,121,143]

4.1.2 Substitution in B-sites of perovskite manganite systems. Substitution at the B-site involves replacing Mn ions with specific ions to tailor T_C and increase the magnetic moment, which can enhance the value of $-\Delta S_M$.[18,137,144] The elements substituted at the B-site are transition metals (Ni, V, Fe, Co, Cr, and Cu). Al-Shahumi *et al.* reported an investigation on $La_{0.7}Sr_{0.3}Mn_{1-x}Fe_xO_3$ ($x = 0.0$–0.30) compounds, where the T_C values decreased from 370 to 98 K, accompanied by a decrease in the $-\Delta S_M$ values from 1.83 to 0.13 J kg^{-1} K^{-1}. The linear decrease in the T_C and $-\Delta S_M$ values are due to the weakening of the DE interaction, which affects the reduction in the magnetic interaction between the Mn magnetic moments. Additionally, the saturation magnetization decreased with increasing Fe concentration. The addition of Fe resulted in competition between SE and DE interactions. This is because the e_g and t_{2g} electrons in Fe^{3+} ions participate in the SE interaction with neighboring Mn and Fe ions in the lattice.[137] Researchers Riahi *et al.* also reported on $La_{0.7}Ca_{0.15}Sr_{0.15}$-$Mn_{1-x}Gd_xO_3$ ($x = 0.00$–0.06), which exhibited decreasing T_C values from 338 to 203 K and $-\Delta S_M$ values from 0.344 to 0.629 J kg^{-1} K^{-1} under a magnetic field of 1 T.[124] It can be concluded that substitution at the B-site results in the value of lower T_C and $-\Delta S_M$ values than doping at the A-site. This is because the natural magnetism of perovskite manganese oxide and MCE is caused by DE based on Mn^{3+}–O^{2-}–Mn^{4+}. Another reason for doping at the B-site being weaker than the A-site is attributed to: 1. The change in T_C is directly dependent on the exchange interactions that occur. 2. After doping, the dopant ions replace one of the Mn^{3+}–O^{2-}–Mn^{4+} ions in the DE.[18,124,137]

4.1.3 Vacancy substitution in perovskite manganite systems. The last type is the vacancy substitution ($\square$), which reduces the composition either at the A-site or B-site. Vacancy substitutions are divided into two categories: vacancy substitution in oxygen or elements.[18] Vacancy substitution in PM materials oxygen sites tends to reduce the T_C and $-\Delta S_M$ values because the decreased DE interactions occur. The reduction in DE interactions can be associated with oxygen ions playing a crucial role as a bridge between two Mn^{3+} and Mn^{4+} ions. Therefore, if the oxygen ions are reduced, and the Mn^{3+}–O^{2-}–Mn^{4+} interactions are not optimal. On the other hand, if vacancy substitution occurs at element sites, it will affect the composition of Mn^{3+} and Mn^{4+} ions.[145–152] The appearance of Mn^{4+} ions can be linked to the ability of the system to maintain its chemical stability by converting Mn^{3+} ions to Mn^{4+}, allowing the chemical equation to become $La_{(1-x)}^{3+}\square_xMn_{(1-y)}^{3+}$-$Mn_{2y}^{4+}O_3^{2-}$.[114]

Patra *et al.* examined a vacancy substitution in $La_{0.9}MnO_3$ samples, presenting a $-\Delta S_M$ value of 4.9 J kg^{-1} K^{-1} with $T_C = 254$ K under a magnetic field of 2 T, which was larger than the
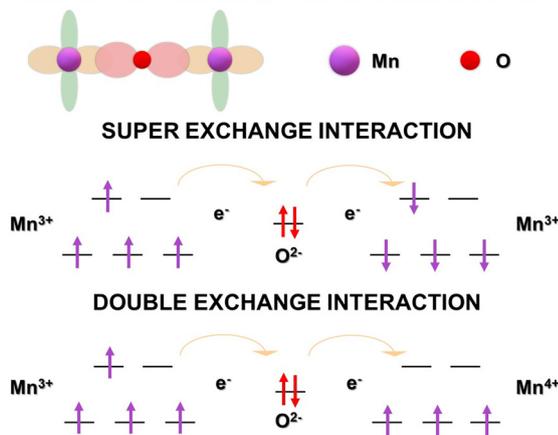
parent compound LaMnO$_3$. Additionally, Sankar and Joy investigated the magnetic properties of La$_{1-x}$MnO$_3$, and reported an increasing trend in T_C and magnetization with the increasing x content. The T_C value increased from 116 to 240 K with x from 0.03 to 0.13.[153] The increase in the T_C value in the system is associated with the increased amount of Mn^{4+} ions, strengthening the occurrence of DE interactions. Moreover, it is known that vacancy substitution also significantly influences lattice distortion and decreases the ionic radius at the A-site, which is another factor in controlling the T_C value.[18]

4.2 Composition of perovskite manganite systems

The determination of the system's composition can estimate the amounts of Mn^{3+} and Mn^{4+} ions. Known Mn^{3+}/Mn^{4+} ion ratio close to 2/1 or 7/3 will present excellent MCE properties because the strong DE interactions occur in the ferromagnetic state.[16] On the other hand, the composition also influences the occurrence of Jahn–Teller distortion.[18] Schiffer *et al.* studied the magnetic property behavior of La$_{1-x}$Ca$_x$MnO$_3$ with increasing x, presenting three magnetic phase regions: paramagnetic, ferromagnetic, and antiferromagnetic.[154] Another example is the investigation by Szewczyk *et al.* into La$_{1-x}$Sr$_x$MnO$_3$, where the addition of x shows regions of ferromagnetic, paramagnetic, and antiferromagnetic phases.[155–157] Ju *et al.* also investigated the magnetic phase behavior of La$_{1-x}$Ba$_x$MnO$_3$, which exhibits a ferromagnetic phase.[158] The phase diagrams for these three examples are clearly illustrated in Fig. 6(A). In this case, the subs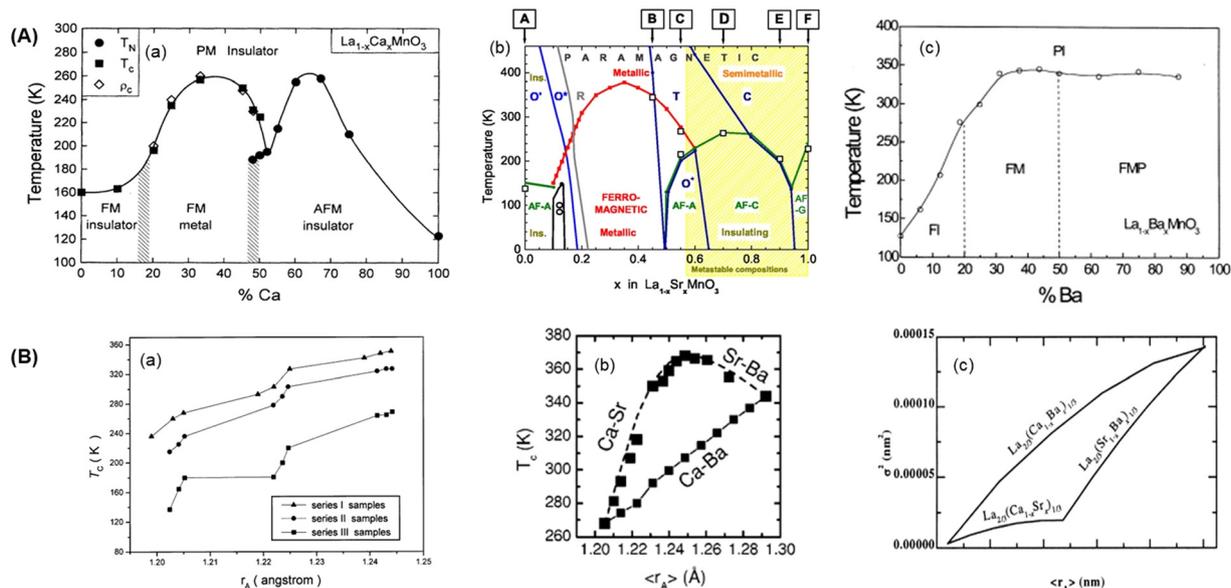titution with divalent ion and composition with x = 0.3 show ferromagnetic behavior. This demonstrates the correlation between strong DE interactions and the ferromagnetic behavior of the PM system. Therefore, considering the composition or amount of doping used is one of the considerations for predicting the material's properties.

4.3 Crystal structures

The substitution in PM materials can influence the crystal structure due to changes in the substituted ionic radius. The discussion on the crystal structure of PM materials will be related to several factors such as the average ionic radius at site-A, mismatch effect (σ^2), Goldsmith tolerance (t), and Jahn–Teller distortion. These four factors will aid in predicting the characteristics of the samples, particularly PM materials. The factors mentioned above will be discussed in more detail below.

4.3.1 Average ionic radius size factor at site-A. Substitution at site-A in the PM system will alter the average radius size of the ions at site-A. To estimate its size, a formulation has been proposed as defined below.[17]

$$\langle r_A \rangle = \Sigma x_i r_i \tag{13}$$

where, $\langle r_A \rangle$ is the average ion radius size, x_i is the ion content in the system, and r_i is the ion radius size in the system. Fig. 6(B)(a) displays the experimental results of the influence of $\langle r_A \rangle$ on the T_C of the PM materials. Wang *et al.* reported Ln$_{1-x}$T$_x$MnO$_3$ (series I), Ln$_{1-x}$T$_x$Mn$_{0.9}$Cr$_{0.1}$O$_3$ (series II), and Ln$_{1-x}$T$_x$Mn$_{0.9}$Fe$_{0.1}$O$_3$ (series III) where Ln is La, (La, Nd), and (La, Y), while T is Ca, CaSr, and Sr.[159] The results demonstrated

that an increase in the average ionic radius size leads to an increase in the T_C value. Abdelmoula *et al.*, also investigated the differences in the size of $\langle r_A \rangle$ in La$_{0.7}$Sr$_{0.3-x}$Ca$_x$MnO$_3$ and La$_{0.7-x}$Pr$_x$Sr$_{0.3}$MnO$_3$ materials, yielding similar results to Wang *et al.*[160] On the other hand, Ulyanov *et al.* conducted experiments to prove this in different compound compositions. These were divided into three groups: La$_{0.7}$Ca$_{0.3-x}$Sr$_x$MnO$_3$ (X), La$_{0.7}$Ca$_{0.3-x}$Ba$_x$MnO$_3$ (Y), and La$_{0.7}$Sr$_{0.3-x}$Ba$_x$MnO^3 (Z). Fig. 6(B)(b) presents groups X and Y with increased T_C with an increase in $\langle r_A \rangle$, while the opposite phenomenon occurs in compound Z.[161] Some researchers believe that there are other influencing factors, namely the mismatch effect, which will be discussed in the next section. Therefore, it was concluded that the influence of $\langle r_A \rangle$ on T_C can increase or decrease depending on the material.

4.3.2 Goldscmith tolerance factor (t). Substitution in the PM system will alter the crystal structure, originally cubic, into orthorhombic or rhombohedral due to decreasing its symmetry level. This is associated with decreasing in the Mn–O–Mn bond angle and shifting in the MnO$_6$ octahedral structure to another crystal structure. Previous researchers concluded a relationship between changes in crystal structure and goldsmith tolerance factor (t).[1,48,113,115,162] This factor is defined by eqn (14).

$$t = \frac{\langle r_A \rangle + r_O}{\sqrt{2}(\langle r_B \rangle + r_O)} \tag{14}$$

where, $\langle r_A \rangle$ dan $\langle r_B \rangle$ are the average ionic radii sizes of sites A and B, respectively, and r_O is the radius of the oxygen ion. There are three ranges of t values, each corresponding to a crystal structure. For t = 1, a perfect cubic crystal structure was observed.[1] In the range $0.96 < t < 1$, it indicates the occurrence of a rhombohedral symmetrical crystal structure. Meanwhile, in the range $t < 0.96$ or $0.75 < t < 0.96$ an orthorhombic crystal structure is formed.[48] Sakka *et al.* demonstrated that Pr$_{0.5}$Eu$_{0.1}$Sr$_{0.4}$MnO$_3$ and Pr$_{0.5}$Eu$_{0.1}$Sr$_{0.4}$MnO$_3$ with t values of 0.9287 and 0.9266, respectively, have an orthorhombic crystal structure.[48] Additionally, Razaq *et al.* reported that La$_{0.8}$K$_{0.1}$Ba$_{0.05}$Sr$_{0.15}$MnO$_3$ has a t value of 0.965, displaying a rhombohedral structures.[17]

4.3.3 Mismatch effect (σ^2). The determination of the system's composition can estimate the amounts of Mn^{3+} and Mn^{4+} ions. Known Mn^{3+}/Mn^{4+} ion ratio close to 2/1 or 7/3 will present excellent MCE properties because the strong DE interactions occur in the ferromagnetic state.[16] On the other hand, the composition also influences the occurrence of Jahn–Teller distortion.[18] Schiffer *et al.* studied the magnetic property behavior of La$_{1-x}$Ca$_x$MnO$_3$ with increasing x, presenting three magnetic phase regions: paramagnetic, ferromagnetic, and antiferromagnetic.[154] Another example is the investigation by Szewczyk *et al.* into La$_{1-x}$Sr$_x$MnO$_3$, where the addition of x exhibited regions of ferromagnetic, paramagnetic, and antiferromagnetic phases.[155–157] Ju *et al.* also investigated the magnetic phase behavior of La$_{1-x}$Ba$_x$MnO$_3$, which exhibits a ferromagnetic phase.[158] The phase diagrams for these three examples are clearly illustrated in Fig. 6(A). In this case, the substitution with divalent ion and composition with x = 0.3

14494 | *Phys. Chem. Chem. Phys.*, 2024, **26**, 14476–14504

This journal is © the Owner Societies 2024

Fig. 6 Phase diagram of substituted PM materials in (A) (a) $La_{1-x}Ca_xMnO_3$ reprinted with permission, copyright 1995, American Physics Society,[154] (b) $La_{1-x}SrMnO_3$ reprinted with permission, copyright 2005, American Physical Society,[157] (c) $La_{1-x}Ba_xMnO_3$ reprinted with permisson, copyright 2000, Elsevier,[158] (B) graph of influencing $\langle r_A \rangle$ to T_C reprinted with permision (a), copyright 2001, Elsevier,[159] (b), copyright 2002, American Institute of Physics[161] and (c) the influence $\langle r_A \rangle$ to cation mismatch effect reprinted with permission, copyright 2002, Elsevier.[165]

show ferromagnetic behavior. This demonstrates the correlation between strong DE interactions and the ferromagnetic behavior of the PM system. Therefore, considering the composition or amount of doping used is one of the considerations for predicting the material's properties.

Other parameters related to magnetic properties such as T_C, $-\Delta S_M$, and magnetic phase transition are the mismatch effect (σ^2).[1] In perovskite manganite (PM) materials, a large value of σ^2 is defined as the difference in the ion radius values for each ion at site-A compared to $\langle r_A \rangle$, and it can be formulated as follows:[8,162–164]

$$\sigma^2 = \Sigma x_i r_i^2 - \langle r_A \rangle^2 \qquad (15)$$

where, $\langle r_A \rangle$ is the average ion radii size, x_i is the ion content in the system, and r_i is the ion radii size in the system. For example, Razaq et al. calculated the σ^2 values for $La_{0.8}K_x$-$Ba_{0.05}Sr_{0.15-x}MnO_3$ ($x = 0.00–0.20$) with results from 3.833×10^{-3} to 18.101×10^{-3}.[17] Additionally, Bangrong He et al. reported $La_{0.8-x}Gd_xSr_{0.2}MnO_3$ ($x = 0.00–0.10$) with σ^2 values from 1.024×10^{-3} to 7.594×10^{-3}.[164] Both studies reported changes in their physical and magnetic properties which are connected to local lattice distortion with a random placement of oxygen. Moreover, mismatch effect plays a role in controlling the type of magnetic phase transition and T_C values.[1,17,18,164] Yuan et al. revealed a correlation between the mismatch effect values and $\langle r_A \rangle$, producing a pattern similar to the T_C pattern in the cases of compounds X, Y, and Z.[165] This correlation is depicted in Fig. 6(B) point (d). Furthermore, it has been widely reported that an increase in the mismatch effect on the size of site-A leads to slightly less magnetic and MCE properties.[1]

4.3.4 Jahn–Teller distortion. The last parameter influencing crystal structure is Jahn–Teller distortion. This phenomenon

is associated with structural changes in materials, where in the case of PM, a cubic structure becomes distorted into an orthorhombic or rhombohedral structure. For example, in PM materials, Mn ions, due to the difference in energy levels in the 3d orbitals, especially in the t_{2g} and e_g orbitals, lead to sample-specific compositions and average ion radius sizes.[1,166]

4.4 Materials production methods

The performance of materials is determined by several crucial factors, one of which is the production method. Previous studies on the production of PM materials have employed various methods. The choice of production method plays a crucial role in investigating MCE properties as it is highly sensitive to the material's characteristics. Some of the methods used by researchers consist of solid-state reaction (SSR),[167–171] sol–gel (SG),[16,17,164] polyol (P), solvothermal (ST),[24] ball milling (BM) or high energy ball milling (HEBM),[116,117,172] pore-wetting (PW),[23] wet-mixing (WM),[16] hydrothermal (HT) methods,[1] etc. It is known that each method has its own targeted advantages.

The most commonly used production methods are SSR, SG, and BM. The SSR method is widely employed because it is easy to make. The SSR method is advantageous for MCE materials since it enhances crystallinity and reduces crystal boundaries, which are magnetically dead areas.[1] However, it should be noted that the mixing process can impact to get desired compounds, since it may lead to non-homogeneous particle sizes. To address this, the BM method was developed by utilizing milling machines to achieve homogenous particle sizes. In general, the process involves combining all precursors, breaking them down, and reuniting them to reduce the particle size, modify the shape and structure, and combine all precursors.[52,117] However, both SSR and BM methods have

This journal is © the Owner Societies 2024

Phys. Chem. Chem. Phys., 2024, **26**, 14476–14504 | **14495**

drawbacks, such as higher sintering temperatures (>1273 K) and longer holding times (>24 hours) to obtain the compounds.[52] Some materials produced using SSR and BM methods include $La_{0.7}Sr_xCa_{0.3-x}MnO_3$,[117] $La_{0.65}Ba_{0.30-x}\square_x$-$MnO_3$,[168] and $La_{0.63}Ca_{0.29}Sr_{0.04}MnO_3$.[167]

The SG method is preparation to obtain ceramic materials from solids transformed into a gel. This method is often associated with the use of citric acid and ethylene glycol in the manufacturing process. Citric acid is used as a complexing agent and combustion aid, while ethylene glycol is used as a polymerization agent. Many researchers use the SG method due to its advantages such as the manufacturing process, short experimental cycles, production of more homogenous particle sizes, adjustable sintering temperatures, and shorter sintering treatment times compared to SSR and BM methods.[16,164] However, materials produced using the SG method tend to have lower crystallinity than those produced using the SSR method.[1] Some materials produced using the SG method include $La_{0.7}Ca_{0.1}Sr_{0.1}Ba_{0.1}MnO_3$,[16] $La_{0.8-x}K_xBa_{0.05}Sr_{0.15}MnO_3$,[17] and $La_{0.7}Gd_xSr_{0.3-x}MnO_3$.[164]

4.5 Effect of heat treatment

The heat treatment process plays a crucial role in PM materials production. The most frequently used methods are dehydration, calcination, annealing, and sintering. The dehydration process involves heating to evaporate water content from the compound at low temperatures ranging from 373 to 473 K over a specific duration. Calcination is a heat treatment process with a specific temperature without melting the compound, using or not using a specific gas, aiming to remove impurities and cause thermal decomposition.[16] Meanwhile, annealing is a heating process for compounds with purposing to alter the physical and chemical properties of samples, such as reducing stress to facilitate subsequent manufacturing processes. The last, sintering process involves heating the material at high temperatures but below its melting point for a specific duration, aiming to promote crystal growth (nucleation) accompanied by atomic diffusion.[1]

One of the methods to determine the sintering temperature is differential thermal analysis (DTA) and thermogravimetric analysis (TGA) measurements. DTA measurements are used to determine the temperature difference between the reference and the sample during heating. Commonly, DTA measurements display two types of peaks such as exothermic and endothermic below the melting point detected in TGA. On the other hand, TGA measurements show the weight change of the material with increasing applied temperature. The results of the measurements allowed for the detection of mass reduction caused by the loss of solvent, impurities, and sample material.[1] For example the DTA–TGA curve results from Kumar et al., recommended a sintering temperature above 1023 K for the $LaMnO_3$ sample.[173]

It is known that the sintering and compaction processes have several methods such as conventional sintering, hot pressing sintering, and spark plasma sintering.[9,30,31,33,40,118,120,174,175] Most researchers use the conventional method to obtain PM materials. However, the development of sintering processes using SPS and HPS methods has become popular because of faster cycles. The SPS method is an advanced technology used to produce high-density bulk, where the sintering and compaction processes occur simultaneously. SPS has a thickness change sensor component that can monitor during the sintering process by adjusting the heating rate and holding time, offering the advantage of a shorter processing time.[33,40,118,120] On the other hand, HPS is a sintering method combined with sample compression at a specific temperature, but its heating rate is not as fast as SPS. Moreover, it has been reported that the mechanical properties of SPS are superior to conventional sintering and HPS methods, demonstrated by lower porosity, higher density, and other mechanical properties.[30,31] The popularity of the SPS method is also used for investigating MCE properties. Khlifi et al. reported an investigation on $La_{0.6}Ca_{0.2}Ba_{0.2}MnO_3$ by comparing synthesis and sintering methods in their research. The synthesis method used was SSR followed by conventional sintering, and the P method followed by SPS. They reported that the MCE properties of the P method followed by SPS had values of $-\Delta S_M = 4.5$ J kg^{-1} K^{-1} and RCP = 244 J kg^{-1}, which were larger than the SSR method followed by conventional sintering.[40]

4.6 Effect of morphology and grain size

Most of the PM materials produced are polycrystalline materials because they are easier to synthesize than single-crystal materials, which are identified through X-ray diffraction (XRD) measurements. Both polycrystalline and single-crystal materials can be morphologically characterized through scanning electron microscope (SEM) and energy dispersive spectroscopy (EDS) measurements. SEM measurements were conducted to determine morphology, size, and grain arrangement. Meanwhile, EDS measurements serve as elemental analyses of the material.

Fig. 7 presents the SEM results of $La_{0.7}Ba_{0.1}Ca_{0.1}Sr_{0.1}MnO_3$ with variations in synthesis methods, SG, and WM, where the morphological shape appears as spheres with specific grain sizes and clear grain boundaries in both samples.[16] It can be observed that the grain size of the SG sample is larger than that of the WM sample. The presented differences in grain size affect the MCE properties and T_C, where larger grain sizes can enhance the values of $-\Delta S_M$ and T_C.[176] Andrade et al. also reported $La_{0.6}Ca_{0.4}MnO_3$ with the smallest grain size of 23 nm and the largest grain size of 223 nm, showing an increase in $-\Delta S_M$ values from 0.3 J kg^{-1} K^{-1} to 8.3 J kg^{-1} K^{-1} and RCP values from 40 J kg^{-1} to 508 J kg^{-1}.[23] Additionally, Yadav et al. studied the magnetic properties of $La_{0.7}Sr_{0.3}MnO_3$, indicating that larger grain sizes can influence magnetization values and increased coercivity fields related to non-magnetic layers on the surface of each grain.[73]

5. Analysis of magnetic properties and magnetocaloric data of perovskite manganite materials

After understanding the parameters that influence the magnetic properties and MCE of PM materials, a deeper understanding is
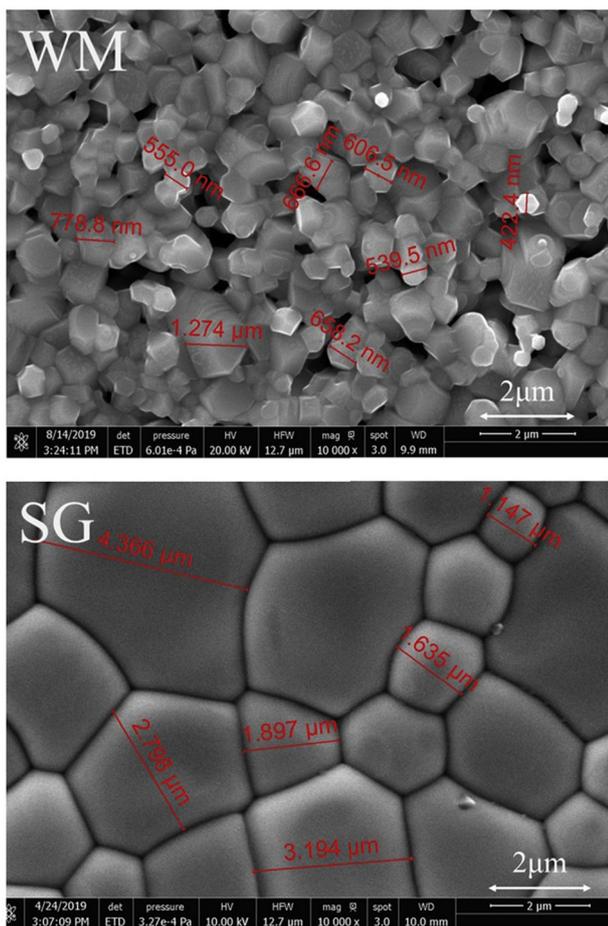
14496 | *Phys. Chem. Chem. Phys.*, 2024, **26**, 14476–14504

This journal is © the Owner Societies 2024

Fig. 7 The morphology of SEM results sample $La_{0.7}Ba_{0.1}Ca_{0.1}Sr_{0.1}MnO_3$ compound with production method SG dan WM reproduced from ref. 16 with permission from Elsevier, copyright 2020.[16]

needed for an analysis of the data. Based on several previous studies discussing MCE, the data usually presented in reports include temperature dependence curves on magnetic fields (M–T), temperature inverse susceptibility ($\chi^{-1} - T$), magnetic field–isothermal magnetization (M–H), arrow plot ($H/M - M^2$), universal curve $\left(\dfrac{\Delta S_M}{\Delta S_M^{max}} - \theta\right)$, and MCE parameters. When presenting data, don't just show it as it is. Instead, calculations and analysis are required to understand their behavior. A more detailed discussion will be presented in the following section.

5.1 Analysis and measurement of temperature dependence on magnetization ($M - T$)

It is known that temperature dependence on magnetization measurements for magnetic and MCE properties investigations of materials. M–T measurements are conducted with different modes such as zero field cooled (ZFC), field cooled (FC), and field heated (FH). Generally, these measurements are conducted to determine the point of the ferromagnetic to paramagnetic phase transition and the T_C value of the PM material, which is related to the appearance of the highest magnetic entropy change. Thus, it can be concluded that M–T

measurements are crucial for investigations in determining the working temperature range of magnetic refrigeration materials.

Fig. 8(A) exhibits M–T curve analysis results from Munazat *et al.* report, showing that both samples undergo a phase transition from ferromagnetic to paramagnetic states with increasing temperature. This is marked by a significant decrease in magnetization around T_C as many research results.[20,60,115] To determine T_C value more accurately, an analysis of the phase transition temperature is needed, where the determination is done by deriving M–T to temperature (dM/dT). The analysis for determining the T_C value was also conducted by Munazat *et al.*, stating that the T_C values for $La_{0.7}Ba_{0.1}Ca_{0.1}Sr_{0.1}MnO_3$ samples are 330.81 K and 316.17 K for SG and WM samples, respectively.[16]

5.2 Analysis and measurement of temperature dependence on inverse susceptibility ($\chi^{-1} - T$)

Futhermore, analysis of the $\chi^{-1} - T$ curve data was carried out to determine T_C value as another alternative approach to the M–T curve and effective magnetic moment value associated with the Curie–Weiss Law. The Curie–Weiss Law equation for ferromagnetic materials can be described by the following expression:[16]

$$\chi = \frac{C}{T - \theta_{CW}} \tag{16}$$

$$\chi^{-1} = \frac{1}{C}T - \frac{1}{C}\theta_{CW} \tag{17}$$

where χ is the material susceptibility, θ_{CW} is the Curie–Weiss temperature, and C is the Curie constant. In determining the Curie–Weiss temperature, a transformation of the function into the $\chi^{-1} - T$ curve is needed, and the Curie constant is defined as follow:[16]

$$C = \frac{N_A}{3K_B}\mu_{eff}^{exp\,2}\mu_B^2 \tag{18}$$

where, N_A is Avogadro's number, K_B is the Boltzmann constant, μ_{eff}^{exp} is the experimental effective magnetic moment, and μ_B is the Bohr magneton.

Fig. 8(B) presents the analysis of inverse susceptibility *versus* temperature for $La_{0.7}Ba_{0.1}Ca_{0.1}Sr_{0.1}MnO_3$. In their report, Munazat *et al.* state that the presented data suits Curie–Weiss Law due to the linear behavior of the graph in the paramagnetic region.[16] The estimated lines of paramagnetic behavior intersect x-axis at the Curie paramagnetic temperature (T_C or θ_{CW}) values of 331.1 K and 337.5 K for the WM and SG samples, respectively. If the sample does not have good magnetic homogeneity, the T_C values from the $\chi^{-1} - T$ analysis may differ from the M–T analysis. Additionally, the dominance of ferromagnetic conditions in the paramagnetic region may lead to the presence of Griffith phases and anomalies.[113,128,177,178] These anomalies are characterized by the absence of a straight-line behavior in the paramagnetic region.[128,177–179]

This journal is © the Owner Societies 2024

Phys. Chem. Chem. Phys., 2024, **26**, 14476–14504 | **14497**

In addition, the Curie constants obtained from the analysis of the slopes of the straight lines above provide $\mu_{\text{eff}}^{\text{exp}}$ values for the Munazat *et al.* samples of $5.36\mu_{\text{B}}$ and $5.80\mu_{\text{B}}$ for the WM and SG samples, respectively.[16] These results do not align with an effective magnetic moment value calculated as $\mu_{\text{eff}}^{\text{cal}}$ ($4.61\mu_{\text{B}}$). According to them, the discrepancy is attributed to the presence of non-homogeneous magnetic states, particularly in the temperature transition region of the samples. Additionally, this difference is also linked to the presence of short-range ferromagnetic interactions above T_{C}.[16]

5.3 Analysis and measurement of isothermal magnetization (M–H)

These measurements are conducted to obtain the isothermal M–H curve, which is used as data for indirectly calculating the $-\Delta S_{\text{M}}$ value from the PM sample. Additionally, this data serves as a tool for analysing the type of phase transition in PM samples by utilizing the Arrot plot. It is noteworthy that previous research suggests the need for special treatment in the isothermal M–H measurements of FOMT-type materials to reduce errors in $-\Delta S_{\text{M}}$. Therefore, FOMT-type materials are recommended to be measured using direct methods.[35] Meanwhile, for SOMT-type samples, no special treatment is required.[1] Fig. 8(C) provides a general illustration of isothermal M–H measurements conducted around T_{C} with constant temperature changes.[16] Isothermal M–H curves in MCE materials typically exhibit a sharp increase in magnetization with a slight change in magnetic field (ferromagnetic phase behavior below T_{C}) and almost become a straight line approaching saturation when
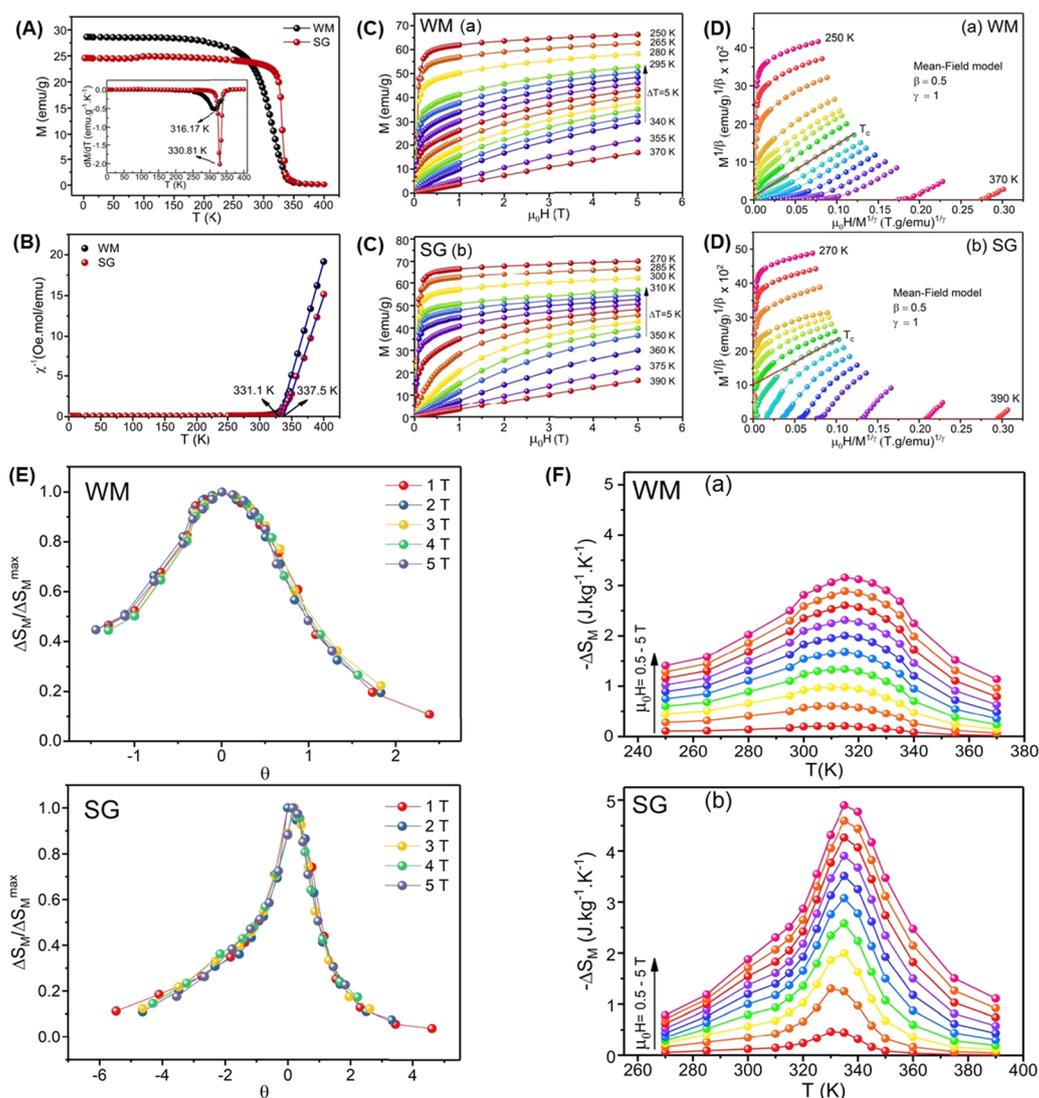
Fig. 8 The results of the magnetic properties and MCE analysis of the La$_{0.7}$Ba$_{0.1}$Ca$_{0.1}$Sr$_{0.1}$MnO$_3$ compound with different production methods, (a) WM (wet-mixing), and (b) SG (sol–gel), are presented. The figures include (A) temperature dependence on a magnetic field of 0.05 T, (B) inverse susceptibility *versus* temperature, (C) isothermal magnetization, (D) Arrot plot, (E) universal curve analysis, and (F) curve of magnetic entropy change *versus* temperature where all of the pictures reproduced from ref. 16 with permission from Elsevier, copyright 2020.[16]

14498 | *Phys. Chem. Chem. Phys.*, 2024, **26**, 14476–14504

This journal is © the Owner Societies 2024

reaching high magnetic fields (paramagnetic phase behavior above T_C).[1,180–182]

5.4 Analysis of phase transition types utilizing Arrot plot

To determine magnetic phase transition types, many researchers utilize the Arrot plot ($H/M – M^2$). As mentioned earlier, the data used for the Arrot plot comes from isothermal $M–H$ data. According to the Banerjee criteria, the type of transition can be illustrated by the slope of the graph. FOMT transitions have a negative slope, while SOMT transitions have a positive slope.[1,183–186] This determination is crucial because MCE materials depend on the type of magnetic transition, as explained earlier. Certainly, Banerjee's criteria and the formulation of the Arrot plot can be defined quantitatively from Landau theory. This theory is considered to originate from the Gibbs free energy ($G(M, T)$) as a function of the magnetic field, which can be expressed as a power series expansion:[187]

$$G(M, T) = G_0 + \frac{1}{2}a(T)M^2 + \frac{1}{4}b(T)M^4 \ldots - \mu_0 HM \quad (19)$$

In thermal equilibrium conditions $\left(\frac{\partial G}{\partial M} = 0\right)$ the magnetic state equation is obtained as:

$$\frac{\mu_0 H}{M} = a(T) + b(T)M^2 \quad (20)$$

eqn (20), known as the Arrot plot formula, presents two Landau coefficients namely $a(T)$, and $b(T)$. Generally, the minimum value of $a(T)$ represents the T_C value according to the Landau expansion characteristics. On the other hand, $b(T)$ in the Landau expansion indicates the type of phase transition that occurs at a specific temperature. At $b(T_C)$, it will confirm the type of magnetic phase transition that occurs; if $b(T_C) < 0$, it indicates FOMT, and if $b(T_C) \geq 0$, it indicates SOMT.[48] For example, experimental results can be seen in Fig. 8(D), which presents the Arrot plot of $La_{0.7}Ba_{0.1}Ca_{0.1}Sr_{0.1}MnO_3$ synthesized using the WM and SG methods.[16] Munazat et al. revealed that their sample exhibited SOMT transition type, characterized by its positive slope as indicated at T_C.[16]

5.5 Analysis of phase transition types utilizing universal curve

Not only is the analysis carried out using the Arrot plot, but also Franco et al. proposed an analysis of magnetic phase transitions using the universal curve.[188,189] They revealed that a material exhibiting FOMT transitions would not have its universal curve merging, while for SOMT transitions, the universal curve would merge into a single line, regardless of the applied magnetic field magnitude. In the analysis of the universal curve, normalization of the axis $\frac{\Delta S_M}{\Delta S_M^{max}}$ is performed, and rescaling is applied to the θ axis, defined as follows:[16,190]

$$\theta = \begin{cases} (T_C - T)/(T_{r1} - T_C), & (T \leq T_C) \\ (T - T_C)/(T_{r2} - T_C), & (T > T_C) \end{cases} \quad (21)$$

Where, T_{r1} and T_{r2} are the temperature values of two reference points chosen based on $\frac{\Delta S_M}{\Delta S_M^{max}} = 0.5$. Munazat et al.

demonstrated the analysis of SOMT transition type with the merging of $-\Delta S_M$ values into a single line in their sample, as shown in Fig. 8(E).[16] Additionally, Bonilla et al. conducted an investigation of the universal curve for $RECo_2$ (RE = Tb, Pr, Nd, Ho, Dy), showing universal curve results for both FOMT and SOMT transition types, as proposed by Franco et al.[191]

5.6 Parameter of MCE properties measurements corellated by Landau theory

As discussed in the subsection on fundamental aspects of MCE property parameters, $-\Delta S_M$ and RCP are crucial. However, when processing experimental $-\Delta S_M$ data, most researchers use the discrete version of eqn (7).[64] Additionally, it can also be calculated using the equation derived from Landau theory, which is obtained from the relationship between entropy and the Landau theory derivative to temperature, as follows:

$$-\Delta S_M(T, H) = \frac{1}{2}a'(T)M^2 + \frac{1}{4}b'(T)M^4 \quad (22)$$

Fig. 8(F) presents the results of the calculation of magnetic entropy change from the study by Munazat et al.[16] Thus, all the MCE materials discussed here will be summarized in Table 2, which contains important parameters for the MCE properties of the material.

6. Conclusion

The research progress on magnetocaloric effect (MCE) for application of magnetic refrigeration technology operating at room temperature has been intensifying. This development aims to envision a better future in terms of energy efficiency and environmental conservation, particularly by avoiding greenhouse gas effects and ozone layer depletion. Numerous types of MCE materials have been developed as alternatives to expensive and limited Gd-based materials ($\$\$4000$ per kg). Among the various proposed alternative materials, one stands out as an ideal MCE material – perovskite manganite. The emergence of MCE properties in perovskite manganite materials is linked to crucial parameters such as production methods, heat treatment, crystal structure, atom substitution (doping), compound composition, morphology and grain size, temperature dependence, and magnetic field dependence on magnetization. These parameters significantly influence MCE properties, represented by values like $-\Delta S_M$, ΔT_{ad}, and RCP. Considering all these crucial parameters and the increasing intensity of research on perovskite manganite-based MCE materials, they hold the potential to be permanently applied in magnetic refrigeration, replacing conventional refrigerator technologies.

Conflicts of interest

There are no conflicts to declare.

Acknowledgements

This journal is © the Owner Societies 2024

Phys. Chem. Chem. Phys., 2024, **26**, 14476–14504 | **14499**

grant "Penelitian Dasar Unggulan Perguruan Tinggi 2021" NKB-160/UN2.RST/HKP.05.00/2021.

References

1 A. O. Ayaş, S. K. Çetin, G. Akça, M. Akyol and A. Ekicibil, Magnetic refrigeration, *Mater. Today Commun.*, 2023, **35**, 105988.

2 D. Coulomb, J. L. Dupont and A. Pichard, *The Role of Refrigeration in the Global Economy*, 2015.

3 I. energy Agency, *The Future of Cooling: Opportunities for energy efficient air conditioning*, OECD, 2018.

4 M. H. Phan and S. C. Yu, *J. Magn. Magn. Mater.*, 2007, **308**, 325–340.

5 N. R. Ram, M. Prakash, U. Naresh, N. S. Kumar, T. S. Sarmash, T. Subbarao, R. J. Kumar, G. R. Kumar and K. C. B. Naidu, *J. Supercond. Nov. Magn.*, 2018, **31**, 1971–1979.

6 Y. Dong, M. Coleman and S. A. Miller, *Ann. Rev. Environ. Resources*, 2021, **46**, 59–83.

7 A. Kitanovski, *Adv. Energy Mater.*, 2020, **10**, 1903741.

8 W. Zhang, Z. Xie, Z. Zou, X. Jiang, C. Xu and M. Feng, *Ceram. Int.*, 2024, **50**, 4921–4935.

9 M. Z. Kurt, S. Kılıç Çetin, A. Kandemir, G. Akça, F. Karadağ and A. Ekicibil, *J. Mater. Sci.: Mater. Electron.*, 2024, **35**, 565.

10 O. Sari and M. Balli, *Int. J. Refrig.*, 2014, **37**, 8–15.

11 K. Rajamani, M. S. Toprak, F. Zhang, A. I. Dugulan, E. Brück, T. van der Meer and M. Shahi, *ACS Omega*, 2023, **8**, 49027–49036.

12 H. Gu, X. Zhang, H. Wei, Y. Huang, S. Wei and Z. Guo, *Chem. Soc. Rev.*, 2013, **42**, 5907–5943.

13 S. Solanki, D. Dhruv, H. Boricha, A. Zankat, K. N. Rathod, B. Rajyaguru, R. K. Trivedi, A. D. Joshi, S. Mukherjee, P. S. Solanki and N. A. Shah, *J. Solid State Chem.*, 2020, **288**, 121446.

14 L. Yin, C. Wang and Q. Shen, *Ceram. Int.*, 2023, **49**, 33392–33400.

15 W. Hizi, H. Rahmouni, K. Khirouni and E. Dhahri, *Phys. B*, 2024, **673**, 415423.

16 D. R. Munazat, B. Kurniawan, D. S. Razaq, K. Watanabe and H. Tanaka, *Phys. B*, 2020, **592**, 412227.

17 D. S. Razaq, B. Kurniawan, D. R. Munazat, K. Watanabe and H. Tanaka, *Crystals*, 2020, **10**(5), 407.

18 Z. Xie, Z. Zou, B. He, L. Liu and Z. Mao, *Front. Mater.*, 2021, **8**, 771941.

19 L. Li and M. Yan, *J. Mater. Sci. Technol.*, 2023, **136**, 1–12.

20 E. Bouzaiene, A. H. Dhahri, J. Dhahri and E. K. Hlil, *Inorg. Chem. Commun.*, 2021, **132**, 108824.

21 T. Gottschall, M. D. Kuz'Min, K. P. Skokov, Y. Skourski, M. Fries, O. Gutfleisch, M. G. Zavareh, D. L. Schlagel, Y. Mudryk, V. Pecharsky and J. Wosnitza, *Phys. Rev. B*, 2019, **99**, 134429.

22 A. M. Tishin, Y. I. Spichkin, V. I. Zverev and P. W. Egolf, *Int. J. Refrig.*, 2016, **68**, 177–186.

23 V. M. Andrade, R. J. C. Vivas, S. S. Pedro, J. C. G. Tedesco, A. L. Rossi, A. A. Coelho, D. L. Rocco and M. S. Reis, *Acta Mater.*, 2016, **102**, 49–55.

24 W. Chen, B. Hong, Y. Zeng, X. Wang, X. Peng, J. Li and J. Xu, *J. Alloys Compd.*, 2023, **933**(13), 22281–22293.

25 A. T. Coşkun, Y. S. Ak, N. Güleç, G. Akça, S. K. Çetin, A. Ekicibil and A. Coşkun, *J. Mater. Sci.: Mater. Electron.*, 2023, **34**, 1257.

26 K. Laajimi, M. Khlifi, E. K. Hlil, K. Taibi, M. H. Gazzah and J. Dhahri, *J. Mater. Sci.: Mater. Electron.*, 2019, **30**, 11868–11877.

27 K. Laajimi, F. Ayadi, M. Kchaw, I. Fourati, M. Khlifi, M. H. Gazzah, J. Dhahri and J. Juraszek, *Solid State Sci.*, 2019, **30**, 11868–11877.

28 M. Varga, L. Galdun, P. Diko, K. Saksl and R. Varga, *J. Alloys Compd.*, 2023, **944**, 169196.

29 T. Zheng, K. Liu, H. Chen and C. Wang, *J. Magn. Magn. Mater.*, 2022, **563**, 170034.

30 Y. C. Wu, Y. X. Li, X. C. Zhong, C. L. Liu, J. H. Huang, H. Y. Yu, Z. W. Liu, M. L. Zhong, Z. C. Zhong and R. V. Ramanujan, *Mater. Res. Bull.*, 2022, **156**, 111974.

31 X. C. Zhong, Y. C. Wu, S. M. Wu, Y. X. Li, J. H. Huang, C. L. Liu, H. Zhang, Z. W. Liu, M. L. Zhong, Z. C. Zhong and R. V. Ramanujan, *J. Alloys Compd.*, 2022, **902**, 163780.

32 H. Wang, G. F. Wang, Y. Bo and Y. Y. Ma, *J. Magn. Magn. Mater.*, 2024, **591**, 171727.

33 Z. R. Zhao, T. Jing, G. F. Wang, Y. F. Li, Q. Ma and X. F. Zhang, *J. Supercond. Nov. Magn.*, 2019, **32**, 993–999.

34 A. M. Chirkova, K. P. Skokov, Y. Skourski, F. Scheibel, A. Y. Karpenkov, A. S. Volegov, N. V. Baranov, K. Nielsch, L. Schultz, K. H. Müller, T. G. Woodcock and O. Gutfleisch, *Phys. Rev. Mater.*, 2021, **5**, 064412.

35 A. T. Sathyanarayana and A. Mani, *J. Alloys Compd.*, 2021, **862**, 158322.

36 J. Hu, C. Liu, M. Wang, M. Wang, S. Wang, G. Zheng and Y. Ma, *J. Solid State Chem.*, 2022, **314**, 123369.

37 J. Zhao, X. Liu, X. Kan, C. Liu, W. Wang, J. Hu, Q. Lv, J. Huang and M. Shazeda, *Ceram. Int.*, 2021, **47**, 7906–7917.

38 R. Felhi, H. Omrani, M. Koubaa, W. C. Koubaa and A. Cheikhrouhou, *J. Alloys Compd.*, 2018, **758**, 237–246.

39 N. Assoudi, I. Walha, E. Dhahri, S. Alleg and E. K. Hlil, *Solid State Commun.*, 2018, **277**, 13–18.

40 H. Ben Khlifa, F. Ayadi, R. M'nassri, W. Cheikhrouhou-Koubaa, G. Schmerber and A. Cheikhrouhou, *J. Alloys Compd.*, 2017, **712**, 451–459.

41 H. Ma, X. Jin, L. Gao, J. Zhao and J. Zhao, *J. Low Temp. Phys.*, 2024, **215**, 93–108.

42 A. Ezaami, N. Ouled Nasser, W. Cheikhrouhou-Koubaa and A. Cheikhrouhou, *Mater. Res. Bull.*, 2017, **95**, 211–215.

43 A. Ezaami, E. Sellami-Jmal, W. Cheikhrouhou-Koubaa and A. Cheikhrouhou, *J. Mater. Sci.: Mater. Electron.*, 2017, **28**, 16741–16746.

44 S. Tillaoui, B. Rabi, M. Sajieddine, A. Essoumhi, M. Emo, A. El Boubekri, M. Lassri, E. K. Hlil, M. Sahlaoui and A. Razouk, *Ceram. Int.*, 2024, **50**, 16375–16381.

45 A. M. Tishin and Y. I. Spichkin, *The Magnetocaloric Effect and its Applications*, Institute of Physics Publishing, Bristol and Philadelphia, 2003.

46 J. Y. Law and V. Franco, *Encycl. Mater.: Composites*, 2021, **2**, 461–472.

14500 | *Phys. Chem. Chem. Phys.*, 2024, **26**, 14476–14504

This journal is © the Owner Societies 2024

47 T. M. Al-Shahumi, I. A. Al-Omari, S. H. Al-Harthi and M. T. Z. Myint, *SN Appl. Sci.*, 2023, **5**, 121.

48 A. Sakka, R. M'nassri, M. M. Nofal, S. Mahjoub, W. Cheikhrouhou-Koubaa, N. Chniba-Boudjada, M. Oumezzine and A. Cheikhrouhou, *J. Magn. Magn. Mater.*, 2020, **514**, 167158.

49 J. Wang, H. Xie, Q. Liu, Z. Hao, Z. Mo, Q. Fu, X. Gao and J. Shen, *J. Rare Earths*, 2023, DOI: 10.1016/j.jre.2023.06.015.

50 X. Wang, L. Wang, N. L. Gulay, L. Li and R. Pöttgen, *J. Magn. Magn. Mater.*, 2024, **589**, 171406.

51 D. H. Manh, T. D. Thanh, D. H. Kim and T. L. Phan, *Curr. Appl. Phys.*, 2024, **60**, 70–78.

52 V. E. Salazar-Muñoz, A. Lobo Guerrero and S. A. Palomares-Sánchez, *J. Magn. Magn. Mater.*, 2022, **562**, 169787.

53 F. Zhang, K. Westra, Q. Shen, I. Batashev, A. Kiecana, N. van Dijk and E. Brück, *J. Alloys Compd.*, 2022, **968**, 164337.

54 A. Biswas, N. A. Zarkevich, A. K. Pathak, O. Dolotko, I. Z. Hlova, A. V. Smirnov, Y. Mudryk, D. D. Johnson and V. K. Pecharsky, *Phys. Rev. B*, 2020, **101**, 224402.

55 W. Lu, N. T. Nam and T. Suzuki, *J. Appl. Phys.*, 2009, **105**, 07A904.

56 S. N. Kaul and M. Rosenberg, *Philosophical Magazine B: Physics of Condensed Matter; Statistical Mechanics, Electronic, Optical and Magnetic Properties*, 1981, **44**, 357–368.

57 E. Rauwel Buzin, W. Prellier, C. Simon, S. Mercone, B. Mercey, B. Raveau, J. Sebek and J. Hejtmanek, *Appl. Phys. Lett.*, 2001, **79**, 647–649.

58 H. Zhang, X. Zhang, J. Tan, J. Yan, H. Shi, J. Zhang, H. Wei, H. Li, W. Li and A. Xia, *J. Alloys Compd.*, 2023, **953**, 170114.

59 V. K. Pecharsky and K. A. Gschneidner, *Phys. Rev. Lett.*, 1997, **78**, 4494–4497.

60 M. A. A. Bally, M. A. Islam, M. Z. Ahasan and F. A. Khan, *J. Magn. Magn. Mater.*, 2022, **557**, 169462.

61 A. Guedri, S. Mnefgui, S. Hcini, E. K. Hlil and A. Dhahri, *J. Solid State Chem.*, 2021, **297**, 122046.

62 E. Oumezzine, S. Hcini, M. Baazaoui, E. K. Hlil and M. Oumezzine, *Powder Technol.*, 2015, **278**, 189–195.

63 W. Chen, J. Xu, Y. Zeng, X. Wang, X. Peng, J. Li and B. Hong, *Ceram. Int.*, 2023, **49**, 22281–22293.

64 A. Coşkun, A. E. Irmak, B. Altan, Y. S. Ak and A. T. Coşkun, *J. Magn. Magn. Mater.*, 2023, **584**, 171104.

65 J. H. Belo, A. L. Pires, J. P. Araújo and A. M. Pereira, *J. Mater. Res.*, 2019, **34**, 134–157.

66 J. B. Puga, B. D. Bordalo, D. J. Silva, M. M. Dias, J. H. Belo, J. P. Araújo, J. C. R. E. Oliveira, A. M. Pereira and J. Ventura, *Nano Energy*, 2017, **31**, 278–285.

67 T. Yang, B. Kwon, P. B. Weisensee, J. G. Kang, X. Li, P. Braun, N. Miljkovic and W. P. King, *Appl. Phys. Lett.*, 2018, **112**, 063505.

68 M. Hodes, R. Zhang, L. S. Lam, R. Wilcoxon and N. Lower, *IEEE Trans. Compon. Packag. Manuf. Technol.*, 2014, **4**, 46–56.

69 J. Bornacelli, C. Torres-Torres, J. Arenas-Alatorre, M. M. Martínez-Mondragón, L. Rodríguez-Fernández and A. Oliver, *Nanotechnology*, 2020, **31**(35), 355705.

70 D. R. Munazat, B. Kurniawan and D. S. Razaq, *IOP Conf. Ser.: Mater. Sci. Eng.*, 2019, **546**, 042026.

71 A. D. Souza, P. D. Babu, S. Rayaprol, M. S. Murari, L. D. Mendonca and M. Daivajna, *J. Alloys Compd.*, 2019, **797**, 874–882.

72 H. Baaziz, A. Tozri, E. Dhahri and E. K. Hlil, *J. Magn. Magn. Mater.*, 2018, **449**, 207–213.

73 P. A. Yadav, A. V. Deshmukh, K. P. Adhi, B. B. Kale, N. Basavaih and S. I. Patil, *J. Magn. Magn. Mater.*, 2013, **328**, 86–90.

74 A. D. Souza, S. Rayaprol, M. S. Murari and M. D. Daivajna, *J. Supercond. Nov. Magn.*, 2021, **34**, 3319–3331.

75 A. O. Ayaş, E. Seçilmiş and A. Ekicibil, *J. Mol. Struct.*, 2021, **1231**, 130010.

76 S. Koner, S. Satapathy, P. Deshmukh, R. K. Sharma, P. K. Sahoo and S. K. Majumder, *J. Alloys Compd.*, 2023, **986**, 172249.

77 R. Atanasov, E. Brinza, R. Bortnic, R. Hirian, G. Souca, L. Barbu-Tudoran and I. G. Deac, *Magnetic Magnetochem.*, 2023, **9**(7), 170.

78 R. Hamdi, D. Ramotar, S. S. Hayek, A. Samara, S. A. Mansour and Y. Haik, *Inorg. Chem. Commun.*, 2023, **150**, 110551.

79 R. Hamdi, S. S. Hayek, A. Samara, Y. Tong, S. A. Mansour and Y. Haik, *Solid State Sci.*, 2023, **142**, 107223.

80 A. B. Tewari, R. Sharma and D. Sharma, *Results Eng.*, 2023, **20**, 101537.

81 H. Zeng, J. Zhang, C. Kuang and M. Yue, *Appl. Nanosci.*, 2011, **1**, 51–57.

82 P. V. Trevizoli, C. S. Alves, M. A. B. Mendes, A. M. G. Carvalho and S. Gama, *J. Magn. Magn. Mater.*, 2008, **320**, 1582–1585.

83 J. Lyubina, R. Schäfer, N. Martin, L. Schultz and O. Gutfleisch, *Adv. Mater.*, 2010, **22**, 3735–3739.

84 P. Lampen, N. S. Bingham, M. H. Phan, H. Kim, M. Osofsky, A. Piqué, T. L. Phan, S. C. Yu and H. Srikanth, *Appl. Phys. Lett.*, 2013, **102**, 062414.

85 V. Chaudhary, X. Chen and R. V. Ramanujan, *Prog. Mater. Sci.*, 2019, **100**, 64–98.

86 S. Tavares, K. Yang and M. A. Meyers, *Prog. Mater. Sci.*, 2023, **132**, 101017.

87 K. Kutynia and P. Gębara, *Materials*, 2012, **14**, 3129.

88 S. Mandal and T. K. Nath, *Intermetallics*, 2023, **162**, 108019.

89 L. Trombi, F. Cugini, R. Rosa, N. S. Amadè, S. Chicco, M. Solzi and P. Veronesi, Rapid microwave synthesis of magnetocaloric Ni–Mn–Sn Heusler compounds, *Scr. Mater.*, 2020, **176**, 63–66.

90 T. Bachaga, J. Zhang, M. Khitouni and J. J. Sunol, *Int. J. Adv. Manuf. Technol.*, 2019, **103**, 2761–2772.

91 S. Ghosh and S. Ghosh, *Phys. Rev. B*, 2021, **103**, 054101.

92 J. Liu, T. Gottschall, K. P. Skokov, J. D. Moore and O. Gutfleisch, *Nat. Mater.*, 2012, **11**, 620–626.

93 M. Chmielus, X. X. Zhang, C. Witherspoon, D. C. Dunand and P. Müllner, *Nat. Mater.*, 2009, **8**, 863–866.

94 Y. S. Koshkid'ko, E. T. Dilmieva, A. P. Kamantsev, J. Cwik, K. Rogacki, A. V. Mashirov, V. V. Khovaylo, C. S. Mejia,

This journal is © the Owner Societies 2024

Phys. Chem. Chem. Phys., 2024, **26**, 14476–14504 | **14501**

M. A. Zagrebin, V. V. Sokolovskiy, V. D. Buchelnikov, P. Ari-Gur, P. Bhale, V. G. Shavrov and V. V. Koledov, *J. Alloys Compd.*, 2022, **904**, 164051.

95 S. Datta, S. S. Dheke, S. K. Panda, S. N. Rout, T. Das and M. Kar, *J. Alloys Compd.*, 2023, **968**, 172251.

96 V. K. Pecharsky and K. A. Gschneidner, *Adv. Mater.*, 2001, **13**, 683–686.

97 E. Brück, *J. Phys. D: Appl. Phys.*, 2005, **38**, R381–R391.

98 E. Yüzüak, I. Dincer and Y. Elerman, *J. Rare Earths*, 2012, **30**, 217–221.

99 A. Magnus, G. Carvalho, C. S. Alves, A. De Campos, A. A. Coelho, S. Gama, F. C. G. Gandra, P. J. Von Ranke and N. A. Oliveira, *J. Appl. Phys.*, 2005, **97**, 10M320.

100 E. V. Aghababyan and N. P. Harutyunyan, *J. Contemp. Phys.*, 2012, **47**, 142–144.

101 V. Paul-Boncour and L. Bessais, *Magnetochemistry*, 2021, **7**, 1–18.

102 F. X. Hu, B. G. Shen, J. R. Sun, Z. H. Cheng, G. H. Rao and X. X. Zhang, *Appl. Phys. Lett.*, 2001, **78**, 3675–3677.

103 L. Pytlik and A. Zieba, *J. Magn. Magn. Mater.*, 1985, **51**, 199–210.

104 L. Däweritz, *Rep. Prog. Phys.*, 2006, **69**, 2581–2629.

105 S. Gama, A. A. Coelho, A. De Campos, A. Magnus, G. Carvalho, F. C. G. Gandra, P. J. Von Ranke and N. A. De Oliveira, *Phys. Rev. Lett.*, 2004, **93**, 237202.

106 N. Menyuk, J. A. Kafalas, K. Dwight and J. B. Goodenough, *Phys. Rev.*, 1969, **177**(2), 942–951.

107 V. Z. C. Paes, I. L. Graff, J. Varalda, V. H. Etgens and D. H. Mosca, *J. Phys.: Condens. Matter*, 2013, **25**, 046003.

108 A. Jain, S. P. Ong, G. Hautier, W. Chen, W. D. Richards, S. Dacek, S. Cholia, D. Gunter, D. Skinner, G. Ceder and K. A. Persson, *APL Mater.*, 2013, **1**, 011002.

109 F. Cristina Nascimento, A. Oliveira dos Santos, A. de Campos, S. Gama and L. Pavie Cardoso, *Mater. Res.*, 2006, **9**(1), 111–114.

110 H. Wada and Y. Tanabe, *Appl. Phys. Lett.*, 2001, **79**, 3302–3304.

111 U. E. Habiba, K. S. Khattak, S. Ali and Z. H. Khan, *Mater. Res. Express*, 2020, **7**, 046106.

112 N. A. Zarkevich and V. I. Zverev, *Crystals*, 2020, **10**, 1–28.

113 G. Singh, A. Gaur, P. Bisht and R. N. Mahato, *J. Magn. Magn. Mater.*, 2024, **591**, 171731.

114 M. Khlifi, M. Bejar, O. El Sadek, E. Dhahri, M. A. Ahmed and E. K. Hlil, *J. Alloys Compd.*, 2011, **509**, 7410–7415.

115 L. Liu, Z. Zou, B. He, Z. Mao and Z. Xie, *J. Magn. Magn. Mater.*, 2022, **549**, 169006.

116 C. A. Taboada-Moreno, A. M. Bolarín-Miró, F. Pedro-García, C. A. Cortés-Escobedo and F. Sánchez-De Jesús, *J. Magn. Magn. Mater.*, 2023, **570**, 170542.

117 C. A. Taboada-Moreno, F. Sánchez-De Jesús, F. Pedro-García, C. A. Cortés-Escobedo, J. A. Betancourt-Cantera, M. Ramírez-Cardona and A. M. Bolarín-Miró, *J. Magn. Magn. Mater.*, 2020, **496**, 165887.

118 F. Ayadi, Y. Regaieg, W. Cheikhrouhou-Koubaa, M. Koubaa, A. Cheikhrouhou, H. Lecoq, S. Nowak, S. Ammar and L. Sicard, *J. Magn. Magn. Mater.*, 2015, **381**, 215–219.

119 F. Ayadi, S. Ammar, S. Nowak, W. Cheikhrouhou-Koubaa, Y. Regaieg, M. Koubaa, J. Monnier and L. Sicard, *J. Alloys Compd.*, 2018, **759**, 52–59.

120 F. Ayadi, S. Ammar, W. Cheikhrouhou-Koubaa, A. Cheikhrouhou, T. Gaudisson, S. Reguer, S. Nowak, J. Monnier and L. Sicard, *J. Alloys Compd.*, 2017, **691**, 474–481.

121 M. Khlifi, E. Dhahri and E. K. Hlil, *J. Alloys Compd.*, 2014, **587**, 771–777.

122 I. Sfifir, A. Ezaami, W. Cheikhrouhou-Koubaa and A. Cheikhrouhou, *J. Alloys Compd.*, 2017, **696**, 760–767.

123 A. Ezaami, I. Sfifir, W. Cheikhrouhou-Koubaa, M. Koubaa and A. Cheikhrouhou, *J. Alloys Compd.*, 2017, **693**, 658–666.

124 K. Riahi, A. Ezaami, I. Messaoui, M. Solzi, W. Cheikhrouhou-Koubaa, F. Cugini, G. Allodi, F. Rossi and A. Cheikhrouhou, *J. Magn. Magn. Mater.*, 2017, **441**, 776–786.

125 S. Banik, K. Das and I. Das, *J. Magn. Magn. Mater.*, 2019, **490**, 165443.

126 S. Vadnala and S. Asthana, *J. Magn. Magn. Mater.*, 2018, **446**, 68–79.

127 K. P. Shinde, E. J. Lee, M. Manawan, A. Lee, S. Y. Park, Y. Jo, K. Ku, J. M. Kim and J. S. Park, *Sci. Rep.*, 2021, **11**, 20206.

128 K. P. Shinde, C. Hwang, M. Manawan, Y. S. Choi, S. Y. Park, Y. Jo, S. Lee, D. H. Kim and J. S. Park, *RSC Adv.*, 2023, **13**, 9099–9108.

129 Y. Zhang, Y. Tian, Z. Zhang, Y. Jia, B. Zhang, M. Jiang, J. Wang and Z. Ren, *Acta Mater.*, 2022, **226**, 117669.

130 S. B. Madake, A. R. Patil, R. S. Pedanekar, N. A. Narewadikar, J. B. Thorat and K. Y. Rajpure, *J. Mater. Sci.: Mater. Electron.*, 2022, **33**, 6273–6282.

131 C. Zener, *Phys. Rev.*, 1951, **82**, 403–405.

132 R. Dhahri and F. Halouni, *J. Alloys Compd.*, 2004, **381**, 21–25.

133 E. Sellami-Jmal, A. Ezaami, W. Cheikhrouhou-Koubaa, M. Koubaa and A. Cheikhrouhou, *J. Supercond. Nov. Magn.*, 2017, **30**, 489–496.

134 W. C. Koubaa, M. Koubaa and A. Cheikhrouhou, *J. Alloys Compd.*, 2011, **509**, 4363–4366.

135 B. Arun, V. R. Akshay and M. Vasundhara, *RSC Adv.*, 2019, **9**, 23598–23606.

136 I. S. Debbebi, H. Omrani, W. Cheikhrouhou-Koubaa and A. Cheikhrouhou, *J. Phys. Chem. Solids*, 2018, **113**, 67–73.

137 T. M. Al-Shahumi, I. A. Al-Omari, S. H. Al-Harthi, M. T. Z. Myint, P. Kharel, S. Lamichhane and S. H. Liou, *J. Alloys Compd.*, 2023, **958**, 170454.

138 N. T. Dang, D. P. Kozlenko, G. Kim, W. Shon, J. S. Rhyee, D. N. Petrov, T. V. Manh and P. T. Long, *Curr. Appl. Phys.*, 2020, **20**, 794–801.

139 A. M. Bolarín-Miró, C. A. Taboada-Moreno, C. A. Cortés-Escobedo, O. Rosales-González, G. Torres-Villaseñor and F. Sánchez-De Jesús, *Appl. Phys. A: Mater. Sci. Process.*, 2020, **126**, 369.

140 N. Zaidi, M. Elabassi, M. Selmi and E. K. Hlil, *J. Supercond. Nov. Magn.*, 2019, **33**, 2257–2267.

141 M. Elabassi, N. Zaidi and M. O. Khair, *J. Supercond. Nov. Magn.*, 2019, **32**, 3019–3027.

142 A. Biswas, S. Chandra, M. H. Phan and H. Srikanth, *J. Alloys Compd.*, 2012, **545**, 157–161.

14502 | *Phys. Chem. Chem. Phys.*, 2024, **26**, 14476–14504

This journal is © the Owner Societies 2024

143 A. Mabrouki, H. Chadha, O. Messaoudi, A. Benali, T. Mnasri, E. Dhahri, M. A. Valente, S. Elgharbi, A. Dhahri and L. Manai, *Inorg. Chem. Commun.*, 2022, **139**, 109310.

144 Z. Xie, X. Jiang, W. Zhang and Z. Zou, *J. Mater. Sci.: Mater. Electron.*, 2023, **34**, 1514.

145 S. Naas, N. Abassi and C. Boudaya, *J. Mater. Sci.: Mater. Electron.*, 2017, **28**, 17985–17992.

146 B. Arun, V. R. Akshay and M. Vasundhara, *Dalton Trans.*, 2018, **47**, 15512–15522.

147 E. Sellami-Jmal, A. Marzouki, W. Cheikhrouhou-Koubaa, A. Cheikhrouhou and N. Njah, *J. Supercond. Nov. Magn.*, 2015, **28**, 831–838.

148 R. Dhahri, M. Bejar, M. Hajlaoui, N. Sdiri, M. A. Valente and E. Dhahri, *J. Magn. Magn. Mater.*, 2009, **321**, 1735–1738.

149 R. Selmi, W. Cherif and N. M. Ferreira, *J. Supercond. Nov. Magn.*, 2022, **35**, 3585–3601.

150 J. Makni-Chakroun, R. M'nassri, W. Cheikhrouhou-Koubaa, M. Koubaa, N. Chniba-Boudjada and A. Cheikhrouhou, *Chem. Phys. Lett.*, 2018, **707**, 61–70.

151 N. Ameur, F. Elleuch, M. Triki, E. Dhahri, L. Bessais and E. K. Hlil, *Solid State Commun.*, 2019, **289**, 30–37.

152 R. Skini, A. Omri, M. Khlifi, E. Dhahri and E. K. Hlil, *J. Magn. Magn. Mater.*, 2014, **364**, 5–10.

153 C. R. Sankar and P. A. Joy, *Phys. Rev. B: Condens. Matter Mater. Phys.*, 2005, **72**, 024405.

154 P. Schiffer, A. P. Ramirez, W. Bao and S.-W. Cheong, *Phys. Rev. Lett.*, 1995, **75**(16), 3336–3339.

155 S. Majumdar and S. Van Dijken, *J. Phys. D: Appl. Phys.*, 2014, **47**, 034010.

156 H. Fujishiro, T. Fukase and M. Ikebe, *J. Phys. Soc. Jpn.*, 1998, **67**, 2582–2585.

157 A. Szewczyk, M. Gutowska and B. Dabrowski, *Phys. Rev. B: Condens. Matter Mater. Phys.*, 2005, **72**, 224429.

158 H. L. Ju, Y. S. Nam, J. E. Lee and H. S. Shin, *J. Magn. Magn. Mater.*, 2000, **219**, 1–8.

159 Z. M. Wang, G. Ni, H. Sang and Y. W. Du, *J. Magn. Magn. Mater.*, 2001, **234**, 213–217.

160 N. Abdelmoula, J. Dhahri, K. Guidara, E. Dhahri and J. C. Joubert, *Phase Trans.*, 1999, **70**, 197–210.

161 A. N. Ulyanov, S. C. Yu, N. Y. Starostyuk, N. E. Pismenova, Y. M. Moon and K. W. Lee, *J. Appl. Phys.*, 2002, **91**, 8900–8902.

162 W. Abdelhedi, A. Krichene, N. Chniba Boudjada and W. Boujelben, *Ceram. Int.*, 2024, **50**, 11528–11538.

163 Y. Li, H. Zhang, Q. Chen, D. Li, Z. Li and Y. Zhang, *Ceram. Int.*, 2018, **44**, 5378–5384.

164 B. He, Z. Zou, W. Zhang, X. Jiang and Z. Mao, *J. Electron. Mater.*, 2023, **52**, 2665–2675.

165 S. L. Yuan, G. Peng, Z. C. Xia, J. Liu, S. Liu, Z. Y. Li, Y. P. Yang, L. Liu, J. Tang, G. H. Zhang, L. J. Zhang, W. Feng, C. S. Xiong and Y. H. Xiong, *Solid State Commun.*, 2002, **121**, 501–504.

166 S. Blundell, *Magnetism in Condensed Matter*, Oxford University Press, Oxford, New York, 2001.

167 V. E. Salazar-Muñoz, S. A. Palomares-Sánchez, I. Betancourt, T. J. Pérez-Juache, V. D. Compeán-García and A. L. Guerrero, *J. Sol-gel Sci. Technol.*, 2019, **90**, 241–249.

168 A. Marzouki-Ajmi, H. Omrani, W. Cheikhrouhou-Koubaa, M. Koubaa and A. Cheikhrouhou, *J. Alloys Compd.*, 2017, **690**, 403–411.

169 A. G. Gamzatov, A. B. Batdalov, N. Z. Abdulkadirova, A. M. Aliev, V. V. Khovaylo, T. D. Thanh, N. T. Dung and S. C. Yu, *J. Alloys Compd.*, 2023, **964**, 171330.

170 T. D. Thanh, N. T. Dung, N. T. V. Chinh, D. S. Lam, D. A. Tuan and A. G. Gamzatov, *J. Alloys Compd.*, 2021, **884**, 161046.

171 S. Chatterjee and I. Das, *J. Alloys Compd.*, 2023, **935**, 167957.

172 A. F. Manchón-Gordón, A. Gómez, J. J. Ipus, J. S. Blázquez, C. F. Conde and A. Conde, *J. Alloys Compd.*, 2020, **848**, 156566.

173 R. Dhinesh Kumar, R. Thangappan and R. Jayavel, *Res. Chem. Intermed.*, 2018, **44**, 4323–4337.

174 K. Zmorayová, P. Diko and J. G. Noudem, *Mater. Sci. Forum*, 2017, **891**, 468–472.

175 J. Cheng, C. You, N. Tian, Y. Deng, L. Gao, P. Wang, Y. Guo and Z. Li, *J. Magn. Magn. Mater.*, 2024, **596**, 171935.

176 A. Ezaami, N. O. Nasser, W. Cheikhrouhou-Koubaa, M. Koubaa, A. Cheikhrouhou and E. K. Hlil, *J. Mater. Sci.: Mater. Electron.*, 2017, **28**, 3648–3658.

177 H. Baaziz, A. Tozri, E. Dhahri and E. K. Hlil, *J. Magn. Magn. Mater.*, 2016, **403**, 181–187.

178 P. T. Phong, D. H. Manh, L. C. Hoan, T. V. Ngai, N. X. Phuc and I. J. Lee, *J. Alloys Compd.*, 2016, **662**, 557–565.

179 G. Jagadish Kumar, A. Jose, E. P. Jinu, T. T. Saravanan, E. Senthil Kumar, M. Navaneethan, H. Sreemoolanadhan and K. Kamala Bharathi, *Mater. Res. Bull.*, 2023, **160**, 112140.

180 T. L. Phan, N. T. Dang, T. A. Ho, T. V. Manh, T. D. Thanh, C. U. Jung, B. W. Lee, A. T. Le, A. D. Phan and S. C. Yu, *J. Alloys Compd.*, 2016, **657**, 818–834.

181 I. Othmani, Y. Regaieg, F. Ayadi, W. Cheikhrouhou-Koubaa, M. Koubaa, V. Nachbaur, M. Abdelhedi and A. Cheikhrouhou, *J. Supercond. Nov. Magn.*, 2023, **36**, 1143–1152.

182 S. Choura-Maatar, R. M'Nassri, W. Cheikhrouhou-Koubaa, M. Koubaa, A. Cheikhrouhou and E. K. Hlil, *RSC Adv.*, 2017, **7**, 50347–50357.

183 S. Banerjee, *Phys. Lett.*, 1964, **12**, 16–17.

184 C. Henchiri, R. Hamdi, T. Mnasri, M. A. Valente, P. R. Prezas and E. Dhahri, *Appl. Phys. A: Mater. Sci. Process.*, 2019, **125**, 725.

185 J. Dhahri, R. Lefi, S. Bouzidi, M. Essid, F. Abdulaziz, A. H. Alsehli and M. M. Alsowayigh, *Appl. Phys. A: Mater. Sci. Process.*, 2023, **129**, 726.

186 S. Ghorai, R. Skini, D. Hedlund, P. Ström and P. Svedlindh, *Sci. Rep.*, 2020, **491**, 19485.

187 E. Bouzaiene, A. H. Dhahri, J. Dhahri, E. K. Hlil and A. Bajahzar, *J. Magn. Magn. Mater.*, 2019, **491**, 165540.

188 V. Franco, A. Conde, J. M. Romero-Enrique and J. S. Blázquez, *J. Phys.: Condens. Matter*, 2008, **20**, 285207.

189 V. Franco, J. S. Blázquez and A. Conde, *Appl. Phys. Lett.*, 2006, **89**, 222512.

190 Z. Xie, Z. Zou, X. Jiang, W. Zhang, B. He, X. Han and Z. Mao, *Phys. B*, 2022, **639**, 413985.

This journal is © the Owner Societies 2024

Phys. Chem. Chem. Phys., 2024, **26**, 14476–14504 | **14503**

191 C. M. Bonilla, J. Herrero-Albillos, F. Bartolomé, L. M. García, M. Parra-Borderías and V. Franco, *Phys. Rev. B: Condens. Matter Mater. Phys.*, 2010, **81**, 224424.

192 S. A. Makhlouf, T. Nakamura and M. Shinga, *J. Magn. Magn. Mater.*, 1994, **135**, 257–264.

193 K. Momma and F. Izumi, *J. Appl. Crystallogr.*, 2011, **44**, 1272–1276.

194 R. S. Liu, C. H. Shen and S. F. Hu, *Int. J. Inorg. Mater.*, 2001, **3**, 1063–1072.

195 M. Hennel, L. Galdun, A. Džubinská, M. Reiffers and R. Varga, *J. Alloys Compd.*, 2023, **960**, 170621.

196 J. Ouyang, Y. Tian, H. Xiao and Y. Zhang, *Mater. Chem. Phys.*, 2021, **273**, 125150.

197 M. Ye, C. Jing, C. Liu, Y. Zhang, X. Sun, B. Kang, D. Deng, Z. Li and K. Xu, *J. Magn. Magn. Mater.*, 2018, **462**, 178–184.

198 D. M. R. Kumar, M. M. Raja, R. Gopalan, R. Balamuralikrishnan, A. K. Singh and V. Chandrasekaran, *J. Alloys Compd.*, 2008, **461**, 14–20.

199 J. Q. Deng, Y. H. Zhuang, J. Q. Li and K. W. Zhou, *J. Alloys Compd.*, 2007, **428**, 28–33.

200 E. Yüzüak, I. Dincer and Y. Elerman, *J. Rare Earths*, 2010, **28**, 477–480.

201 F. Gao, W. Ren, H. Wu, M. An, X. Zhao, B. Li and Z. Zhang, *J. Solid State Chem.*, 2023, **328**, 124347.

202 R. Nirmala, D. C. Kundaliya, S. R. Shinde, A. G. Joshi, A. V. Morozkin and S. K. Malik, *J. Appl. Phys.*, 2007, **101**, 123901.

203 Z. Wang, Y. Zhang, C. Chen, H. G. Piao, L. Ding, L. Pan, J. Huang, H. R. Park, D. S. Kim and S. C. Yu, *J. Magn. Magn. Mater.*, 2023, **565**, 170147.

204 X. C. Zhong, X. L. Feng, X. W. Huang, X. Y. Shen and Z. W. Liu, *J. Alloys Compd.*, 2016, **685**, 913–916.

205 L. Xian, J. Yu, W. Lin, S. Ke, C. Liu, X. Nie, W. Zhu, P. Wei, D. He, W. Zhao and Q. Zhang, *Intermetallics*, 2023, **153**, 107827.

206 J. I. E. Hu, H. A. O. T. I. A. N. Liu, X. I. N. Y. A. O. Zhang, Z. H. I. Wang, Z. H. I. G. A. N. G. Yang, M. E. N. G. N. A. N. Feng and X. U. E. P. E. N. G. Shi, *Heliyon*, 2024, **10**(3), e25169.

207 Y. Yan, C. Liu, W. Lu, Y. Sun, W. Zhu, X. Nie, X. Sang, W. Zhao and Q. Zhang, *J. Alloys Compd.*, 2022, **910**, 164858.

208 V. Chaudhary and R. V. Ramanujan, *IEEE Magn Lett.*, 2015, **6**, 6700104.

209 V. Chaudhary and R. V. Ramanujan, *Sci. Rep.*, 2016, **6**, 35156.

210 P. Gorria, J. L. Sánchez Llamazares, P. Álvarez, M. J. Pérez, J. Sánchez Marcos and J. A. Blanco, *J. Phys. D: Appl. Phys.*, 2008, **41**, 192003.

211 M. A. Islam and A. K. M. A. Hossain, *RSC Adv.*, 2022, **12**, 17362–17378.

212 S. Hcini, N. Kouki, A. Omri, A. Dhahri and M. L. Bouazizi, *J. Magn. Magn. Mater.*, 2018, **464**, 91–102.

213 J. K. Murthy, K. Devi Chandrasekhar, S. Mahana, D. Topwal and A. Venimadhav, *J. Phys. D: Appl. Phys.*, 2015, **48**, 355001.

214 T. Chakraborty, H. Nhalil, R. Yadav, A. A. Wagh and S. Elizabeth, *J. Magn. Magn. Mater.*, 2017, **428**, 59–63.

215 Y. Jia, Q. Wang, Y. Qi and L. Li, *J. Alloys Compd.*, 2017, **726**, 1132–1137.

216 L. Su, X. Q. Zhang, Q. Y. Dong, Y. J. Ke, K. Y. Hou, C. S. Liu and Z. H. Cheng, *J. Alloys Compd.*, 2018, **746**, 594–600.

217 Y. Jia, Q. Wang, P. Wang and L. Li, *Ceram. Int.*, 2017, **43**, 15856–15861.

218 Z. Dong, Z. Wang and S. Yin, *Ceram. Int.*, 2020, **46**, 26632–26636.

219 D. Chi Linh, N. Thi Viet Chinh, N. Thi Dung, L. Viet Bau, N. Huu Duc, D. Hung Manh and T. Dang Thanh, *Phys. B*, 2023, **661**, 414945.

220 M. E. Botello-Zubiate, M. C. Grijalva-Castillo, D. Soto-Parra, R. J. Sáenz-Hernández, C. R. Santillán-Rodríguez and J. A. Matutes-Aquino, *Materials*, 2019, **12**, 309.

221 H. Baaziz, A. Tozri, E. Dhahri and E. K. Hlil, *Chem. Phys. Lett.*, 2018, **691**, 355–359.

222 S. K. Estemirova, V. Y. Mitrofanov, S. A. Uporov and G. A. Kozhina, *Solid State Sci.*, 2022, **124**, 106806.

223 A. Bouzayen, A. Elghoul, A. Krichene, N. Chniba Boudjada and W. Boujelben, *J. Alloys Compd.*, 2023, **952**, 169986.

224 A. Mabrouki, A. Benali, T. Mnasri, E. Dhahri, M. A. Valente and M. Jemmali, *J. Mater. Sci.: Mater. Electron.*, 2020, **31**, 22749–22767.

14504 | *Phys. Chem. Chem. Phys.*, 2024, **26**, 14476–14504

This journal is © the Owner Societies 2024